Title
Temperature and Tidal Dynamics in a Branching Estuarine System

Author
Wagner, Richard Wayne

Publication Date
2012

Peer reviewed|Thesis/dissertation

Temperature and Tidal Dynamics in a Branching Estuarine System

by

Richard Wayne Wagner, Jr.

A dissertation submitted in partial satisfaction of the

requirements for the degree of

Doctor of Philosophy

in

Engineering – Civil and Environmental Engineering

in the

Graduate Division

of the

University of California, Berkeley

Committee in charge:

Professor Mark T. Stacey, Chair

Professor John C. H. Chiang

Professor Sally E. Thompson

Fall 2012

Abstract

Temperature and Tidal Dynamics in a Branching Estuarine System

by

Richard Wayne Wagner, Jr.

Doctor of Philosophy in Civil and Environmental Engineering

University of California, Berkeley

Professor Mark T. Stacey, Chair

California's Sacramento-San Joaquin Delta (the Delta) will experience tremendous change in the coming decades, as natural variation within the Delta confront wholesale background changes due to climate change, water shortages, potential levee failures, invasive species introduction, and anthropogenic management decisions. In light of this, I present work analyzing a number of facets of the Delta's physical functioning and how they might affect its ecological function.

Using a simple statistical water temperature model, we project water temperatures to warm across the region in the coming century, threatening species near ecological bottlenecks, and stressing other native populations. For example, timing of spring spawning temperatures for Delta smelt will shift earlier in the year. Lethal temperatures for Delta smelt will be more frequent in all four climate scenarios tested. I discuss possibilities for managing the Delta's thermal regime. I did field observations in Cache Slough in the north Delta to parse out smaller scale water temperature variations within a shallow tidal slough. Given bathymetric variation, velocity and thermal gradients develop, which mix and move throughout this complex region. These gradients can intensify near intersections, mixing out over tidal and diurnal cycles. Bathymetric variation combined with atmospheric heating/cooling create thermal gradients. Advection and diffusion move these gradients, which can be intensified where channel merge. Sharp gradients matter biologically; they also create possibilities for refugia for species pushed to their thermal limits. These gradients affect lateral flows, but lateral flows are more strongly affected by lateral wind forcing. Lateral circulation from wind is not strong enough to affect along-channel thermal mixing, as along-channel forcing is strong enough to overcome the homogenization driven by these lateral circulations.

In branching tidal systems, tidal dissipation, propagation and reflection together define the spatial distribution of tidal energy. When specific locations or regions are altered, for example through the restoration of tidal marsh, there is uncertainty as to how the system will respond, including the spatial influence of the changes. When tidal marsh habitat is restored, it creates local tidal dissipation which may alter tidal energy in other parts of the estuary, potentially altering the function of tidal marshes elsewhere. I present results of a simple analytic model of tidal propagation in a branching system. I developed wave equations for along-channel velocity and wave height which account for friction and changes in channel geometry. By linearizing the friction term in the depth-averaged along-channel momentum equation and including an amplification factor in the wave form, then combining it with the continuity equation, I solved for wave speed and amplification as a function of friction and channel geometry. I also solved for the tidal velocity and stage as a function

of position and time. Using this solution within an idealized branching channel estuary and applying matching conditions at the branches, I analyzed the effects of changes to one branch on tidal regimes throughout an idealized branching channel estuary. I then applied this simple model to consider restoration questions on California's Sacramento-San Joaquin Delta.

Acknowledgements

I would like to express my gratitude to all those who helped me along my way. I would like to particularly thank my advisor, Mark Stacy, for your guidance, patience, and help as I stumbled along this path. I appreciate all your help.

Although Mark was a leading figure in my graduate studies at Berkeley, he is by no means alone. Thank you to Tina Chow, Jim Hunt, and Evan Variano for grilling me on preliminary and qualifying exams. Thank you John Chiang and Sally Thompson for helping improve this manuscript. I would like to thank all the professors in whose classes I toiled (at Auburn, at UNO, and at Berkeley), although there are too many to mention. I would also like to give a special shout out to Andy Talmadge at UNO, who helped me understand how to communicate math to people who do not yet understand it (and how to deal with bureaucracy patiently). Although this work was less directly applicable, I think I may use it as frequently as any fluid mechanics concept I have learned since.

I would be completely remiss if I did not thank my high school teachers who laid the foundation for my future academic successes. I never would have believed that you taught me anything when I was there, but it's clear that you did and that you did a good job. Thank you.

Thank you to my fellow grad students. Thanks to 'Super' Scott Mansell (and his wife Jenn and their three beautiful daughters) for hosting me for dinner from time to time and treating me as one of the family. I am proud of y'all and jealous all the same. To Sam, Jackie, and Charlie, thank you for being wonderful children. Thanks to Justin Jasper for the great runs and better wisdom. Nicely done. Thanks to Audric Collignon and Julia Davis for all the outdoor adventures. It's so awesome to meet people as excited by the world as I am, even if I am sometimes overwhelmed by your enthusiasm and ability. I would like to thank those who helped me in the field (Maureen Kunz, Carlos Oroza, Rebecca Leonardson, Audric Collignon, Scott Mansell, Steve Gladding, Mark Stacey, Megan Williams, Rudi Schuech, Andrew Tinka, Bowen Zhou, and Ian Tse, in no particular order). Thank you. I hope y'all had as much fun as I did. The data came out fine. Thanks to Rusty Holleman, who never made it into the field with me, but who convinced me that imaginary numbers *do* exist. Thanks for all the conversations. Thank you Lissa MacVean, for showing me what field work is and how muddy it can get. I need to mention Rudi, Ian, Mary Cousins, and Dave Wiersema for being my cubicle-mates. I know I can be loud; I just get so excited about stuff sometimes. I need to particularly mention Rudi and Mary; thanks for putting up with me when I was a first-year grad student. I know I asked a million annoying questions. Thanks for putting up with everything. To the rest of the Environmental Fluid Mechanics group, I say thanks. You are so awesome and bright and cheery and wonderful and excellent at ping pong. (Well, Rudi is definitely *not* cheery, but the rest of you are.) Thank you.

To my family and friends, thank you. To my parents, Wayne Wagner, Sr. and Tibby Wagner, my siblings, Hugh Wagner, Dorothy Strachan, and Mimi Agee, and their children, Riley and Aiden Agee and Hannah Strachan, and uncles and aunts, Hugh Penn, John and Lydia Cartafalsa, Patricia Thompson, Sandy Gooddail, Emile Wagner, and Tommy Wagner, thank you for putting up with so much separation. It has been hard for me to be so far away for so long and to miss so much in your lives. I hope I can be there much more in the future. Thanks for your support. To my friends, thank you for understanding when I was tired or overworked or late. Grad school is not always easy; thank you for understanding. I would like to particularly thank roommates (past and present)

Max Baumhefner, Rosie Ueng, Tico Ramirez, Isabel Permdoro, Mindy Lee, Dan Mode, Laura Shulthies, Cora Stryker, and Sid Breckinridge. You all have been great to live with. I love you all and hope to continue to know you. To the friends I have met along the way (Pam Kaercher, Brad Allen, Caroline Adams, Jason Burwen, among so many others), you have made this journey wonderful to take. Thank you so much.

To all who I have forgotten to mention, I have not forgotten you. Thank you so very much. I appreciate you all more than this simple document could ever express. Thanks.

Table of contents

Chapter 1 Introduction **1**
1.1 Background 1
1.1.1 Importance of Estuaries 1
1.1.2 Importance of Water Temperature 1
1.1.3 Importance of the Interconnectivity of Branching Channels 3
1.2 Field Site 3
1.2.1 Overview of California's Sacramento-San Joaquin Delta 3
1.2.2 Cache Slough/Liberty Island 5
1.3 Research Questions 6
Chapter 2 Statistical Model of Water Temperature in the Delta **8**
2.1 Introduction 8
2.1.1 Study Location 8
2.2 Data 9
2.2.1 Measured Water Temperature Data 9
2.2.2 Measured Forcing Data 10
2.2.3 Forcing for Water Temperature Projections 10
2.3 Data Analysis 11
2.3.1 Temporal Variability 11
2.3.2 Spatial Variability 12
2.4. Methods 13
2.4.1 Development of Statistical Temperature Model 13
2.4.2 Performance Metrics 16
2.5 Results 16
2.5.1 Calibration and Verification of Statistical Temperature Model 16
2.5.2 Projections of Water Temperatures for Climate Scenarios 18
2.6 Discussion 20
2.6.1 Model Limitations 20
2.6.2 Flow Effects 20
2.6.3 Temperature Trends 23
2.6.4 Ecological Implications 24
2.7 Summary 25
Chapter 3 Mixing and Thermal Dynamics in a Shallow Tidal Slough System **26**
3.0 Introduction 26
3.0.1: Research Questions 26
3.0.2: Background 26
3.0.2.1 Water Temperature 26
3.0.2.2 Estuarine Mixing - Lateral and Along-Channel 26
3.0.2.3 Interactions: Temperature, Lateral Dynamics, and Along-Channel Dynamics 27
3.0.2.4 Wind Effects on Estuaries 28
3.1 Site Overview 28
3.2 Methods 31
3.2.1 Field campaign 31
3.2.2 Data Analysis 31
3.2.2.1 Principal Component Analysis 31
3.2.2.2 Multiple Linear Regression 32

3.3 Results 32
3.3.1 Field Observations 32
3.3.3.1 Atmospheric Observations 32
3.3.1.2 General Water Column Observations 33
3.3.1.3 Water Temperature Observations 34
3.3.1.4 Velocity Observations 35
3.3.2 Principal Component Analysis 37
3.3.3 Multiple Linear Regression 39
3.4 Discussion 43
3.4.1 Temperature 43
3.4.2 Lateral Momentum 44
3.4.3 Along-Channel Dynamics 44
3.4.4 Connections: Temperature, Lateral Momentum, and Along-Channel Mixing 45
3.4.4.1 Along-Channel Dynamics create Lateral Thermal Gradients 45
3.4.4.2 Lateral Shear does not affect Along-Channel Dynamics 46
3.5 Summary 47
Chapter 4 Exploration of Tidal Propagation in a Branching Channel Estuary 49
4.1 Introduction 49
4.1.1 Importance of Tidal Regime to Ecosystem Function 49
4.1.2 Modeling Tidal Systems 50
4.1.3 Study Domain 51
4.2 Methods 52
4.2.1 Development of wave equations 53
4.2.2 Development of branching channel equations 56
4.2.3 Development of framework for exploration 57
4.3 Broad Theoretical Study: Results and Discussion 58
4.3.1 Broad theoretical results 58
4.3.1.1 Even Split Case Setup and Results 59
4.3.1.2 Even Split Case Discussion 61
4.3.1.3 Uneven Split Case 62
4.3.1.4 Uneven Split Case Discussion 63
4.3.2 Case Study: The Sacramento-San Joaquin Delta 63
4.3.2.1 Restoration on the San Joaquin Results 64
4.3.2.2 Restoration on the San Joaquin Discussion 65
4.3.2.3 Restoration on the Sacramento 65
4.3.2.4 Restoration on the Sacramento Discussion 66
4.4 General Discussion 67
4.5 Summary 68
Chapter 5 Conclusions 69
5.1 Summary and Implications 69
5.2 Future Work 70
References 71
Appendix A: Flow Effects on Water Temperatures 77

Chapter 1

Introduction

1.1 Background

1.1.1 Importance of Estuaries

Estuaries are coastal water bodies and their associated wetlands where oceanic saltwater mixes with riverine freshwater. The size and shape of estuaries varies tremendously around the globe as they are affected by the local geography, hydrology, tidal variation, sediment, climate, etc. (Elliott and McLusky 2002). The interplay of fresh and salty waters often creates a biologically rich ecosystem, as well as providing physical connections between the ocean and farms and factories upstream. Because of the productivity and value of estuaries, human use of these resources has been prodigious. People have diked, drained, and farmed estuarine wetlands, while containing the estuaries to tidal sloughs and rivers, limiting floodplain access and cutting off wetland vegetation. Often, these changes set into motion a cascade of land and water management problems. For example, subsidence of farmland leads to calls for increased levee heights, which further cutoff sloughs from their floodplains. Farmers demand freshwater, which requires altering and managing river flow, further straining weakened ecosystems. Estuaries are often the center of intensive human development (urban, suburban, and rural) and are used for recreation. Often, anthropogenic activity has long-lasting effects on ecosystem function. These competing interests manifest themselves in the Sacramento-San Joaquin Delta (Lund et al. 2007).

The regional importance of estuaries, and the political and legal frameworks that govern their environmental condition have motivated an extensive research effort into estuary function. In the Sacramento-San Joaquin Delta, estuarine management and state-wide policy decisions have become entangled with the delta smelt (*Hypomesus transpacificus*), a small, low-fecundity, threatened fish (Bennett 2005). The risk of entrainment of delta smelt into south Delta pumps, which bring water to agricultural and municipal consumers south of the region, has led to legal rulings requiring the operations of the pumps to be limited during certain critical periods.

This dissertation outlines a research program aimed at advancing our understanding of the thermal and tidal dynamics within the branching estuarine system of California's Sacramento-San Joaquin Delta (the Delta). The results may be applicable to many water systems throughout the world. Chapter 1 introduces this research program, discussing the motivation, field site, and research questions to be addressed. Chapter 2 outlines a Delta water temperature model used to project effects of climate change on the Delta's thermal ecosystem. We specifically look at effect on the delta smelt. Chapter 3 focuses on water temperature dynamics on length-scales which vary from along a shallow tidal slough to vertical within those sloughs. Chapter 4 discusses tidal dynamics within a branching system. Much of the background/literature review for chapters 2 through 4 will be contained within them. All of this work has implications for the management of California's Delta; the big picture implications will be discussed in chapter 5.

1.1.2 Importance of Water Temperature

In freshwater and near-coastal marine ecosystems, water temperatures provide an important constraint on ecological function (Coutant 1976). Examples include effects on fish spawning (Hotta et al. 2001), swimming performance (Myrick and Cech 2000), metabolism (Das et al. 2005; Scheller

et al. 1999), and mortality (Coutant 1976; Johnson and Evans 1996) as well as effects on aquatic invertebrates (Vannote and Sweeney 1980; Ward and Stanford 1982). Species of concern within the Sacramento-San Joaquin Delta that are sensitive to water temperatures at various points in the life cycles include the Sacramento winter run Chinook salmon (*Oncorhynchus tshawytscha*) (Baker et al. 1995), the Sacramento splittail (Moyle et al. 2004), and the delta smelt (Bennett 2005; Swanson et al. 2000).

Within an estuary, thermal regimes can control the suitability of a region as habitat for certain species during various points in their life cycles. Since the thermal regime is expected to vary seasonally and tidally within an estuary, pelagic organisms are forced to move in response to this ever-changing environment. Large, strong swimmers may be able to track plumes of favorable water (Geist et al. 2005), but weaker swimmers may be more vulnerable (Oliveira et al. 2006). The physical complexity of an estuary means that large thermal gradients may exist at junctions between channels, vertically (during large heating events), laterally (where two channel meet), or longitudinally (as the water warms or cools due to mixing or atmospheric influence).

Temperature within the water column is constantly affected by atmospheric fluxes from above, as well as advection and dispersion of thermal gradients from other areas of the estuary (Monismith et al. 2009). On small scales, water temperature can behave much like a passive scalar (nutrients, phytoplankton, etc.). These scalars travel primarily in suspension and their transport is predominantly controlled by local flows. Gradients of these scalars are formed and broken down by physical, chemical, and biological processes; locations of large gradients are also often locations of large estuarine productivity (Largier 1993). Mixing processes within the estuary serve to lessen these gradients (Fischer et al. 1979). These scalars can be sourced locally or can flux into or out of the region through advection or dispersion. The flows are forced by winds, tides, stream flow from up-estuary, and pumping.

Mixing processes within complex systems are often described as "scale-dependent," i.e. the rate at which a scalar spreads is a function of the size of the plume itself. Often, this is due to the plume's growing large enough to experience different flow regimes in different areas of a water mass. For example, in an estuary, branching channels can present different flow regimes which, in turn, affect mixing processes (MacVean and Stacey 2010). Frictional differences between the tributary channels can lead to tidal phase shifts from one to the other. These shifts lead to scalar spreading along the axis of the main channel. The flow regimes in each channel can be affected by changes in the boundaries of the others, changing mixing characteristics for a region. From an ecosystem perspective, these changes can affect the timing or location of temporary estuarine fronts. Waters merging in an estuarine junction may remain separated and form a front; shear instabilities along these lines of separation act to mix across them. Where flooded islands connect to the surrounding estuary, asymmetric draining and filling (called “tidal pumping”) generates a net flux of scalars into or out of the island (Fischer et al. 1979). These local mixing processes serve to set the time-scales of mixing for the region as a whole; as a scalar plume grows in size, the number of channel junctions it will experience will increase.

Mixing behavior is further complicated in the case of water temperature because it is not, however, a passive scalar. By altering the bouyancy of water, temperature affects the dynamics of advection and dispersion in an estuary directly. If thermal gradients are large enough, water temperature can affect water densities and drive or prevent fluid flow. Horizontal thermal gradients can drive baroclinic forcing, as warmer, less dense waters seek to spread across the top of cooler,

denser water. Further, heating and cooling from above can create stable or unstable stratification, respectively. This stratification is important because it inhibits turbulent length-scales and often increases estuarine exchange flow.

1.1.3 Importance of the Interconnectivity of Branching Channels

In an effort to a) control costs associated with maintaining anthropogenic controls on estuaries (levees, pumps, dams, etc.), b) provide flood protection (by providing water storage in some cases or storm surge buffers in others (e.g. Louisiana, Holland), and c) restore ecosystem function both for recreation and for environmental sustainability, wetland restoration is often advocated (Pethick 2002).

One way to restore wetlands is to remove the physical barriers to tidal action (Athearn et al. 2010; van Proosdij et al. 2010). Often, breaching a levee will restore tidal action to a previously dry island. The consequences of that "restoration," however, are not necessarily well understood. There are several uncertainties that underlie levee removal. Flooding an island can have a large effect on the thermal regime of the region. This can occur through several mechanisms: 1) Increasing the tidal prism, the volume that can be filled by tides, brings more water into the region on each tide. This water has its own thermal characteristics, and it will take time for it to equilibrate to the local conditions. 2) Increased flows from the larger tidal prism will lead to increased vertical mixing, affecting temperature profiles. These increased flows will also affect all regions down-estuary. 3) The large increase in the water surface area in the region following flooding of the island permits greater atmospheric interchange with the water column.

While the island may become a functioning wetland, the timescales for such a return, however, are not well-known. Flooded subsided islands can act as sinks of sediment in an estuary, potentially causing other functioning areas to erode (Brew and Williams 2010). As a flooded island slowly fills with sediment, it provides habitat that was not typical of the native system, offering refuge for non-native biota. Additionally, changes to tidal energy reflection within a system can affect the tidal amplitudes throughout the estuary. If the amplitude is too greatly altered, functional tidal marsh can be drowned or greatly diminished as it responds to changing water heights. Further, if tidal velocities are altered, mixing and transport are affected (Fischer et al. 1979).

1.2 Field Site

1.2.1 Overview of California's Sacramento-San Joaquin Delta

California's Sacramento-San Joaquin Delta (the Delta), the subject of this dissertation, is a large (~200km x ~300km) estuary on the west coast of the United States. The Delta is located at the upstream end of the San Francisco Estuary. Detailed descriptions of the Delta can be found in (Kimmerer 2004) and (Lund et al. 2007). It consists of a network of channels and flooded "islands" (Figure 1-1) that are fed by freshwater flow from a number of rivers that drain California's Central Valley, most significantly the Sacramento and San Joaquin Rivers (Kimmerer 2004). The Delta serves as the hub of California's water system, draining roughly 45% of the state's area (Lund et al. 2007) and providing water supply to approximately two-thirds of its population. The Delta is important as a source of freshwater (locally and state-wide), drainage, habitat, and recreation. In its unaltered state, the Delta was a system of sloughs and marshlands (both of which were open to influence from river flows and tidal effects), but currently it is a system of leveed, subsided farmlands separated by channelized tidal sloughs and rivers (Kimmerer 2004). Because of the delta

smelt and other environmental concerns, the Delta is heavily studied (Kimmerer 2004), with researchers working to understand the physics, biology, and chemistry and interactions between the three that affects the Delta ecosystem and function.

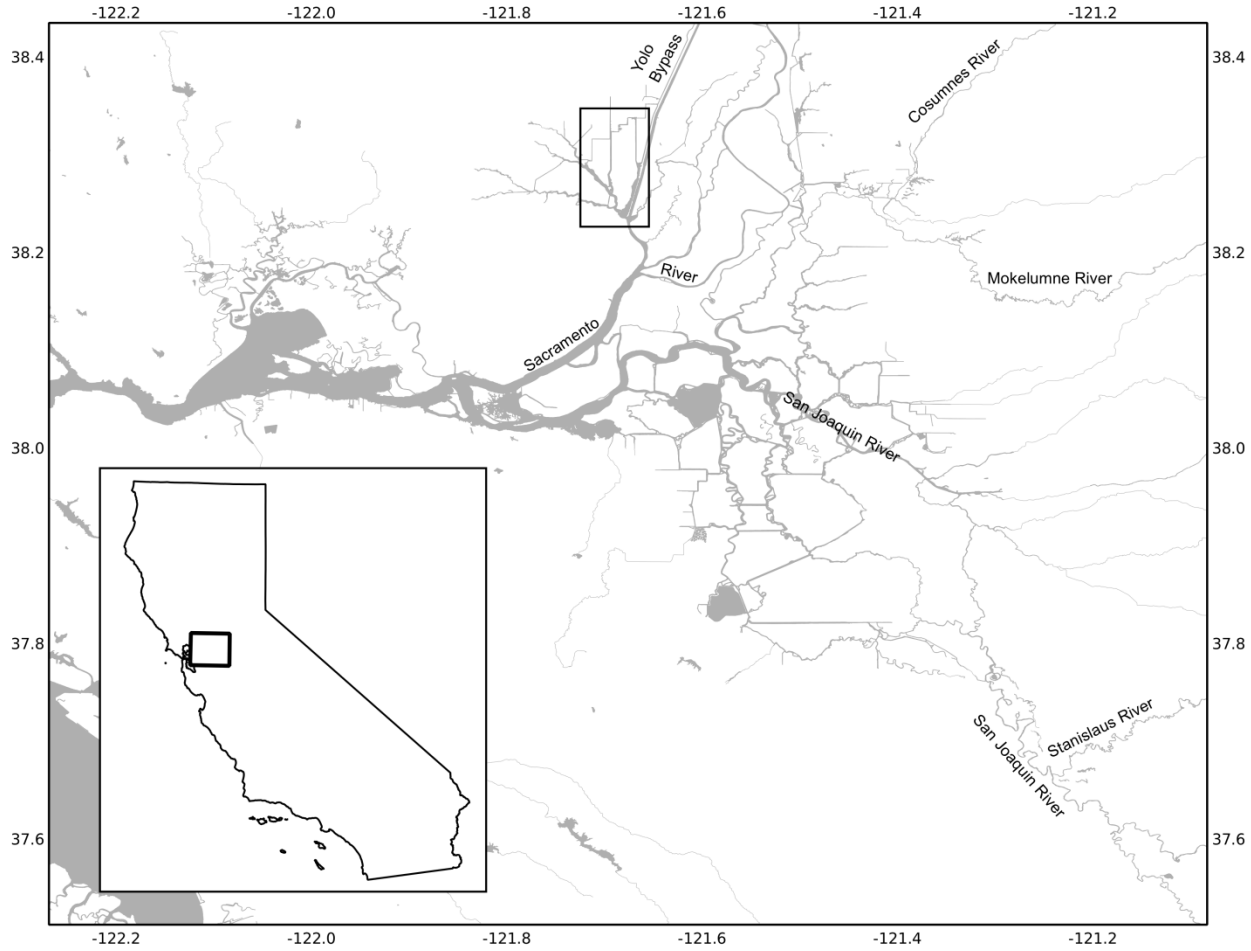

Figure 1-1. California's Sacramento-San Joaquin Delta. The Cache Slough/Liberty Island region (Figure 2) is boxed.

California's water distribution system relies heavily on the Delta, because reservoir releases must move through the Delta on their way to pumping stations for delivery to water users throughout the state (Lund et al. 2007). The most important of these stations are located in the southern Delta and provide water for the Delta Mendota Canal and the California Aqueduct, both of which carry water to municipal and agricultural users south of the Delta (Kimmerer 2004). Levees, dams, and diversions have drastically altered the hydrologic system from its native state. The ecology of the delta has been similarly altered, not only due to the changing hydrology but also because of introductions of non-native fish, clams, and aquatic plants (Kimmerer 2004). Climate change is predicted to impact the Delta in a number of ways; hydrologically due to changing timing and proportions of snow and rainfall in the Sierra Nevada mountains (Vanrheenen et al. 2004), thermally as the local heat budget adjusts to a warmer atmosphere, and tidally as the estuary responds to sea level rise.

The Delta is forced by fresh water flow from numerous rivers to the east, north, and south, tides from San Francisco Bay, and atmospheric conditions. The complex geography of the region

enhances local mixing due to the dispersive effects of oscillatory flow in a network of channels and junctions. Mixing within the Delta is therefore likely to be scale-dependent. The bathymetry of the Delta helps to create thermal gradients, as shallow shoals and islands respond to atmospheric heating/cooling quicker than deeper channels.

1.2.2 Cache Slough/Liberty Island

A sub-region of the Delta, the Cache Slough/Liberty Island (CSLI) complex (boxed in Figure 1-2), contains a flooded island, Liberty, and numerous connecting sloughs (Figure 1-2). Liberty Island is the site of much study, as it represents an accidental restoration project within the north Delta. Located at the downstream end of the Yolo Bypass, a flood control spillway for the Sacramento River, and within the Cache Slough complex, Liberty Island was set aside for seasonal farming in the 1920s, provided it was allowed to flood seasonally. In the 1990s, its levees breached and were abandoned in 1997. The island itself has not subsided as badly as other islands in the Delta. Much of the northern portion of the island is currently high enough to sustain functional tidal marsh after flooding; the rest of the island gets gradually deeper as it approaches its exit at Cache Slough. The southern (open-water) end of Liberty is now considered a refuge for longfin smelt (*Spirinchus thaleichthys),* delta smelt (*Hypomesus transpacificus*), Sacramento splittail (*Pogonichthys macrolepidotus*) and striped bass (*Morone saxatilis*). Three of these (excluding the Sacramento splittail) are being carefully studied due to the collapse in their abundances; this collapse is referred to as the Pelagic Organism Decline (POD). This is why, in spite of its accidental formation, Liberty Island is viewed as a possible paradigm for restoration efforts in the Delta.

Figure 1-2. The Cache Slough/Liberty Island complex. Fresh water enters the system primarily at its southern end from the Deep Water Shipping Channel. All the connecting sloughs and channels are tidally influenced.

1.3 Research Questions

The research in this dissertation is aimed at beginning to answer the fundamental question: What are the thermal mixing dynamics and the physical processes that control them within an estuary at a variety of length- and time-scales? This work will focus on physical processes and their implications for ecosystem health and restoration. This work is sub-divided into three parts:

1) How do water temperatures vary on large length- and time-scales across the Delta? What does this imply for critical species in the Delta, specifically the delta smelt. (Chapter 2)

Heat can enter or leave the water column through atmospheric fluxes and advective/dispersive fluxes. The heat fluxes can be primarily broken down into five terms: short-wave radiation, upward long-wave radiation from the estuary's surface, downward short-wave radiation from atmospheric water vapor, sensible heat, and evaporative heat flux (Miyakoda and Rosati 1984; Uncles and Stephens 2001). Heat will also enter the area through advective/dispersive fluxes, as water from outside a region is tidally- or wind-driven into or out of the area.

With climate change predicted to create slowly changing air temperatures (and potentially other atmospheric forcings), what changes will occur to Delta water temperatures? Without an understanding of the physical processes that determine water temperatures, we cannot know how much change to expect in the coming decades or century. What effect will changes to the Delta's thermal regime have on the Delta ecosystem, specifically on the delta smelt? The delta smelt dies at 25°C (Bennett 2005; Swanson et al. 2000). Can we expect this thermal limit to be reached more often in the Delta? How much do reservoir releases from dams upstream affect water temperatures within the Delta (if at all)? Without this knowledge, we cannot hope to know if reservoir releases will help in times when the Delta ecosystem might be near critical thermal limits. This work presents results from a modeling study based on data collected by public agencies reflecting water and atmospheric conditions and on the impact of the changes the model predicts on delta smelt.

2) What controls temperature and thermal gradients within a tidal slough? Can this be managed to improve thermal refugia for species? (Chapter 3)

At these scales, tidal trapping and shear dispersion are processes typically expected to dominate along-channel mixing, with turbulence playing a smaller role. Within the cross-section, however, these processes are less important as local processes dominate. Advection and mixing compete with atmospheric influence (from heating/cooling and from wind) to control thermal dynamics. Lateral gradients result when warmer waters advect downstream along one bank; the relaxation of these waters across the channel converts these lateral gradients into vertical stratification. Mixing, either driven by turbulence or other processes, serves to smooth these gradients.

Vertical gradients can be formed by heating from above, as warm surface waters create a stably-stratified water column. Atmospheric cooling can create unstable stratification. Wind forcing creates stress near the surface of the water, both in the water and in the air. The stress in the air increases thermal atmospheric fluxes. The stress in the water creates turbulence, enhancing mixing near the surface and driving surface water deeper into the water; this can ultimately de-stratify the water column. The wind effects will be highly variable over the study area, as the wind strength and direction varies on fairly small length- and time-scales; bathymetric variation and changes in the wind's duration will cause the importance of the wind to local mixing to vary. Variation in wind

direction will also change the local fetch, causing the wind's effects to vary. The wind can also create free-surface gradients which can affect sub-surface flows.

Without understanding the length-scales, time-scales, or intensity of these vertical gradients, managers will not know if thermal refugia are likeley to exist within the Delta if climate change scenarios are realized. Further, if the causes of the formation of these refugia are unknown, managers cannot create a Delta likely to have them. The focus of this work is determining which processes drive thermal gradient creation and breakdown along longitudinal, lateral, and vertical directions within a tidal slough. We present results and analysis of data from two field campaigns, combined with data from public agencies to characterize atmospheric conditions, over a two-week and a month-long period in late 2009 and early 2010.

3) How do tides interact across junctions? Will restoration efforts affect ecologically functional systems elsewhere in the estuary? (Chapter 4)

Tidal trapping, as mentioned above, depends on different flow regimes in different regions of an estuary. The branches of an estuary provide different flow regimes, but they also interact. Tidal energy, driven from the mouth of the estuary, splits at channel junctions: Some energy reflects, and some goes down each branch. Whenever the tidal wave encounters a boundary, whether it is a levee, a marsh, a junction, or something else, there is a reflection of some portion of the tidal energy back towards the mouth. The amount of wave energy reflected is a function of the boundary (Moller et al. 1999). This reflected energy, upon reaching the branch it came up, shows no preference for traveling back towards the mouth or sampling the other branch. As such, the energy splits again, as a function of the geometry of the channels involved. As tidal energy moves in a system like this, these waves interfere, constructively and destructively, in such a way as to create a single waveform that is typically labeled "the tide."

Restoration efforts, as mentioned above, often involve regional-scale changes to the boundaries of the estuary. This is often through flooding otherwise leveed farmland. Although the changes to the system are intended to improve habitat quality, decision makers need to know how much the restoration effort will affect tidal reflection and, through it, the entire region or Delta. Due to the many reflections that go into the creation of the tide in a branching channel estuary, this research seeks to understand the effect of changing the boundaries of a branch (and thereby affecting the amount of reflected energy) on the tide in the other branch. If the tides in a region are too greatly altered, ecological function could be affected. This chapter presents results of a theoretical framework for an idealized branching channel estuary and used this framework to answer basic questions about tidal interconnectivity in the Sacramento-San Joaquin Delta.

What are the thermal mixing dynamics and the physical processes that control them within an estuary at a variety of length- and time-scales? In the next three chapters, I present three studies on mixing and interconnectivity in California's Sacramento-San Joaquin Delta.

Chapter 2

Statistical Model of Water Temperature in the Delta

2.1 Introduction

In freshwater and near-coastal marine ecosystems, water temperatures provide an important constraint on ecological function (Coutant 1976). Examples include effects on fish spawning (Hotta et al. 2001), swimming performance (Myrick and Cech 2000), metabolism (Das et al. 2005; Scheller et al. 1999), and mortality (Coutant 1976; Johnson and Evans 1996), as well as effects on aquatic invertebrates (Vannote and Sweeney 1980; Ward and Stanford 1982). Specific examples of species of concern within the Sacramento-San Joaquin Delta that are sensitive to water temperatures at various points in the life cycles include the Sacramento winter run Chinook salmon *Oncorhynchus tshawytscha* (Baker et al. 1995), the Sacramento splittail *Pogonichthys macrolepidotus* (Moyle et al. 2004), and the delta smelt *Hypomesus transpacificus* (Bennett 2005; Swanson et al. 2000).

Climate change is projected to result in increases in mean annual air temperature of 2.2-5.8^{o}C in the coming century averaged across the state of California (Loarie et al. 2008). An increase in air temperature will lead to earlier snowmelt, more precipitation falling as rain (vs. snow), and changes in the operation of California's water delivery system (Barnett et al. 2008; Vanrheenen et al. 2004). To analyze the effects of climate change on fish populations, however, we require projections of water temperature under global warming scenarios.

In tidal systems, the water temperature at a particular location is determined by the interplay between atmospheric forcing, tidal dispersion, and riverine flows (Monismith et al. 2009). Formal models of tidal dispersion are not currently feasible for projections of temperature over centuries given the magnitude of the computational requirements. In view of this limitation, we have developed a statistical model of temperature in the Sacramento-San Joaquin Delta. Our emphasis in this paper is on understanding the dynamics of water temperatures and their possible effects on aquatic species.

2.1.1 Study Location

This study focuses on California's Sacramento-San Joaquin Delta (the Delta) and nearby environs, which are located at the upstream end of the San Francisco Estuary. Detailed descriptions of the Delta can be found in Kimmerer (2004) and Lund et al. (2007). It consists of a network of channels (Figure 2-1) that are fed by freshwater flow from a number of rivers that drain California's Central Valley, most significantly the Sacramento and San Joaquin Rivers (Kimmerer 2004). The Delta serves as the hub of California's water system, draining roughly 45% of the state's area (Lund et al. 2007) and providing water supply to approximately two-thirds of its population. In its unaltered state, the Delta was a system of sloughs and marshlands (both of which were open to influence from river flows and tidal effects), but currently it is a system of leveed, subsided farmlands separated by channelized tidal sloughs and rivers (Kimmerer 2004).

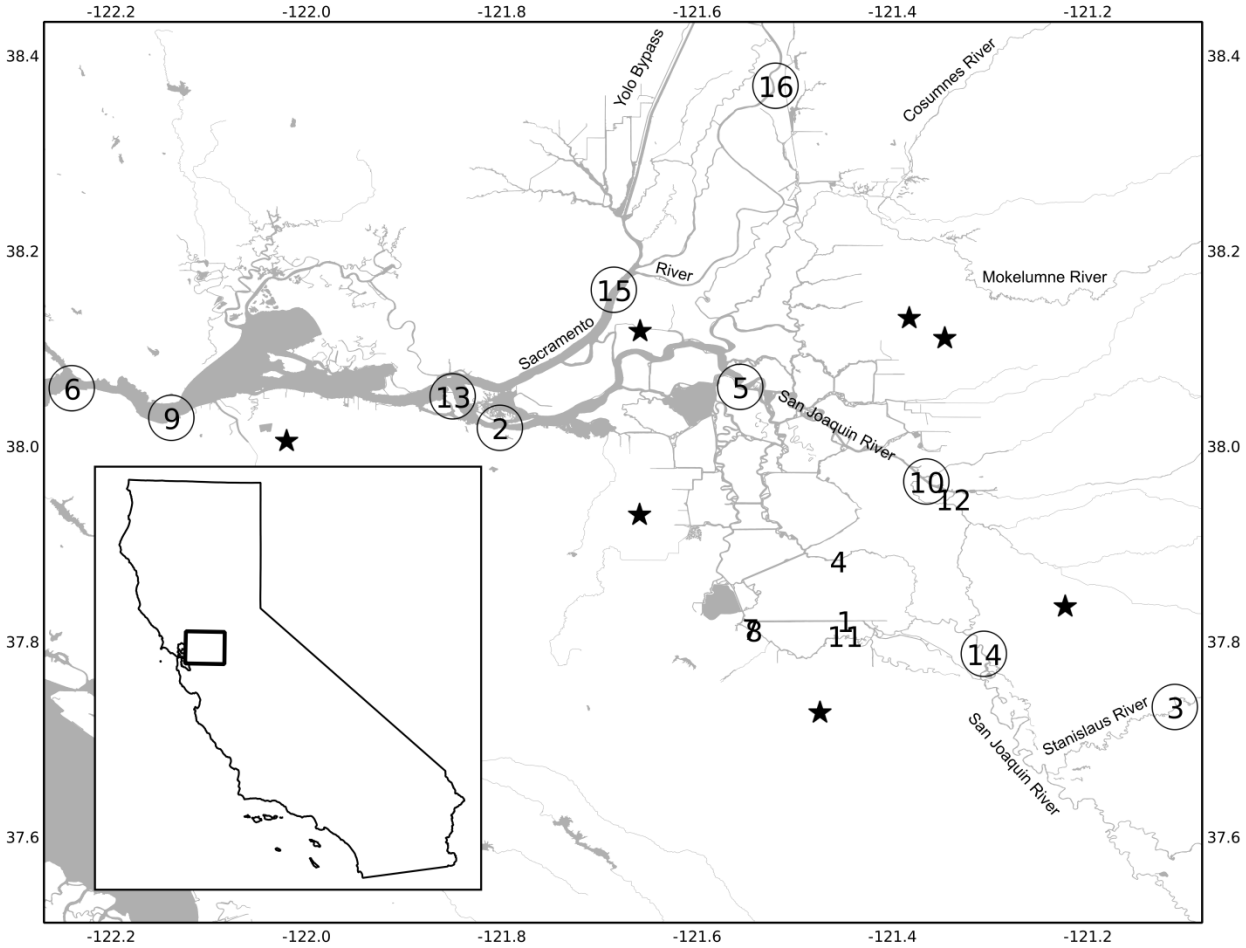

Figure 2-1. California's Sacramento-San Joaquin Delta and environs. The Delta is forced primarily by Sacramento River flow from the north, San Joaquin River in the south, and tides from San Francisco Bay in the west. The locations of the water temperature stations are numbered; stations with circles had greater than one year's worth of data. CIMIS weather stations are denoted with stars.

California's water distribution system relies heavily on the Delta, because reservoir releases must move through the Delta on their way to pumping stations for delivery to water users throughout the state (Lund et al. 2007). The most important of these stations are located in the southern Delta and provide water for the Delta Mendota Canal and the California Aqueduct, both of which carry water to municipal and agricultural users south of the Delta (Kimmerer 2004). The levees, dams, and diversions have drastically altered the hydrologic system from its native state. The ecology of the delta has been similarly altered, as it has responded to the changing hydrology as well as introductions of non-native fish, clams, and aquatic plants (Kimmerer 2004). Climate change will impact the Delta in a number of ways; examples include hydrologic change as the proportion of precipitation falling as snow declines in the Sierra Nevada mountain range (Vanrheenen et al. 2004), local heat budget adjustment to a warmer atmosphere, and estuarine response to sea level rise.

2.2 Data

2.2.1 Measured Water Temperature Data

We downloaded time series of measured water temperatures from the Interagency Ecological Program (http://www.iep.ca.gov), which receives the data from the California Department of Water Resources (DWR), the United States Geologic Survey (USGS), the California

Data Exchange Center (CDEC), and the United States Bureau of Reclamation (USBR), for locations throughout the Delta (Figure 2-1). For many stations, water temperature data collection started in the mid-1980s and extends to the current time. The data have been collected at either 15-minute intervals or hourly. For consistency among the data sets, we averaged the 15-minute data to give hourly datasets. To handle outliers, we deleted all points outside 4 standard deviations from the mean of 20-hour windows of the data. At locations where two or more agencies collected data, we averaged the data to create one dataset for each location. We calculated the daily maximum, average, and minimum water temperatures from these data for model calibration and verification.

2.2.2 Measured Forcing Data

We downloaded hourly air temperatures and insolation from the California Irrigation Management Information System (CIMIS, http://www.cimis.water.ca.gov) at seven locations within the Delta (Figure 1; stations were Lodi, Brentwood, Manteca, Twitchell Island, Lodi West, Tracy, and Concord). We downloaded an additional six air temperature locations from the Interagency Ecological Program (locations 2, 9, 10, 13, 14, and 15 on Figure 1). As an initial processing step, we removed improbable values (air temperatures less than -5°C or greater than 45°C; insolation less than 0 W/m^2 or greater than the solar constant (1368 W/m^2, (Rubin and Davidson 2001)) from both datasets.

To handle outliers in the air temperature data, we deleted all points outside 4 standard deviations from the mean of 20-hour windows of the data. Model verification requires continuous forcing because the model output depends on the output from the previous time-step. For this reason, and for verification use only, we created a second air temperature dataset wherein gaps in the data shorter than 72 hours were filled. We filled small gaps (< 6 hours) in this second dataset through linear interpolation. We filled longer gaps (< 72 hours) by first linearly interpolating and then adding a diurnal pattern defined by the diurnal cycles during adjacent (within one week) time periods spanning the same time of day as the gap. The daily cycle was defined by an average based on the time of day, and was then added to the linear interpolation of the gap itself to produce synthetic data that match the daily patterns of the surrounding measured data. We did not fill gaps larger than 72 hours.

We found that in the data of interest for these projections, the variation in air temperature and insolation across the locations was quite small. Therefore, we took the arithmetic mean of the data over the seven stations to provide representative values of air temperature and insolation for the Delta. Since the climate projections to be used to force the projections provided only daily maximum and minimum air temperature, we used the hourly data to produce these quantities for our historical domain.

2.2.3 Forcing for Water Temperature Projections

Projected scenarios of daily air temperatures were used to evaluate potential impacts of climate change on water temperatures in the Delta. The scenarios were derived from simulations of 21st Century climate variations and trends by two global climate (or general circulation) models (GCMs) under each of two future global greenhouse-gas emissions scenarios. The GCMs used here were the Geophysical Fluid Dynamics Laboratory's (GFDL) CM2.1 coupled ocean-atmosphere GCM (Delworth et al. 2006) and the National Center for Atmospheric Research's Parallel Climate Model (PCM) coupled ocean-atmosphere GCM (Washington et al. 2000). Daily temperatures from

simulations by these two models, under A2 (rapidly accelerating) and B1 (eventually leveling) greenhouse-gas emissions scenarios, were obtained from the Program for Climate Diagnosis and Intercomparison at the Lawrence Livermore National Laboratory (Meehl et al. 2007). The GCM simulations were made on global grids with about 2 to 3° latitude and longitude resolution (about 250 km at the latitude of the Delta), and thus the original GCM scenarios were too spatially coarse for the purposes of this study. The GCM outputs were "downscaled" onto a 12-km grid over the conterminous US by a method called Constructed Analogs (Hidalgo et al. 2008). This statistical downscaling method is applied to each day's simulated climate condition in turn, and is based on fitting a linear combination of historical weather patterns (aggregated onto the GCM grid) that best reproduces the GCM pattern for the day. The coefficients necessary to make this linear fit are then applied to high-resolution versions of the weather on the same historical days. This approach ensures that, day by day, the weather simulated by the GCM is faithfully carried down to the 12-km scale, and tends to yield particularly realistic temperature relations across areas with sharp geographic gradients (Cayan et al. 2009). When applied to the historical record, as a validation exercise, the method reproduces daily temperature variations quite accurately on the 12-km grid given only historical temperatures as observed on the GCM grids as inputs (Hidalgo et al. 2008), indicating that the downscaled future-climate patterns are likely to also be realistic. The method was applied to climate simulations spanning the period from 1950-2100, to obtain daily, gridded temperature patterns of 21st Century warming over California and the Delta.

The air temperature data were sub-sampled for the Delta region, and then averaged to produce an equivalent forcing time series for 2000 though 2100 to those used during the calibration/verification stage. The data from the scenarios included maximum and minimum daily air temperatures. The climate projections did not provide insolation, so we derived the average insolation based on Julian day of the year. We extended this dataset to create a 100-year record under the assumption that insolation will be relatively constant over these climatic time scales.

2.3 Data Analysis

2.3.1 Temporal Variability

The daily water temperature data show strong yearly cycles as well as shorter time scale variation (Figure 2). Although short-term variation exists, the yearly cycle dominates at all Delta locations. The amplitude of the yearly cycle, however, varies from year to year and between locations. This is most apparent starting in 1998 at Ripon (station 3), where, following a particularly wet winter season, the summer peak temperatures are reduced for two years (discussed further below). Although shorter time scale variations are evident, yearly variations (on the order of 15°C at the locations in Figure 2-2) dominate the signal. These shorter time scale features are likely forced by a combination of short-term atmospheric conditions, local mixing, tidal advection of longitudinal temperature gradients, and possibly local precipitation.

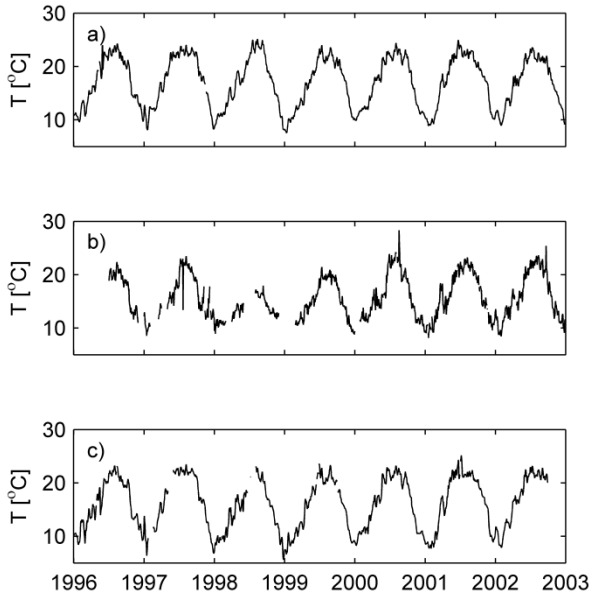

Figure 2-2. Daily-averaged water temperature at three locations from 1996-2003: (a) San Joaquin River at Antioch (station 2); (b) Ripon (station 3); (c) Rio Vista (station 15).

2.3.2 Spatial Variability

Once the water temperature data were processed, we performed a principal component analysis (PCA) on a subset of the data; the subset chosen was the eight stations (2, 3, 9, 10, 13, 14, 15, and 16) that had data from 1998 – 2002 because this was the longest uninterrupted dataset available. An overview of PCA can be found in Stacey et al. (2001); a more complete discussion is in Preisendorfer and Mobley (1988). This analysis is designed to decompose spatiotemporal data in such a way as to explain the maximum amount of total variance in the dataset in the first principal component (PC). Each principal component of a spatiotemporal dataset is a spatial structure which defines how strongly each station exhibits that mode of variation. A separate temporal structure, the amplitude of the principle component, defines the variability that is shared by the stations. Each successive principal component then explains the maximum amount of variability that remains in the dataset after removing the contributions of the previous principal components. All the PC's are mutually orthogonal to each other.

PCA at the eight locations that had data from 1998 through 2002 demonstrates the dominance of the yearly cycle in the temperature signal. Over 90% of the combined variance is described by the first principal component, whose amplitude represents the yearly cycle (Figure 2-3). Overland and Preisendorfer's (1982) test of significance ("Rule N") suggests that the higher modes of variation (PC2, 3, etc.) are not significant. In this test, the results of the PCA of the dataset of interest are compared to PCA of multiple random, normalized datasets to determine whether each principal component is significantly different from random noise. For this analysis, only PC1 passed Rule N, likely because autocorrelation in water temperatures caused so much variance to be captured in PC1, leaving so little left for higher modes of variation.

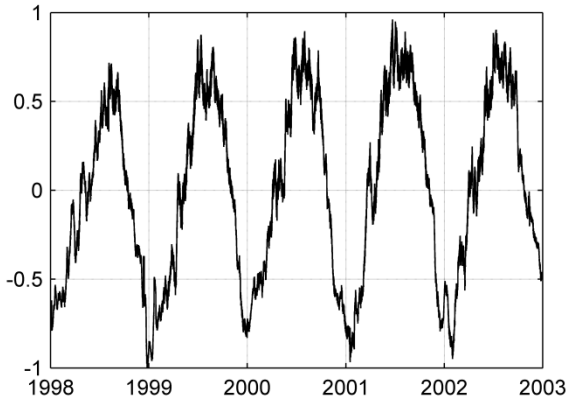

Figure 2-3. The amplitude of PC1 divided by its largest absolute value.

The PCA approach also displays spatial variability of the yearly cycle within the Delta (Figure 2-4). Annual variability was strong at all locations; but, notably, PC1 is strongest near the central Delta and weakest towards the edges (North, South, and West); these are areas dominated by single water sources (Sacramento River, San Joaquin River, San Francisco Bay tides, respectively.) This indicates that these peripheral locations have annual cycles somewhat independent of the rest of the Delta. The time variability in the central Delta is complicated by the interaction of the three main water sources; the mixing of waters from these three water sources causes water temperatures in the central Delta to be near-uniform spatially.

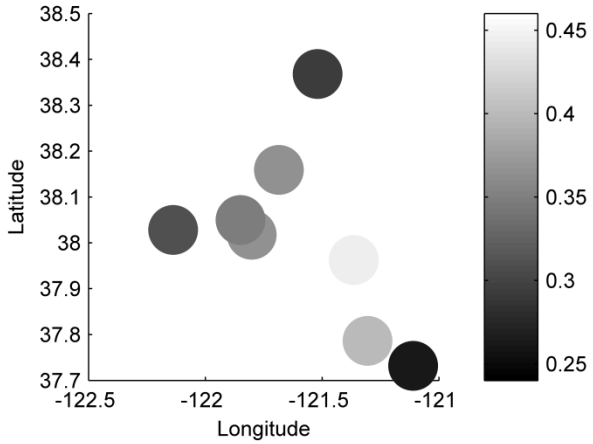

Figure 2-4. Principal component 1 (PC1) of the water temperature data for the years 1998-2002. The x-axis represents longitude and the y-axis represents latitude.

2.4. Methods

Water temperature has been modeled extensively over the years for a number of different locations. Modeling techniques have been split between deterministic models (Marce and Armengol 2008; Sinokrot and Stefan 1993; Uncles and Stephens 2001) and statistical models (Benyahya et al. 2007; Bradley et al. 1998; Caissie et al. 2001; Lemos et al. 2007; Marce and Armengol 2008; Mohseni et al. 1999). Our approach here is to create a statistical model, but one that is based on variables known to be important for deterministic models.

2.4.1 Development of Statistical Temperature Model

Assuming complete lateral and vertical mixing, the water temperature dynamics at a point in an estuarine channel can be defined

$$\frac{\partial T_w}{\partial t} + \frac{\partial U T_w}{\partial x} = \frac{\sum H}{\varrho_w z C_p} + \frac{\partial}{\partial x} K_x \left(\frac{\partial T_w}{\partial x}\right) \quad (2\text{-}1)$$

where T_w is water temperature, t is time, x is the direction of flow (along-axis), U is the velocity in the x-direction, H refers to atmospheric heat fluxes (defined below), ϱ_w is the density of water, z is the depth of the water column, C_p is the specific heat of water, and K_x is the dispersion coefficient in the x-direction. The atmospheric heat fluxes are broken down

$$\sum H = H_s + H_e + H_{l\downarrow} + H_{l\uparrow} + H_{sw}. \quad (2\text{-}2)$$

Following Fischer et al. (1979), Miyakoda and Rosati (1984) and Uncles and Stephens (2001), atmospheric heat fluxes [W/m^2] into the surface of a body of water can be defined using bulk formulae:

Sensible heat flux: $$H_s = \rho_a C_s C_{pa} W (T_a - T_w) \quad (2\text{-}3)$$

Evaporative heat loss: $$H_e = \rho_a C_e L_w W (Q_a - Q_w) \quad (2\text{-}4)$$

Long-wave heat radiation from water vapor: $$H_{l\downarrow} = 5.18 \times 10^{-13} (1 + 0.17 C^2)(273 + T_a)^6 \quad (2\text{-}5)$$

Long-wave heat loss from the water surface: $$H_{l\uparrow} = -5.23 \times 10^{-8} (273 + T_w)^4 \quad (2\text{-}6)$$

Short-wave radiation from insolation: $$H_{sw} = R(1 - \alpha) \quad (2\text{-}7)$$

For all heat fluxes, heating of the water column is represented by positive signs and cooling by negative. The symbols are defined as follows:

a Albedo, [dimensionless]

C Fractional cloud cover, [dimensionless]

C_e Empirical exchange coefficient, (~1.5 x 10^{-3}) [dimensionless]

C_s Empirical exchange coefficient, (~1.5 x 10^{-3}) [dimensionless]

C_{pa} The specific heat of air, (1.012 x 10^3 J/kg$^{\circ}$C)

L_w Latent heat of evaporation, (2.4 x 10^6 J/kg)

ϱ_a The density of air, (~ 1.2 kg/m^3)

R Insolation, [W/m^2]

Q_a Atmospheric mixing ratio (see Fischer et al. 1979), [dimensionless]

Q_w Saturation mixing ratio at the ocean surface for T_w, [dimensionless]

T_a Air temperature, [$^{\circ}$C]

T_w Water temperature, [°C]

W Wind speed at 10 m, [m/s]

Typical values of calculated atmospheric heat fluxes within the Delta (Table 2-1) show the dominance of the long-wave and short-wave radiation terms.

Stockton-Manteca						
Month	H_s	H_e	$H_{l\uparrow}$	$H_{l\downarrow}$	H_{sw}	$\sum H$
January	-3.5	-9.3	-331.0	270.6	55.0	-18.3
August	-12.0	-102.3	-416.4	346.8	277.0	93.1

Table 2-1: Typical values for the surface heat fluxes into (+) and out of (-) the water column for Stockton Ship Canal at Burns Cutoff (station 10).

Bartholow (1989) observed that river water temperatures are typically not influenced by reservoirs more than 25-30 km upstream. This suggests that $\frac{\partial T_w}{\partial x}$ is likely to be small and contributions from terms dependent on this gradient, advection and diffusion, are small by the time a water parcel reaches the Delta. Thus, combining equations (2-1) and (2-2) and eliminating terms, we can write:

$$\frac{dT_w}{dt} \cong \frac{H_{l\downarrow}+H_{l\uparrow}+H_{sw}}{\rho_w z C_p} \tag{2-8}$$

Or, simplified even further:

$$\frac{dT_w}{dt} \cong f(T_a, T_w, R) \tag{2-9}$$

Equation (2-9) could be discretized as

$$T(t) \cong T(t-\Delta t) + \Delta t\big(f(T_a, T, R)\big), \tag{2-10}$$

where T represents modeled water temperature; we drop the subscript w in order to emphasize that the model's predicted water temperature will depend on the model's output from the previous time step and not on measured values. Equation (2-10), although deterministic, is the basis for our statistical model. Based on the historical water temperature data, we applied a simple regression to relate the day's water temperature to the air temperature and insolation from the same day and water temperature from the day preceding it:

$$T(n) = aT_a(n) + bT(n-1) + cR(n) + d \tag{2-11}$$

where n is the day on which the temperature is being calculated, a is the coefficient on the current day's air temperature, b is the coefficient on the previous days water temperature, c is the coefficient on the current day's insolation, and d is a constant offset. This model can be used to model maximum, minimum, or average water temperatures. The insolation, R, used was the average insolation for each Julian day of the year.

We used our regression model to accurately reconstruct historical water temperatures with a minimal amount of data needs or computational cost. To verify the model, we calculated regression coefficients for equation (2-11) using the first half of the dataset (the calibration period), then used these coefficients to force the model during the entire dataset (both calibration and verification

periods). To project water temperatures for the coming century, we calibrated with the entire historical dataset and forced with the downscaled climate data and the annual insolation cycle.

2.4.2 Performance Metrics

We measured model performance through the root mean squared error (*RMSE*), the coefficient of determination (R^2), and the Nash-Sutcliffe Coefficient (*NSC*). The first gives an idea of the magnitude of the errors. The latter two quantify how well the model performed on the whole.

The final metric, the Nash-Sutcliffe Coefficient, has been used widely to evaluate the performance of hydrologic models and is defined (Nash and Sutcliffe 1970) as

$$NSC = 1 - \frac{\sum_{i=1}^{N}(O_i - P_i)^2}{\sum_{i=1}^{N}(O_i - \bar{O})^2}, \tag{2-12}$$

where *O* represents observed data with *N* realizations and *P* represents predicted data. Values of *NSC* range from -∞ to 1.0. Higher values indicate better agreement. A value of zero indicates that the predicted values are no better than the mean of the observations as a predictor; negative values indicate that the observed mean is a better predictor. The *NSC* has been criticized as a metric because it (like R^2) gives too much weight to outliers. Additionally, Garrick et al. (1978) have argued that it is possible to get high values for the *NSC* with poor models while good models do not score much higher.

2.5 Results

2.5.1 Calibration and Verification of Statistical Temperature Model

Figure 2-5 presents time series of the calibration and verification periods from a long-term record on the San Joaquin River at Antioch (station 2). The annual cycle is clearly well-predicted, as are shorter time scale variations, particularly weekly to monthly fluctuations. A more difficult test is shown in Figure 2-6, for which temperature data were only collected during the spring at San Joaquin River at Prisoner's Point (station 5); the model was still able to capture the annual cycle sampled at the end of the verification period. This is most likely because the range of the data was close to the annual range in temperature.

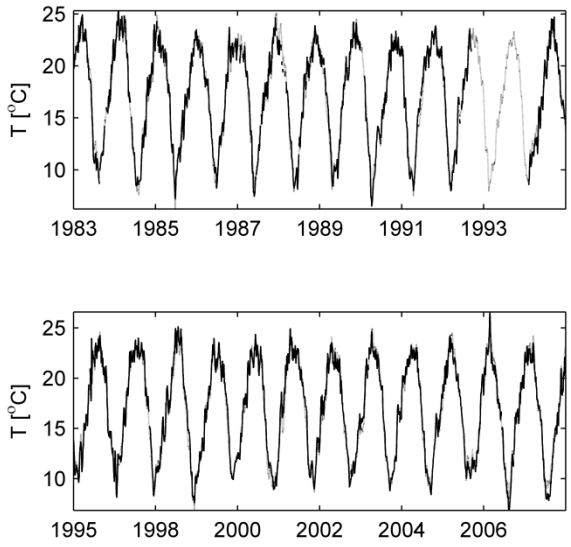

Figure 2-5. Calibration (a) and verification (b) at the San Joaquin River at Antioch (station 2). The measured values are indicated with the solid line; the modeled values are indicated with the grey line. The calibration R^2 was 0.981; verification R^2 was 0.978.

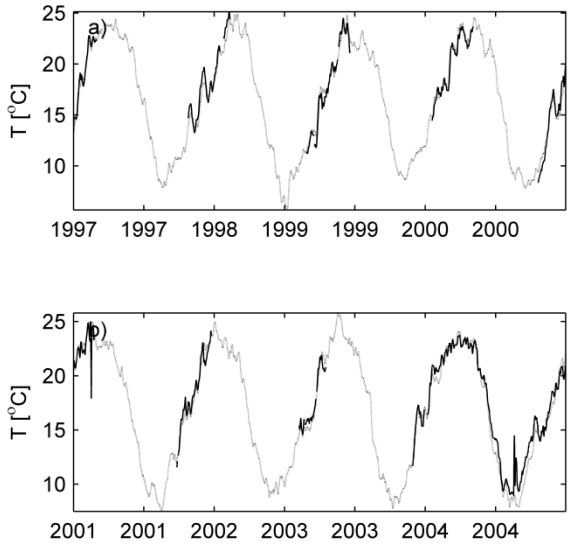

Figure 2-6. Calibration (a) and verification (b) at San Joaquin River at Prisoner's Point (station 5). R^2 values are 0.976 for calibration and 0.974 for verification.

The model performed very well at locations where more than 1 year of data were available for calibration. After locations with less than one year of data were removed, the model fit the data well (Table 2-2) with R^2 values greater than 0.930 (and generally over 0.965) and *NSC* values greater than 0.890 (and generally over 0.950) for verification periods for all locations except Ripon (station 3), which is on the Stanislaus River and farther from tidal influence than the other stations.

The modeled temperatures match the measured temperatures very well. This is due, in part, to the strong seasonality of the water temperatures. The three predictor variables (insolation, air temperature, and lagged water temperature) all have strong seasonality. Because these three are strongly correlated with each other (and the variables are not of the same scale), the coefficients do not necessarily inform us much with regard to the importance of each term to the overall model's performance.

Station		*RMSE* - Cal [°C]	*RMSE* - Ver [°C]	R^2 - Cal	R^2 - Ver	*NSC* - Cal	*NSC* - Ver
2	T_{max}	0.74	0.78	0.98	0.97	0.98	0.97
	T	0.66	0.70	0.98	0.98	0.98	0.98
	T_{min}	0.67	0.71	0.98	0.98	0.98	0.98
3	T_{max}	1.88	2.06	0.79	0.89	0.79	0.80
	T	1.74	1.90	0.79	0.89	0.79	0.80
	T_{min}	1.63	1.52	0.78	0.92	0.78	0.85
5	T_{max}	0.65	1.42	0.97	0.93	0.97	0.89
	T	0.65	0.90	0.97	0.98	0.97	0.95
	T_{min}	0.64	0.98	0.97	0.97	0.97	0.94
6	T_{max}	0.68	0.77	0.97	0.97	0.97	0.96
	T	0.63	0.69	0.98	0.97	0.98	0.97
	T_{min}	0.63	0.70	0.97	0.97	0.97	0.97
9	T_{max}	0.85	0.89	0.96	0.96	0.96	0.96
	T	0.75	0.73	0.97	0.97	0.97	0.97
	T_{min}	0.72	0.77	0.97	0.96	0.97	0.96
10	T_{max}	1.17	1.00	0.96	0.97	0.96	0.97
	T	1.17	1.00	0.96	0.97	0.96	0.97
	T_{min}	1.18	1.04	0.96	0.97	0.96	0.97
13	T_{max}	1.36	0.97	0.91	0.96	0.91	0.96
	T	1.08	0.75	0.94	0.97	0.94	0.97
	T_{min}	1.01	0.85	0.95	0.96	0.95	0.96
14	T_{max}	1.21	1.23	0.96	0.95	0.96	0.95
	T	1.20	1.22	0.95	0.95	0.95	0.95
	T_{min}	1.20	1.23	0.95	0.95	0.95	0.95
15	T_{max}	0.92	0.93	0.97	0.97	0.97	0.96
	T	0.94	0.94	0.97	0.96	0.97	0.96
	T_{min}	0.94	0.96	0.97	0.96	0.97	0.96
16	T_{max}	0.86	1.13	0.97	0.97	0.97	0.96
	T	0.84	1.10	0.97	0.97	0.97	0.96
	T_{min}	0.83	1.09	0.97	0.97	0.97	0.96

Table 2-2. Model performance. This table lists calculated performance metrics for each variable modeled at each location with at least one year of calibration data for both calibration (Cal) and verification (Ver) periods. The performance metrics are abbreviated root mean squared error (*RMSE*), the coefficient of determination (R^2), and the Nash-Sutcliffe Coefficient (*NSC*).

2.5.2 Projections of Water Temperatures for Climate Scenarios

Model projections predict long-term changes in water temperatures throughout the Delta. (Model coefficients are reported in Table 2-3.)

		a	b	c	d
2	T_{max}	0.393 ± 0.027	0.080 ± 0.003	0.890 ± 0.004	0.001 ± 0.000
	T	0.283 ± 0.017	0.068 ± 0.002	0.909 ± 0.002	0.001 ± 0.000
	T_{min}	0.263 ± 0.020	0.063 ± 0.002	0.913 ± 0.003	0.001 ± 0.000

	T_{max}	0.434 ± 0.096	0.079 ± 0.009	0.890 ± 0.011	0.001 ± 0.000
	T	0.406 ± 0.081	0.080 ± 0.007	0.891 ± 0.010	0.000 ± 0.000
3	T_{min}	0.647 ± 0.109	0.094 ± 0.010	0.850 ± 0.014	0.000 ± 0.001
	T_{max}	0.755 ± 0.198	0.114 ± 0.016	0.811 ± 0.023	0.004 ± 0.001
	T	0.343 ± 0.078	0.076 ± 0.006	0.889 ± 0.010	0.002 ± 0.000
5	T_{min}	0.314 ± 0.092	0.074 ± 0.008	0.891 ± 0.012	0.002 ± 0.001
	T_{max}	0.427 ± 0.043	0.057 ± 0.004	0.905 ± 0.006	0.001 ± 0.000
	T	0.304 ± 0.021	0.050 ± 0.002	0.922 ± 0.003	0.001 ± 0.000
6	T_{min}	0.289 ± 0.026	0.050 ± 0.002	0.922 ± 0.004	0.001 ± 0.000
	T_{max}	0.596 ± 0.045	0.082 ± 0.004	0.871 ± 0.006	0.001 ± 0.000
	T	0.383 ± 0.026	0.060 ± 0.002	0.909 ± 0.003	0.001 ± 0.000
9	T_{min}	0.377 ± 0.032	0.059 ± 0.003	0.907 ± 0.004	0.001 ± 0.000
	T_{max}	0.130 ± 0.027	0.082 ± 0.003	0.900 ± 0.004	0.002 ± 0.000
	T	0.090 ± 0.015	0.062 ± 0.002	0.922 ± 0.002	0.001 ± 0.000
10	T_{min}	0.086 ± 0.018	0.058 ± 0.002	0.926 ± 0.003	0.001 ± 0.000
	T_{max}	0.536 ± 0.055	0.091 ± 0.005	0.866 ± 0.007	0.001 ± 0.000
	T	0.299 ± 0.025	0.066 ± 0.002	0.908 ± 0.003	0.001 ± 0.000
13	T_{min}	0.425 ± 0.045	0.076 ± 0.004	0.883 ± 0.006	0.001 ± 0.000
	T_{max}	0.398 ± 0.043	0.137 ± 0.005	0.825 ± 0.006	0.003 ± 0.000
	T	0.323 ± 0.039	0.130 ± 0.004	0.835 ± 0.006	0.002 ± 0.000
14	T_{min}	0.298 ± 0.042	0.129 ± 0.005	0.835 ± 0.006	0.002 ± 0.000
	T_{max}	0.226 ± 0.024	0.078 ± 0.003	0.895 ± 0.004	0.001 ± 0.000
	T	0.171 ± 0.018	0.069 ± 0.002	0.908 ± 0.003	0.001 ± 0.000
15	T_{min}	0.147 ± 0.020	0.065 ± 0.002	0.913 ± 0.003	0.001 ± 0.000
	T_{max}	0.204 ± 0.050	0.077 ± 0.006	0.896 ± 0.008	0.001 ± 0.000
	T	0.184 ± 0.046	0.073 ± 0.006	0.901 ± 0.008	0.001 ± 0.000
16	T_{min}	0.179 ± 0.051	0.072 ± 0.006	0.901 ± 0.008	0.001 ± 0.000

Table 2-3. Model coefficients and their 95% confidence intervals at locations with at least one year of calibration data.

Figure 2-7 shows an example of these projections, showing projected water temperatures on the San Joaquin River at Antioch (station 2) under PCM A2 forcing. In this particular case, water temperature over the 100 year time horizon increases both the yearly high and yearly low temperatures.

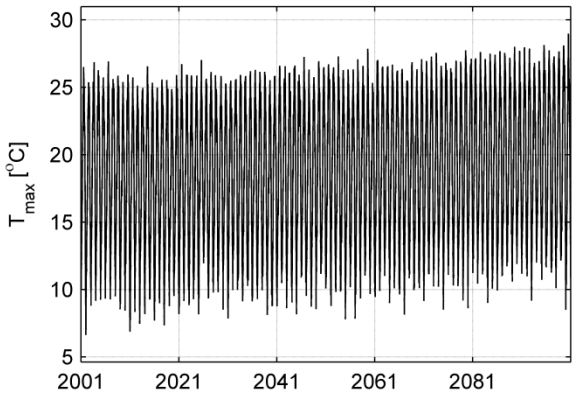

Figure 2-7. 100-year projection of daily max water temperatures on the San Joaquin River at Antioch (station 2) under PCM A2 forcing.

2.6 Discussion

2.6.1 Model Limitations

One major concern is the ability of a statistical model to project water temperatures in a changing system. The model predicts the seasonal cycle as well as capturing much of the short-term variability compared to measured data. These seasonal fluctuations (the dominant mode of variability) are much larger than the long-term trends expected with climate change. On the other hand, increases in water temperatures could lead to increases in evaporative cooling and ultimately cause a leveling off of water temperatures near some maximum (Mohseni et al. 1999). While this dynamic is not included in the model, the model is effective at predicting the maximum temperatures contained in the historical record of the current regime.

While this approach has been successful at reproducing water temperatures at locations of long-term records, the local spatial variability of the system is not captured. The statistical approach essentially projects the water temperature that would be measured at the instrumentation site. It is unclear if those temperature measurements are representative of the local or regional water temperature. Depending on the station and the method of deployment of the instrument, there are likely to be both lateral and vertical gradients in water temperature that would reduce the applicability of the results for locations other than the instrument sites. Further, variation between stations may not be linear, but may change abruptly at channel junctions or other Delta features. Finally, all of the long-term stations are located along either the Sacramento or San Joaquin River channels, so the applicability of the results to other sloughs and channels in the Delta is unclear.

2.6.2 Flow Effects

The model skill evident in our verification periods indicates that riverine flows are not required to effectively predict water temperatures in the Delta on long time scales. However, on shorter time scales, large flows create features that the model is unable to accurately forecast.

Although flow effects on water temperatures are, to great extent, overwhelmed by atmospheric influences, flow does appear to have significant effects over shorter time scales, and some events have longer term implications. We performed a PCA on water temperature data from

the same eight stations from section 2.3.2 for each year individually from 1998-2002 to evaluate the inter-year stability of the annual cycle. The amplitide of PC1 for each of these years is similar; the yearly cycle is evident as it ranges from -20 in the beginning of the year to +20 in the middle of the year and back to -20 at the end. The comparison of the first PC (the yearly cycle) for these years (Figure 2-8) shows a temporary increase in the strength of this PC over the western Delta and a weakening of this PC at Ripon (station 3), the most eastern station and the one farthest from tidal influence.

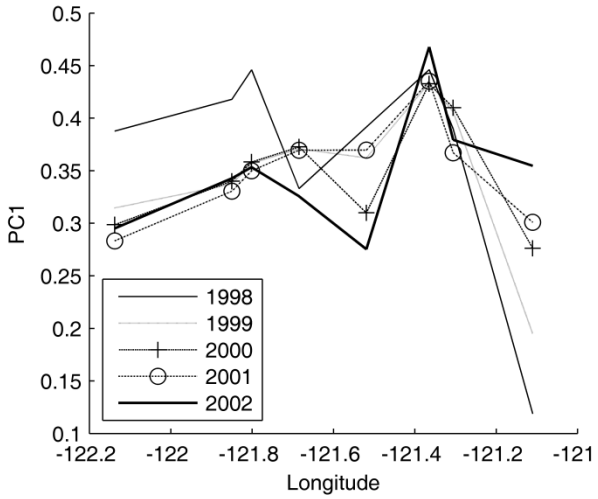

Figure 2-8. PC1 for each year from 1998 to 2002 taken individually for the stations that had data for that time period (2, 3, 9, 10, 13, 14, 15, and 16). The x-axis represents longitude and the y-axis represents PC1.

This shift comes in conjunction with a large El Niño with accompanying large flows during the winter of 1997-1998. The western stations have higher PC1 for 1998 than for other years, perhaps because high flows of that year forced a downstream shift of the interaction of Bay and river waters, making the western stations more like the up-estuary reaches of the Delta during a typical year. The western stations recovered their normal yearly cycle within one year; Ripon does not re-align with the Delta until 2002. This is presumably the result of elevated reservoir releases that persisted for more than a year following the large flows of 1997-1998.

Another notable example of this effect is at Rio Vista (station 15) on the Sacramento River. Water temperatures were lower than predicted during the exceptionally high flows of the 1997-1998 winter, but once the water temperatures began to warm in the spring, the model prediction again matched the observations (Figure 2-9). Bartholow's (1989) observations indicate that it is unlikely that this divergence in model performance is caused by influence from upstream dam releases; more likely, this divergence is due to either local precipitation and run off or changes in mixing in the north Delta region. Through model calibration using data that spans multiple years, the model is optimally designed to capture as much variability as possible during a typical year for a location, including accounting for the relative contributions of San Francisco Bay and riverine waters at a site. During high flow events, riverine influences on Delta water temperatures increase while Bay influence decreases. This affects the thermal dynamics at a site across years, just as it affects it within years.

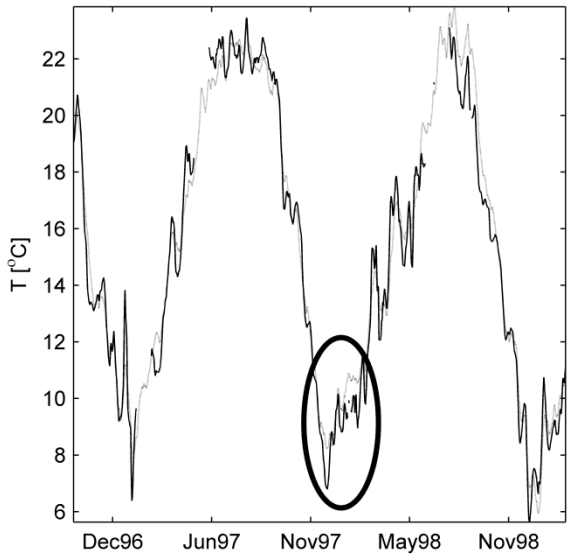

Figure 2-9. Short-term model deviations due to large flows on the Sacramento River at Rio Vista (station 15). The measured values are indicated with the solid line; the modeled values are indicated with the grey line. The circle highlights model deviations from measurements during the winter of 1997-1998.

Further, the inundation of the Yolo Bypass (a flood plain conveyance that is active during high flows) may have altered the thermal dynamics in the vicinity of Rio Vista, which is near the outflow of the Bypass. In the Rio Vista example (Figure 2-9), high flows are associated with lower temperatures during model divergences for a period of a couple of months. However, once spring warming began in March, the model converges on the observed temperatures, including two warming-cooling events in March and April. Notably, the model also diverges during the following summer prior to cooling during the fall.

Another process that might cause short-term anomalies in model performance is the effect of flows on thermal dispersion within the Delta. Monismith et al. (2009) found a strong positive correlation between the thermal dispersion coefficient and river flow along the San Joaquin River. A visual analysis of the residuals of our model (Figure 2-10) indicates that flows may have an effect on the performance of the model in this area of the Delta; however, the correlation between residuals and flows ($R^2 = 0.14$) is low enough that integrating flow into the model is unlikely to improve performance. Similar analyses at locations on the Sacramento River show no correlation between residuals and flow (max $R^2 = 0.07$).

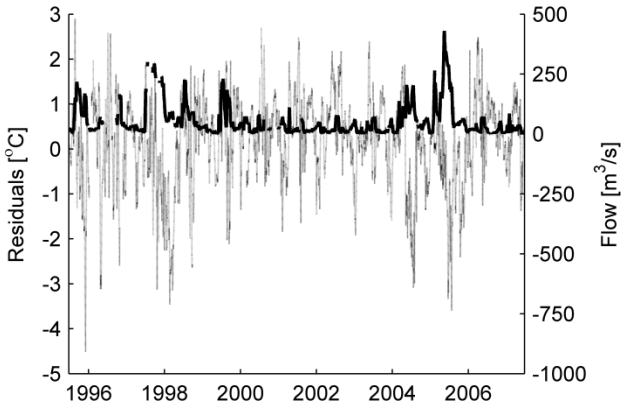

Figure 2-10. Potential flow effects on model performance at Stockton Ship Channel at Burns Cutoff (station 10). The grey line represents the model residuals (measured temperature minus modeled temperature) at station 10; the thick black line represents San Joaquin River flows nearby at the Garwood Bridge.

2.6.3 Temperature Trends

Under the selected climate change scenarios, both daily maximum and daily minimum water temperatures are expected to increase. This increase varies from one scenario to another and from one location to another within each scenario. For example, a comparison of the predicted yearly cycle of the daily average temperature at Rio Vista (station 15) in 2090 yields very different results for each of the 4 scenarios (Figure 2-11). Under all of our climate scenarios, the yearly cycle peaks later in the year than in 1997-1999, with the GFDL A2 scenario giving a sharper, higher peak than the others. All four projections are considerably warmer (~3-6°C) in late summer than 1997-1999.

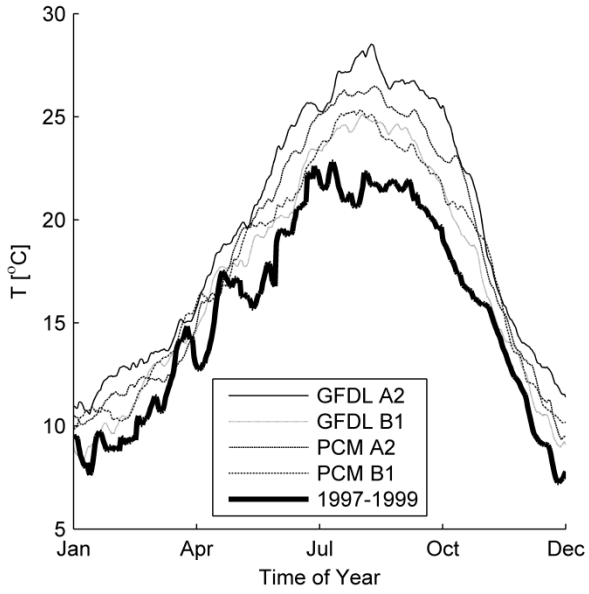

Figure 11: Projected yearly cycle of water temperatures at Sacramento River at Rio Vista (station 15) averaged from 2097-2099. The mean of the measured water temperatures at the same location from 1997-1999 is included for comparison.

2.6.4 Ecological Implications

One informative way to evaluate the increase in water temperatures is to look at ecological thresholds. The Delta smelt, a federally listed threatened species endemic to the Delta, has high mortality above a temperature of about 25^{0}C (Bennett 2005). If we look at the number of days at a location that the daily maximum temperature exceeds the 25^{0}C threshold, then temperature trends (from an ecological standpoint) become easier to see. Although all areas are projected to warm in response to increased air temperatures, the ecological effects would not be uniform across the Delta (Figure 2-12). Notably, the Sacramento corridor shows the greatest change with respect to this threshold, mostly because other areas of the Delta are already frequently exceeding the threshold.

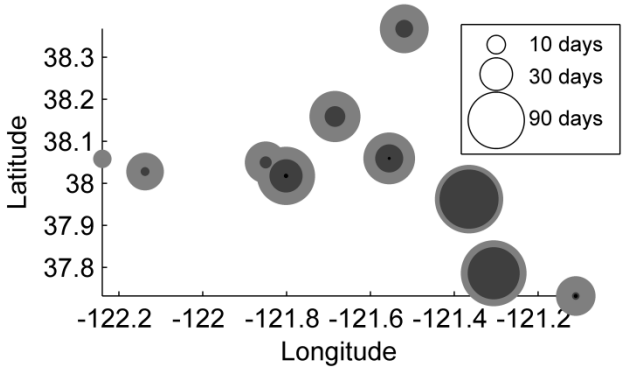

Figure 2-12. Spatial variability in heating. Dot area is proportional to the average number of days per year exceeding 25^{0}C (the Delta smelt's thermal limit) at each location under GFDL A2 forcing. The black dots represent the measured data; the dark grey dots are for 2010-2030; the light grey dots are for 2070-2090.

Delta smelt require water temperatures between about 15^{o}C and 20^{o}C during spring months for spawning, and juvenile delta smelt are stressed between 20^{o}C and 25^{o}C during the summer (William Bennett, personal communication). Since the spawning temperatures occur during the spring warming cycle and the rate of warming is relatively insensitive to climate change scenarios, the number of days within these ranges does not change much in response to climate change (Figure 2-13), but the timing can be affected.

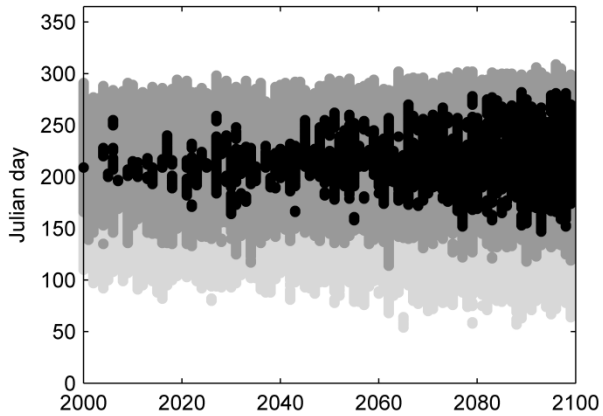

Figure 2-13. Long-term shift in water temperatures on the Sacramento River at Rio Vista (station 15) under GFDL A2 forcing. Using projected temperatures, each day is grouped as it impacts the Delta smelt: spring spawning (daily average temperatures from 15 – 20°C in light grey), stress (daily average temperatures from 20 – 25°C in dark grey), and lethal (daily maximum temperatures > 25°C in black).

If the timing of the temperature variations in these ranges were to drift out of phase with other ecological variables (i.e. flows, sunlight, etc.), it could have an important impact on the populations of these species. Over the 100 years projected here, the model predicted shifts on the order of 10-15 days of the median day of the spawning period under 3 of our 4 scenarios (Figure 2-14). The fourth scenario, GFDL A2, would cause the greatest shifts, on the order of 25 days.

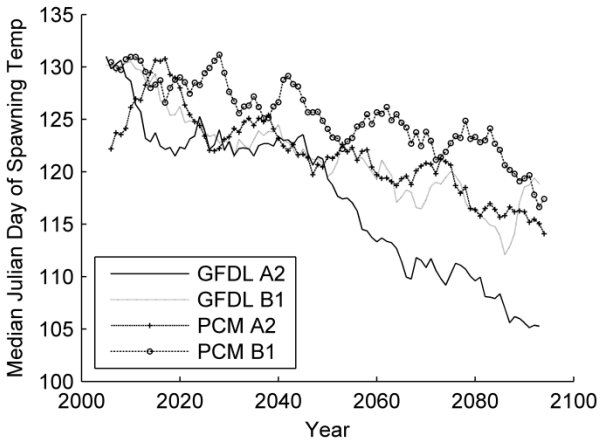

Figure 2-14. Projected shift in the median day of the spawning period due to temperature on the Sacramento River at Rio Vista (station 15). The median day of the spawning period was calculated for each year under each scenario. The medians were smoothed with a 10-year running average.

2.7 Summary

We present a simple, computationally efficient model for water temperatures within the Sacramento-San Joaquin Delta. The statistical model is based on physical principles; calibration and verification demonstrate the ability of our statistical approach. The model's skill allows consideration of the long term effects of climate change on water temperatures. Driven by climate change scenarios, the model forecasts considerable changes throughout the Delta. These changes will affect ecosystem function in a variety of ways. For example, timing of spring spawning temperatures for Delta smelt will shift earlier in the year. Lethal temperatures for Delta smelt will be more frequent in all four climate scenarios.

Our approach has potential weaknesses. While model forecasts appear to predict that Delta smelt are doomed under some climate change scenarios, the forecasts are spatially limited and do not account for thermal refugia which may exist within the Delta. Additionally, model calibration utilized data collected from 1983 through 2007 and did not sample the same range of temperatures that are likely to be seen in the future. We expect the long-term trend, however, to be small relative to the yearly cycle, and we expect the calculated coefficients to be robust. Flow regimes and water depths in the Delta might be expected to change in the future, as snowmelt arrives earlier and sea level rises. We expect the flow regime to have little effect on the effectiveness of the model; however, it will play a role in setting temperature dynamics over shorter time scales, as it controls the balance between riverine and Bay influences within the Delta.

Chapter 3

Mixing and Thermal Dynamics in a Shallow Tidal Slough System

3.0 Introduction

Tidal channel systems confound simple modeling efforts for resolving small-scale advection and mixing processes within them. These processes determine the creation and breakdown of gradients of ecologically important scalars (e.g. salt or temperature). In light of this, field measurements and work is necessary to parse the effects of within channel transport and mixing on the region's thermal environment, including the effects of exchanges between intersecting channels or between channels and shallow habitats.

3.0.1: Research Questions

We present results of two field campaigns to assess thermal regimes in the Cache Slough/Liberty Island (CSLI) complex within California's Sacramento-San Joaquin Delta (the Delta). The CSLI complex is singled out because it is "typical" within the Delta, containing tidal sloughs, flooded "islands," and the input of freshwater from the nearby Sacramento River, but also because it has been identified as a model for future restoration efforts in the Delta due to discovery of important species using the flooded island as habitat. In this paper, we will analyze 1) water temperature dynamics within a channel cross section of Cache Slough, 2) lateral momentum within that cross section, 3) along-channel mixing along Cache Slough, and 4) the interplay between the three. Further, we will specifically look at the role wind plays in this system. While wind appears to have had a temporally dominant role in the lateral momentum budget, it does not appear to have had nearly the same influence on water temperatures or along-channel mixing, despite the interconnectedness of the three processes.

3.0.2: Background

3.0.2.1 Water Temperature

In freshwater and estuarine ecosystems, water temperature provides an important constraint on ecological function (Coutant 1976). Water temperature affects fish spawning (Hotta et al. 2001; Wagner et al. 2011), swimming performance (Myrick and Cech 2000), metabolism (Das et al. 2005; Scheller et al. 1999), and mortality (Coutant 1976; Johnson and Evans 1996) as well as almost all aspects of the life cycles of aquatic invertebrates (Vannote and Sweeney 1980; Ward and Stanford 1982). Species of concern within the Sacramento-San Joaquin Delta that are sensitive to water temperatures at various points in the life cycles include the Sacramento winter run Chinook salmon *Oncorhynchus tshawytscha* (Baker et al. 1995), the Sacramento splittail *Pogonichthys macrolepidotus* (Moyle et al. 2004), and the delta smelt *Hypomesus transpacificus* (Bennett 2005; Swanson et al. 2000; Wagner et al. 2011).

3.0.2.2 Estuarine Mixing - Lateral and Along-Channel

Much work has been done to quantify mixing in estuarine channels, in part because the along-channel salinity field defines the very length of the estuary itself (Chant 2002), but also because salinity (and temperature and sediment) affects the physical dynamics of the estuary by modifying the density field. While estuarine fronts have been shown to be important

hydrodynamically, they also matter because of their role in estuarine productivity (Largier 1993). Mixing is important because it drives the creation and breakdown of these fronts, but also because of the ecological importance of the scalars being mixed, whether temperature (Lankford and Targett 1994; Rakocinski et al. 1992; Wagner et al. 2011), salinity (Crump et al. 2004; Haller et al. 1974; Lankford and Targett 1994; Rakocinski et al. 1992; Stevenson 1988; Williams 1964), dissolved oxygen (Dauer et al. 1992; Rakocinski et al. 1992; Yin et al. 2004), turbidity (Cyrus and Blaber 1987; Fisher et al. 1988; Pennock 1985), nutrients (Eyre 2000; Fisher et al. 1988; Yin et al. 2000), or larvae (Cronin 1982; Fortier and Leggett 1982; Stancyk and Feller 1986). Jassby et al. (1995) noted the strong relationship between X2, the location of the 2 psu salinity line in San Francisco Bay, and multiple metrics of the estuary's productivity.

Although most work on estuarine mixing focuses on along-channel processes, there is a growing body of work on lateral dynamics within an estuary. One reason for the new interest in lateral dynamics is the feedback between lateral processes and along-channel transport (Fischer et al. 1979; Geyer et al. 2008; Lerczak and Geyer 2004). Lacy et al. (2003) scaled the relative importance of lateral advection to along-channel momentum in northern San Francisco Bay. Many studies (e.g. Burchard et al. 2011; Cheng et al. 2009; Lerczak and Geyer 2004; Nunes and Simpson 1985) discuss lateral circulations created by lateral density gradients formed from differential advection of an along-channel density gradient. Other studies have analyzed lateral circulations formed as an interaction between along-channel flows and bathymetry (Valle-Levinson et al. 2000), due to channel curvature (Chant 2002; Kalkwijk and Booij 1986; Lacy and Monismith 2001), or due to Coriolis effects (Kalkwijk and Booij 1986; Lerczak and Geyer 2004). Importantly, stratification within the estuary has been shown to limit secondary circulations (Chant 2002; Lacy and Monismith 2001; Lerczak and Geyer 2004, for example.)

Turbulence acts as an along-channel mixing agent; but shear dispersion, the interaction between differential advection of a concentration field and turbulence, is a much more effective agent (Fischer et al. 1979). Turbulence prevents the differential advection from undoing its work on the return tide by mixing out the gradients formed across the cross section. Shear dispersion is typically thought as being due to vertical shear, but Geyer et al. (2008) observed the time-dependent dominance of lateral shear on this process. Other along-channel processes, like tidal trapping (MacVean and Stacey 2010; Okubo 1973) and tidal pumping (Fischer et al. 1979) can be even more effective mixers in complex branching systems over time scales longer than tidal. However, the scalar of interest in this study, temperature, is not conserved and likely would not be a good choice for studying mixing processes since the system's thermal memory is likely too short to allow robust quantification.

3.0.2.3 Interactions between Water Temperature, Lateral Dynamics, and Along-Channel Dynamics

Lateral mixing processes can limit the differential advection by homogenizing the along-channel velocity and thus shutting off shear dispersion. Conversely, in oscillating shear flow, if turbulent mixing times across the shear direction were longer than the oscillation time scale, weak lateral shear dispersion could, without effectively limiting the along-channel shear, act as the turbulent agent in mixing out across-channel concentration gradients created by differential advection. This would, in effect, increase shear dispersion in the case of weak turbulence, since across-shear mixing would be necessary to prevent along-shear spreading from un-spreading when the flow reverses. Differential advection of the salinity field, as observed by Lacy et al. (2003), can drive lateral circulation through the creation of lateral density gradients. In Cache Slough,

differential along-channel advection of the temperature field could have the same effect, which could feed back into the along-channel mixing. Our initial hypothesis was that three processes (water temperature dynamics, lateral circulation, and along-channel mixing) and their interactions would together define the structure and variability of tidal flows within Cache Slough. We found, however, that wind dominated the lateral momentum equation during high wind events.

3.0.2.4 Wind Effects on Estuaries

Although there has been much work on lateral momentum and its forcings in estuaries, most of it does not consider wind effects. Uncles and Stephens (2011), Chen et al. (2009), Chen and Sanford (2009) and Scully et al. (2005) are good examples of work that emphasizes wind effects, but these papers study along-channel winds, ignoring across-channel winds. This is a logical approach since fetch lengths are limited across estuarine channels, but it ignores the possible importance of lateral winds forcing lateral shear and mixing. Scully et al (2005) noted the role along-channel winds have in increasing vertical stratification due to straining of the along-channel salinity gradient, contrary to previously held assumptions about wind stirring increasing vertical homogeneity. North et al. (2004) studied wind effects on Chesapeake Bay numerically and observationally. Interestingly, their observational studies showed winds from a variety of directions, but they applied wind in only either up-estuary or down-estuary directions for their numerical studies. They found that the salt field moved in the opposite direction as the wind direction; i.e. the salt field moved down-estuary in respond to up-estuary winds. In both Uncles and Stephens (2011) and Chen et al. (2009), along-channel winds create lateral gradients, which in turn drive lateral circulation. Another logical approach would be to consider the effects of lateral winds on lateral circulation. We attempt to fill this gap here.

3.1 Site Overview

This study focuses on the Cache Slough/Liberty Island complex (CSLI) of California's Sacramento–San Joaquin Delta (the Delta), which are located towards the upstream end of the San Francisco Estuary. Detailed descriptions of the Delta can be found in Kimmerer (2004) and Lund et al. (2007). The Delta consists of a network of channels (Figure 3-1) that are fed by freshwater flow from a number of rivers that drain California's Central Valley, most significantly the Sacramento and San Joaquin Rivers (Kimmerer 2004). The CSLI complex is a region of the Delta that has recently come to the attention of researchers due to the discovery of its use by species noted as part of the Pelagic Organism Decline (POD), first noted in the early 2000s (Sommer et al. 2007): the delta smelt, threadfin shad, and the striped bass. Moyle (2008) discusses the high restoration potential for this region.

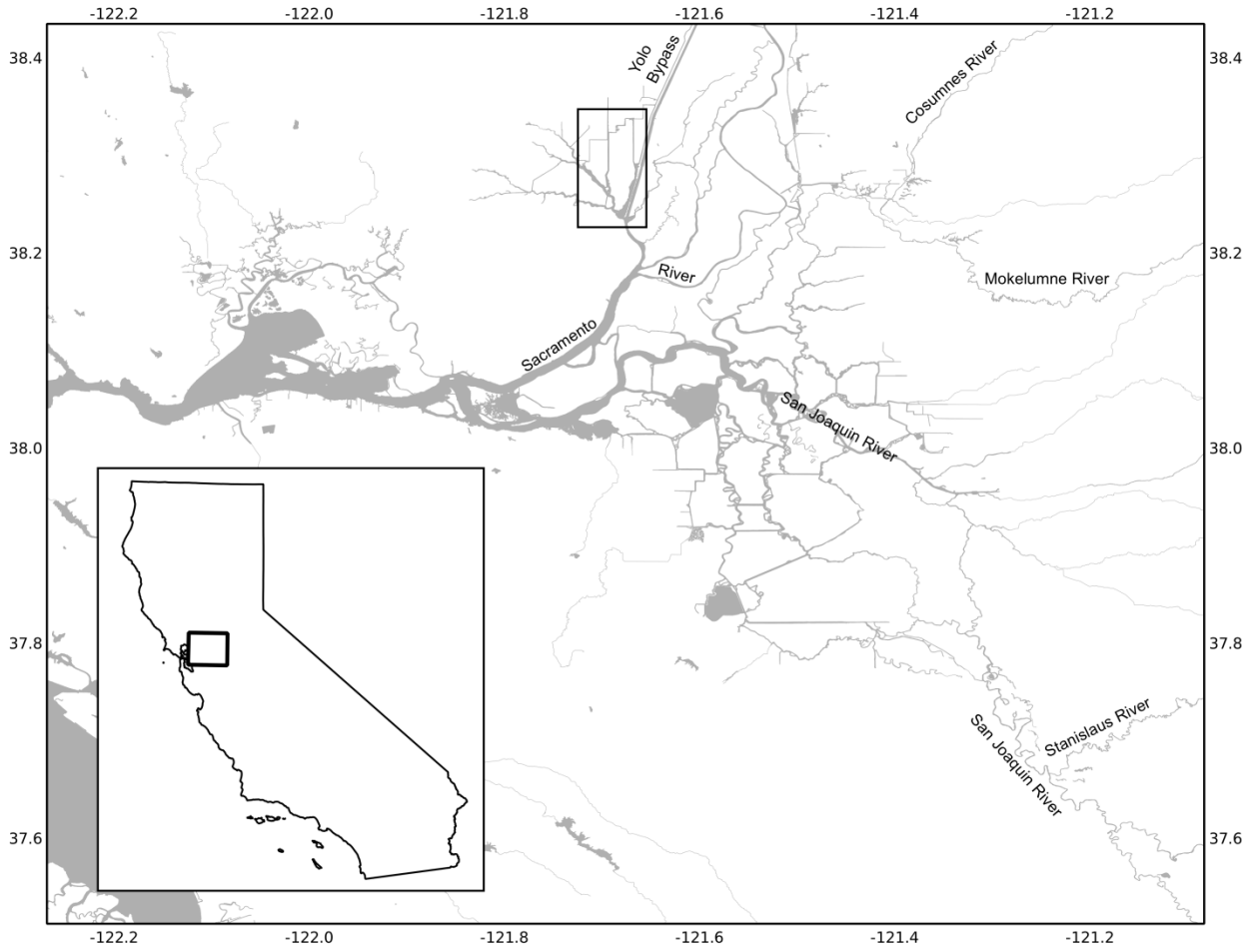

Figure 3-1. California's Sacramento-San Joaquin Delta and environs. The Delta is fed primarily from tides from San Fancisco Bay, and freshwater from the Sacramento River in the north and the San Joaquin River in the South. The Cache Slough/Liberty Island complex (Figure 3-2) is boxed in.

Liberty Island (Fig 3-2) is a flooded island in the northern portion of the Delta, roughly 8 miles north and west of Rio Vista, CA. After a series of unplanned floods in the 1990s, the Liberty Island levees breached in 1997 and were abandoned in 1998 (Moyle 2008) and the island remained flooded. The southern levee was breached to restore tidal action to the island. The northern portion is still high enough to form a marsh, while the southern portion is inundated. The southern breach serves as the end of the Yolo Bypass, a flood spillway that reduces pressure on mainline levees within the Delta during flood events. Additionally, the island drains and fills through multiple levee breaches on its eastern side (into Prospect Slough and Liberty Cut) and western side (into Shag and Cache Sloughs). Shag Slough flows into Cache Slough and its waters interact with Cache Slough through several inlets, including a small shallow unnamed flooded island (Figure 3-2). Cache Slough forms the main drainage from this region of the Delta, flowing into the Deep Water Shipping Channel (DWSC) and, ultimately, the Sacramento River. Notably, the main source of freshwater to the CSLI enters from down-estuary, as both the DWSC and the Sacramento River pass south and east of the CSLI. Taken together, these water bodies form the main pieces of the CSLI complex. For this study, we focused on Cache Slough (Figure 3-3), just down-estuary of the intersection with the smaller unnamed island.

Figure 3-2: Cache Slough/Liberty Island complex. The field campaigns focused on the region in the box. Note the outlet from the unnamed island into Cache Slough within the box.

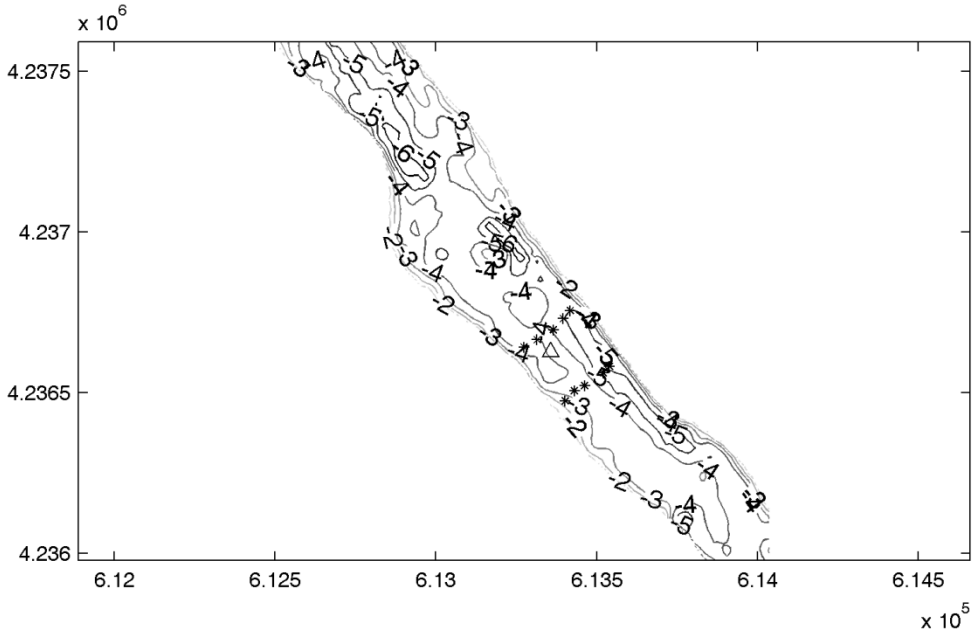

Figure 3-3: Cache Slough bathymetry. Labels are in meters. Axes are UTM coordinates in meters. Stars represent thermistor chain locations for the November field campaign. The triangle represents the ADCP location from November. The May experiment did not have the second (down-estuary) row of thermistor chains. Note that the bathymetry for the small unnamed flooded island was not available. During our time on the water, the unnamed island was very shallow, order 1 m or less, with boat often hitting bottom when in the island.

3.2 Methods

3.2.1 Field campaign

To study thermal dynamics, lateral momentum, and along-channel mixing, we conducted two observational studies measuring water temperatures and velocities within Cache Slough. To account for atmospheric influences including wind, we relied on data collected by outside agencies. We placed RBR Ltd. thermistors and a RBR Ltd. CTD (Conductivity, Temperature, and Depth) instruments within a cross section of Cache Slough, just down-estuary of its connection with the unnamed flooded island (Figure 3-3) for two weeks in October-November 2009 and for 4 weeks in April-May 2010. We will refer to these deployments as November and May, respectively. The November campaign had 17 thermistors and one CTD; the May campaign had 19 thermistors. In November, we placed an additional 11 thermistors in a second cross-section roughly 200 m down-estuary of the first cross section. The thermistors measured water temperature every 5 seconds for the duration of each campaign. We placed a Teledyne RD Instruments acoustic Doppler current profiler (ADCP) just down-estuary of the thermistor cross section during these time periods. The ADCP took measurements every 10 seconds for each 25 cm bin of the water column for the duration of the experiment. Meteorological data were from the nearby California Irrigation Management Information System (CIMIS) station (www.cimis.water.ca.gov) at their Hastings Tract East location, roughly 3 km from the study site. Since stress and heat flux equations generally rely on wind velocities at 10 m above the surface and the CIMIS station is 2 m above the bed, we extrapolated wind speeds to 10 m assuming a log layer and a roughness height, z_0, of 0.1 m. Initial processing of the data included turning the ADCP data along its principal horizontal components (along-channel and lateral directions). For analysis purposes, data was averaged to create 10 minute and 1 hour datasets. For this paper, positive x is defined as along Cache Slough and down-estuary; positive y is defined as perpendicular to x and across Cache Slough, roughly towards the northeast; positive z is defined as vertically upwards.

3.2.2 Data Analysis

3.2.2.1 Principal Component Analysis

The observed temperature data included variations in both the vertical and lateral dimensions at tidal, diurnal, and other timescales. This combination of spatial and temporal variability makes it difficult to isolate the effects of atmospheric forcing (including heating and wind) and tidal forcing (both advection and mixing). As a result, we used principal component analysis (PCA) to reduce the data to specific spatial structures that can be more easily connected to forcing mechanisms as well as effects. An overview of PCA can be found in Stacey et al. (2001); a more complete discussion is in Preisendorfer and Mobley (1988). This analysis involves taking the eigenvectors and eigenvalues of the covariance matrix of several concurrent datasets. In this case, each dataset was multiple observations of temperature over time. A principal component (PC) is an eigenvector and an associated time series which we will refer to as the amplitude of the principal component. The eigenvectors represent the way to rotate the original data (in temperature and time) such that the maximum amount of total variance is contained in each successive rotation. The rotated data is the amplitude of the principal component, and it represents how the PC plays out

over time. The eigenvector shows how the time series plays out over space. The eigenvalues inform how much total variation is contained in each PC. Each successive principal component then explains the maximum amount of variability that remains in the dataset after removing the contributions of the previous principal components. Since all the eigenvectors are mutually orthogonal to each other, there is no redundant information across principal components, i.e. each PC shows a signal that is unique amongst the others.

3.2.2.2 Multiple Linear Regression

To analyze the effect external (wind) and internal (baroclinicity) forcings are having on lateral momentum within the cross-section, we used multiple linear regression to calculate the predictive capabilities of the forcings on the observed lateral circulations. Since we begin with fundamental physical equations, the regression coefficients served as more than just fitting parameters; they offer insight into the validity of the model since we can compare calculated values to published values.

3.3 Results

3.3.1 Field Observations

3.3.3.1 Atmospheric Observations

During our November study, air temperatures generally ranged 20°C daily, with average mean temperatures trending downwards from roughly 12°C to 8°C (Figure 3-4). The wind was generally calm (<3 m/s), with a few larger events. The first wind storm was a large event from October 26-28, with the wind generally coming from the north at 8-9 m/s. The second major wind event was on November 4, when the wind blew almost directly laterally across the channel, from the southwest, as hard as 10 m/s. Neither of these events brought any rain. Two small rain events brought rain later in the experiment. The May experiment had smaller daily temperature ranges, but higher and more consistent daily maximum temperatures, generally near 28°C compared to November's 26°C. Daily average temperatures fluctuated strongly, from a high of near 19°C on May 3 down to 9°C on May 22. The wind was much more active, with wind speeds greater than 4 m/s an almost daily occurrence. There was more rain in May, but it was generally less than 2 mm/hr.

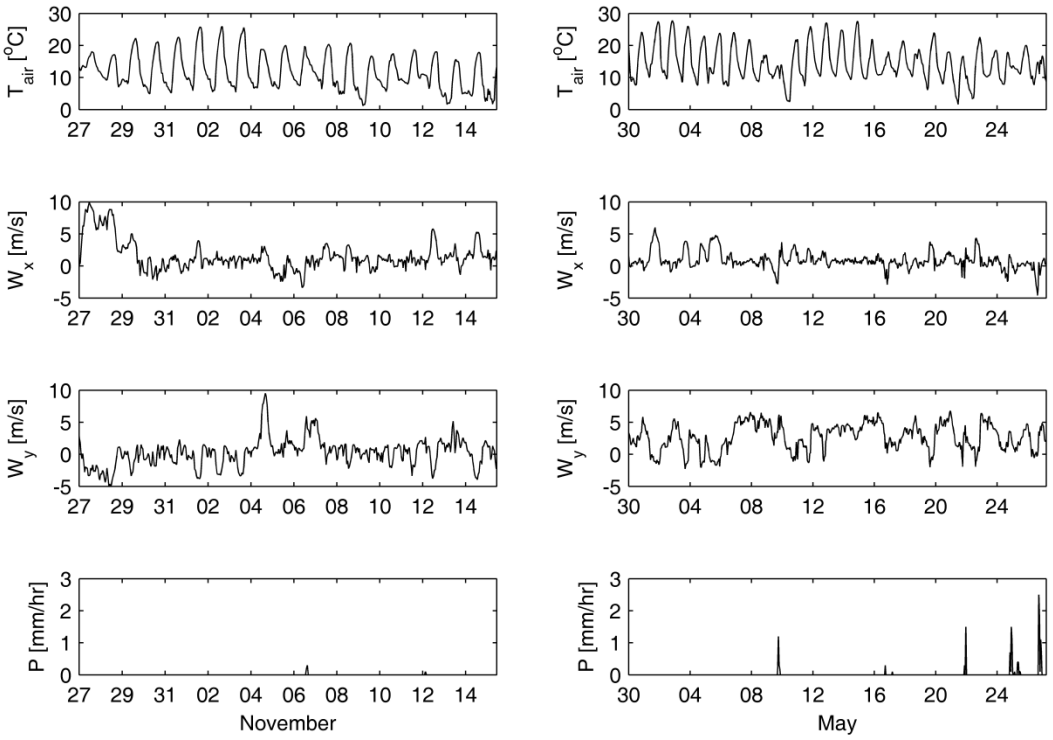

Figure 3-4. Atmospheric conditions at the nearby CIMIS weather station. The November campaign is on the left; the May campaign is on the right. The top panels have air temperature; the second and third panels have along-channel and lateral wind speeds; the bottom panels have precipitation.

3.3.1.2 General Water Column Observations

In Figure 3-5, we present some characteristic measurements from our field site. The tidal range at our site was roughly 1-1.5 m with along-channel velocities peaking near 0.15 m/s. Analysis of water depths and salinities from Figure 3-5 indicate that the CSLI behaved as a "reverse estuary", where water depths correlate negatively with salinity (r = -0.88 in November). In May, flood tides brought fresh water, but the net transport of fresh water from down-estuary freshened the CSLI. This trend in salinity in May eliminated the correlation between water depth and salinity (r = 0.01) despite the obvious decreases in salinity during flood tides. If we high-pass filter depth and salinity to remove cycles longer than 3 days, the relationship is more clear (r = -0.86, -0.70 for November and May, respectively). This would follow from fresh Sacramento River water entering the system from down-estuary, while water losses from evaporation continually increase the salinity of the up-estuary reaches. Regardless, the salinities in question were low, and the tidal range of salinity was low. From this point on, we will ignore salt-derived baroclinity in the system.

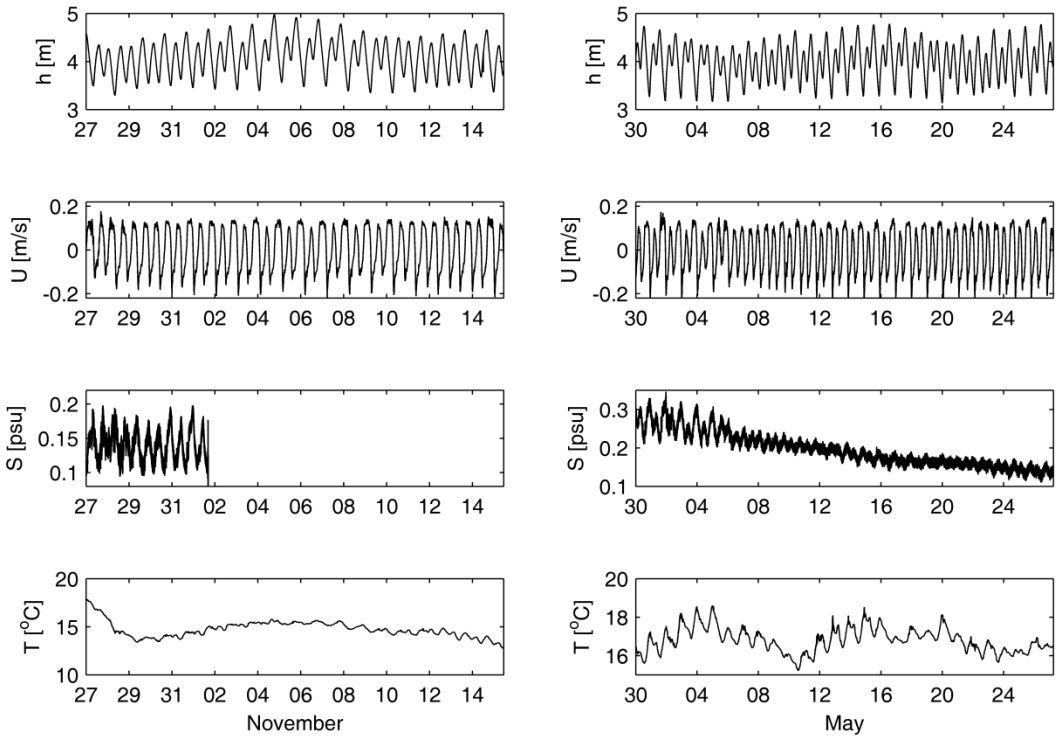

Figure 3-5. Depth, depth-averaged along-channel velocity, salinity, and cross-sectionally averaged temperature at field site for November and May field campaigns. November is on the left; May is on the right.

3.3.1.3 Water Temperature Observations

Water temperatures ranged less than a degree daily in November, with more variation on longer timescales (Figure 3-5). The water temperature dropped almost 5°C during the November campaign, mimicking the air temperature for the period (Figure 3-4). Similarly, longer timescale variation dominated in May with almost 4°C change from week to week, but the diurnal fluctuations were roughly 1.5°C. If we correlate high-pass filtered cross-sectionally averaged temperature with depth in the same manner as we did for salinity in section 3.3.1.2, we get correlation (r = -0.57, 0.44 for November and May, respectively) that is weaker than that for salinity. This indicates that temperature effects were less driven by along-channel advection than salinity, and that local heating/cooling or lateral advection matter for temperature on timescales shorter than several days. The change in sign of the correlation indicates that the along-channel temperature gradient switched signs seasonally, with cooler water coming from up-estuary in November and warmer water from up-estuary in May. This is consistent with the upper reaches of the estuary having been more sensitive to atmospheric heating/cooling than down-estuary, which was dominated by input of Sacramento River water.

Figure 3-6 shows the along-channel, lateral, and vertical gradients along the channel and within the cross section for each field campaign. In November, horizontal (x- or y-direction) temperature gradients were relatively small compared to vertical gradients, which were as large as 0.4 °C/m. Unsurprisingly, both lateral and vertical gradients were much larger in May, when vertical

gradients got as high as 0.7 °C/m. Gradients in all three directions varied on both diurnal and tidal time-scales as advection and atmospheric influences competed, but the vertical gradients were more strongly tied to daily heating and cooling. In addition to the importance these gradients potentially had on lateral momentum, they could have had an effect biologically. Within the cross section, total temperature differences as large as 1.6°C vertically were seen in November, while larger differences (2.8°C) were seen in May. Laterally, differences were found as large as 0.6°C in November and 1.2°C in May. Past work (Bennett 2005; Cloern et al. 2011; Wagner et al. 2011) has discussed the potential issues for the Delta smelt, for example, as temperatures approach critical levels. The fact that lateral temperature differences tended to increase during the warmer months means that cooler refugia may exist for these fish during seasons when their upper thermal limits might be approached in one location.

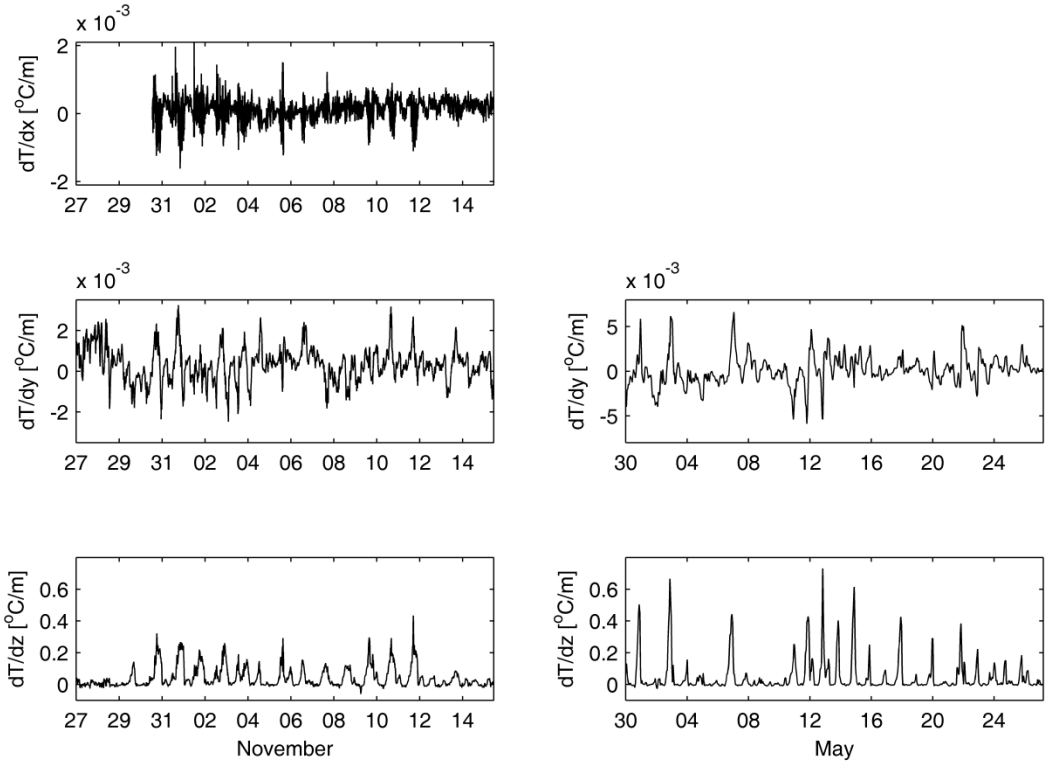

Figure 3-6. Mean thermal gradients in Cache Slough for the November (left) and May (right) field campaigns. Along-channel gradients were not measured in May.

3.3.1.4 Velocity Observations

Figure 3-5 shows the along-channel flows within the study site. A closer look at the timing of velocity and depth relationship shows a phase lag between stage and velocity of roughly 205 minutes in November and 210 in May. Depth-averaged tidal flows within Cache Slough were asymmetric, with stronger velocities on the flood (approaching -0.2 m/s) than on the ebb (roughly 0.15 m/s). If we phase-average the velocities, this pattern is apparent. To phase-average the velocities, we applied a time-stamp for each measurement for when it occurs in a tide, from 0 (when the depth-averaged velocity crosses zero and begins to ebb) to 1 (the end of the following flood).

Using this new time-stamp, we averaged depth-averaged velocity across all the tides to create one "typical" tide. Interestingly, peak flood velocities were typically short-lived, with flood velocities dropping after peaks (Figure 3-7). This had implications for creation of lateral thermal gradients (discussed below).

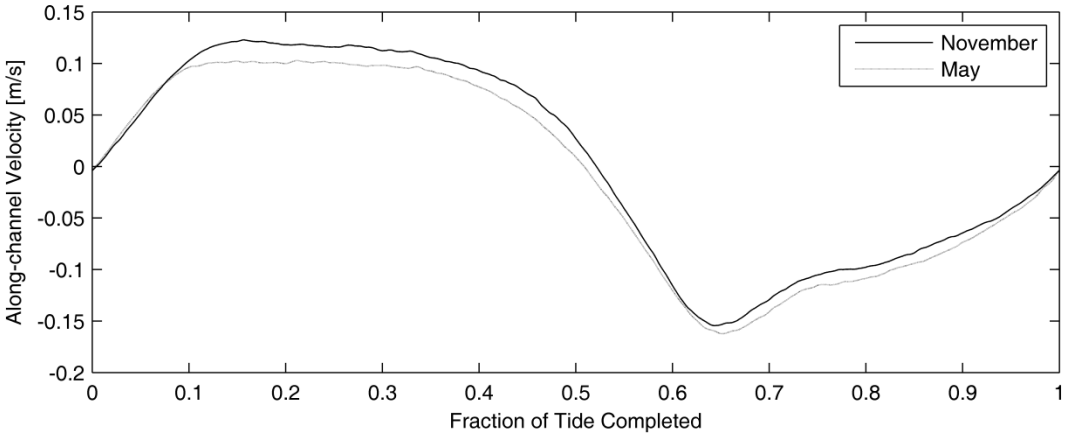

Figure 3-7. The along-channel phase-averaged velocity during November and May. The tides were asymmetric, with steady ebbs (positive) and shorter, peakier floods.

Depth-averaged lateral velocities were more than an order of magnitude smaller than the depth-averaged along-channel velocities, but lateral surface or bottom velocities could be of the same order or greater than along-channel velocities at certain times. Lateral velocities near the surface typically were order 0.01 m/s in magnitude, but during certain events, hourly velocities could average as high as 0.10 m/s (Figure 3-8). Along the bottom of the channel, velocities tended to be slightly weaker than the surface velocities, but in the opposite direction, indicating lateral circulation. While lateral velocities were generally small, they were often of the same order or greater than the along-channel velocities near the turn of the tide. Lateral circulations can be driven by any number of different processes, as mentioned earlier, including lateral baroclinic forcing , wind, curvature, and Coriolis forcing. During our November campaign, notable lateral circulation events occurred from 10/27-10/28, and on 11/4, 11/6, 11/12, and 11/14. We will discuss the forcing of these circulations below.

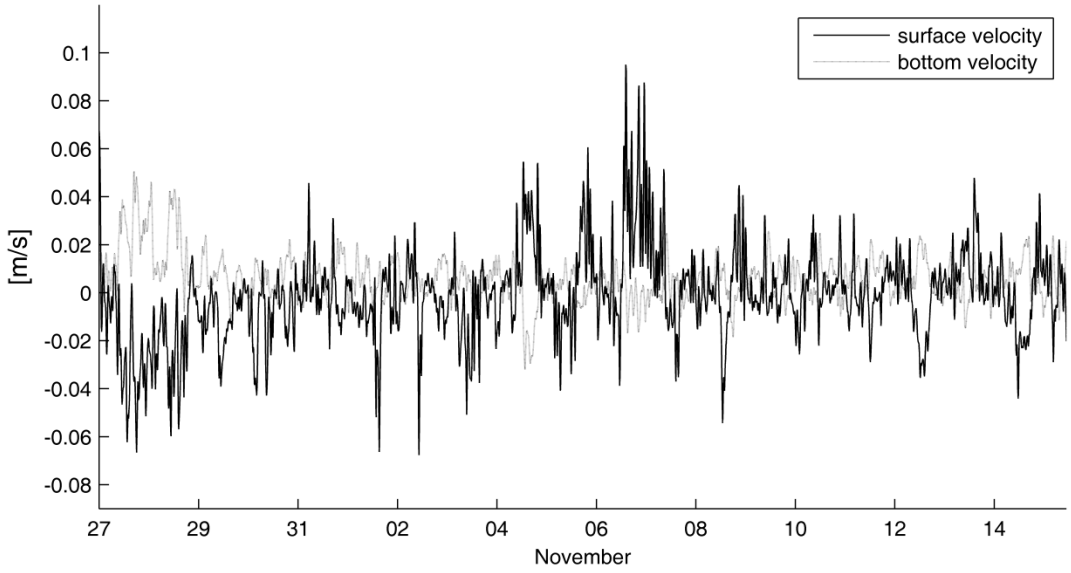

Figure 3-8. Lateral velocities at the surface and at the bottom during the November field campaign. These are 10 minute averages smoothed with an hourly window for clarity.

3.3.2 Principal Component Analysis

We used PCA on the thermistor dataset in November and May to tease apart the spatial and temporal dynamics within the temperature record. For the November field campaign, the amplitude of the first principal component (Figure 3-9) shows the general temperature trend, shared among all 18 sensors within the up-estuary cross-section, with a slightly stronger signal near the surface. This general trend, forced by the atmospheric conditions and along-channel advection (tides), represents the vast majority (96.0%) of the variance in the data. The amplitude of the second PC spikes daily; the eigenvector of the second PC (Figure 3-10) shows positive weighting near the surface and negative weighting near the bed. This PC represents thermal stratification, which occurred almost daily during this period. The stable stratification evident during the days was reversed at night with very weak unstable stratification. This PC contains 2.2% of the total variance in the data. The third PC shows lateral temperature differences (Figure 3-10) and contains 0.7% of the total variance. The time series shows this to predominantly a tidal process; analysis of the power spectral density (not shown) shows a sharp peak corresponding to a period of 12.2 hours. This is very close to the published M_2 tidal frequency of 12.4 hours. In May, PCA revealed qualitatively the same structures of the three eigenvectors (Fig 3-10).

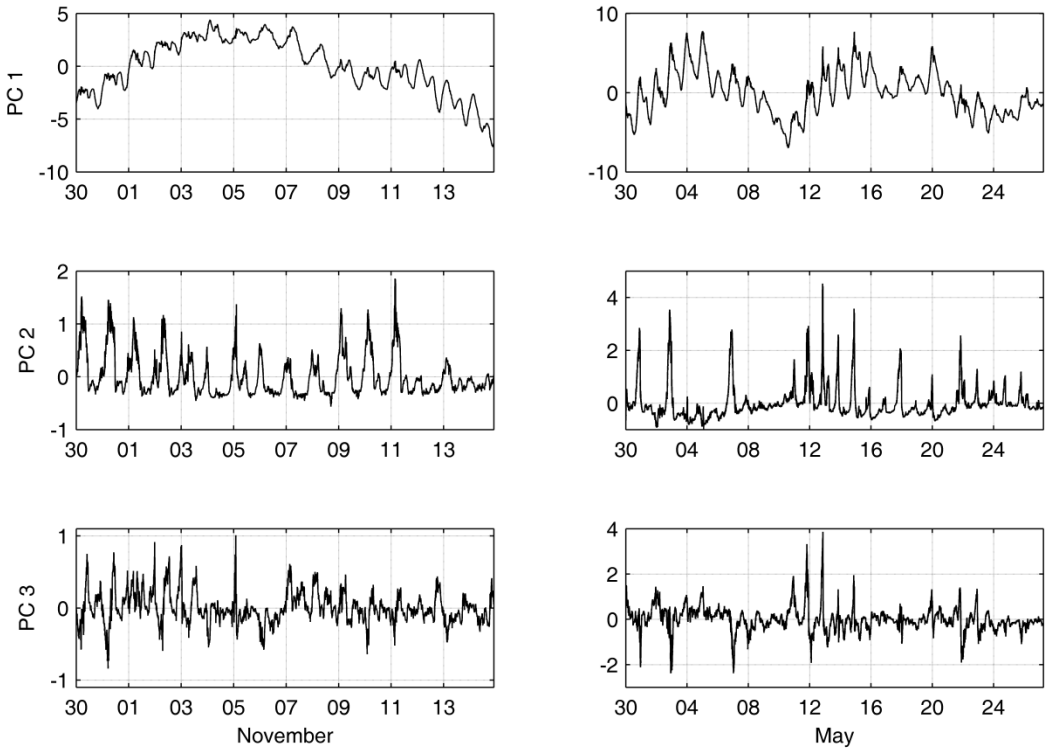

Figure 3-9. Amplitude of the first three principal components for the water temperature data in the up-estuary cross-section of Cache Slough.

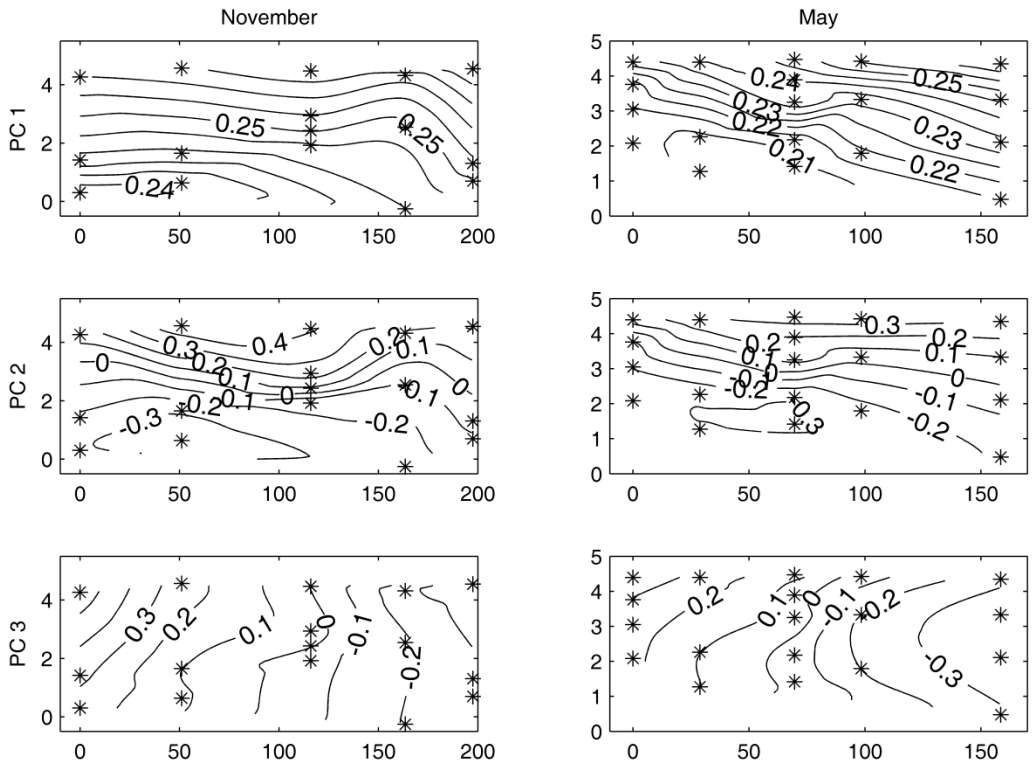

Figure 3-10. Eigenvectors of the first three prinipal components for the water temperature data in the up-estuary cross-section of Cache Slough. Stars indicate the locations of the thermistors.

Although PC3 holds so little of the original data's signal, we argue that it is real due to the robustness of this spatial structure in the May data. As an added test, we apply Overland and Preisendorfer's (1982) Rule N test to the data after we remove the first PC. For this test, we compare the amount of variance contained in each PC compared to the PCs of random datasets. PCs 1 and 2 (corresponding to PCs 2 and 3 in the original dataset) have more variance than 95% of PCs 1 and 2 of the random datasets and are considered real. We removed the first PC for this test because it contained so much variance as to dominate all other signals.

3.3.3 Multiple Linear Regression

In this section we consider the hypothesis that wind is an important component of the lateral momentum balance. The lateral circulation patterns evident in Figure 3-8 could have been caused by a number of different processes. Starting with fundamental physical equations, we will ultimately arrive at a regression equation in hopes of showing the relationship between the explanatory variable and lateral shear within the cross-section. We start with the lateral momentum equation:

$$\frac{\partial v}{\partial t} + u\frac{\partial v}{\partial x} + v\frac{\partial v}{\partial y} + w\frac{\partial v}{\partial z} - \frac{u^2}{r} = -\frac{1}{\rho}\frac{\partial P}{\partial y} + \frac{1}{\rho}\left(\frac{\partial \tau_{yx}}{\partial x} + \frac{\partial \tau_{yy}}{\partial y} + \frac{\partial \tau_{yz}}{\partial z}\right), \quad (3\text{-}1)$$

where u, v,and w represent velocity in the along-channel (x), lateral (y), and vertical (z) directions, t represents time, r represents the radius of curvature, ρ represents water density, P represents

pressure, and τ represents stress. The first term in equation (1) is the unsteadiness, terms 2 through 4 represent convective accelerations, term 5 is the curvature, term 6 is the pressure gradient due, in this case, to thermal gradients and lateral depth differences, and terms 7 through 9 are the viscous stress terms. We were not able to directly measure most of these terms, but we could scale them based on our measurements. Parameterizing the stress terms, we got

$$\frac{1}{\rho}\left(\frac{\partial \tau_{yx}}{\partial x}+\frac{\partial \tau_{yy}}{\partial y}+\frac{\partial \tau_{yz}}{\partial z}\right)= \nu_T\left(\frac{\partial^2 v}{\partial x^2}+\frac{\partial^2 v}{\partial y^2}+\frac{\partial^2 v}{\partial z^2}\right), \tag{3-2}$$

and further parameterizing the eddy viscosity, ν_T, following Fischer et al. (1979) as

$$\nu_T = \kappa u_* H, \tag{3-3}$$

where $\varkappa$ is the von Karman constant, u_* is the shear velocity, and H is the water depth, we were able to scale most of the terms in equation 1. Using typical values from our November observations, we were unable to scale the second or third term, since we do not have horizontal gratients of v, and we were not confident in scalings of the fourth term since measurements of w are near the instrument's lower limit. The remaining terms, however, scaled as: unsteadiness (10^{-7} m/s^2), pressure gradient (10^{-5} m/s^2), and lateral stress term (10^{-6} m/s^2). Note, for curvature (u^2/R) to have been an important factor, r, the radius of curvature, would have to have been as small as 10^3 m, too small for this relatively straight channel. The most likely balance in our system was between the lateral pressure gradient and the vertical stress term, both order 10^{-5} -10^{-6} m/s^2.

Using this knowledge, we developed a model of the difference in lateral velocities between the top and bottom layers of a two-layer system (Figure 3-11).

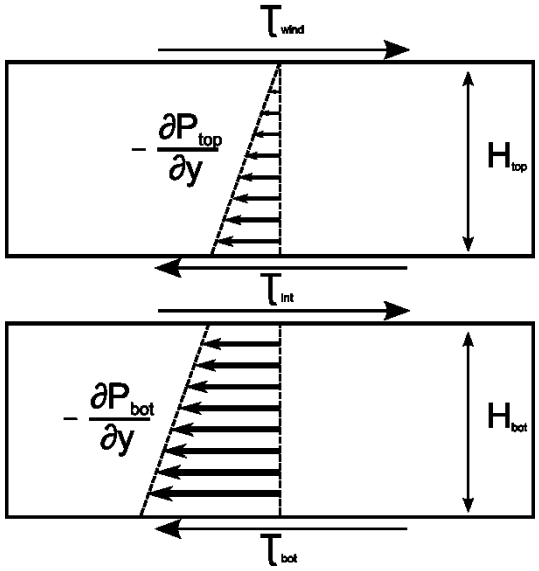

Figure 11. Schematic of two-layer system.

We began by layer-averaging equation (3-1), taking stresses and pressure gradients as the likely balance. The layer-averaged lateral momentum equation for the top layer of a two-layer system could then be written

$$\frac{\tau_{wind}-\tau_{int}}{H_{top}} = \frac{\partial P_{top}}{\partial y}. \quad (3\text{-}4)$$

The variable H_{top} represents layer depth. The subscripts *top* and *bot* (below) refer to layer-averaged quantities for the top layer and bottom layer, respectively. We define the interface between the two layers to be at half the depth. The subscript *wind* refers to wind stress; the subscript *int* refers to stress at the interface between the two layers. A similar equation could be written for the bottom layer as

$$\frac{\tau_{int}-\tau_{bot}}{H_{bot}} = \frac{\partial P_{bot}}{\partial y}, \quad (3\text{-}5)$$

Subtracting the bottom layer (equation 3-5) from the top (equation 3-4), we got:

$$\frac{\tau_{wind}-\tau_{int}}{H_{top}} - \frac{\tau_{int}-\tau_{bot}}{H_{bot}} = \frac{\partial P_{top}}{\partial y} - \frac{\partial P_{bot}}{\partial y}. \quad (3\text{-}6)$$

The barotropic contribution to both terms on the right hand side of equation (3-6) cancelled and the pressure gradients were evaluated as baroclinic-only gradients. In this case, we evaluated these gradients as due to thermal gradients only, since the system is very fresh (Figure 3-5). We chose a location, 80 m from the western-most thermistor mooring and roughly lined up with our ADCP, to calculate the temperature gradients for this pressure term.

Re-arranging equation (3-6), we got

$$\tau_{int} = \left(\frac{H_{top}H_{bot}}{H}\right)\left(-\frac{\partial P_{top}}{\partial y} + \frac{\partial P_{bot}}{\partial y} + \frac{\tau_{wind}}{H_{top}} + \frac{\tau_{bot}}{H_{bot}}\right), \quad (3\text{-}7)$$

where H represents total depth ($H_{top}+H_{bot}$). Parameterizing the interfacial stress term, we got:

$$\tau_{int} = \rho \nu_T \left.\frac{\partial v}{\partial z}\right|_{int}, \quad (3\text{-}8)$$

where the derivative represents the vertical gradient of v evaluated at the interface between the two layers. We further parameterized this expression as

$$\nu_T \left.\frac{\partial v}{\partial z}\right|_{int} = \alpha \nu_T \frac{\Delta v}{\Delta z}, \quad (3\text{-}9)$$

where a represents an unknown constant and Δ represents the difference between the top layer and the bottom layer. In this case, we use the average velocity in the top layer minus average velocity in the bottom layer to define Δv. Combining equations (3-7), (3-8), and (3-9), and re-arranging, we got

$$\Delta v = \frac{\Delta z}{\alpha \rho \nu_T}\left(\frac{H_{top}H_{bot}}{H}\right)\left(-\frac{\partial P_{top}}{\partial y} + \frac{\partial P_{bot}}{\partial y} + \frac{\tau_{wind}}{H_{top}} + \frac{\tau_{bot}}{H_{bot}}\right). \quad (3\text{-}10)$$

We parameterized the wind stress as

$$\tau_{wind} = \rho_{air} C_d{}^{air} \left|v_{wind} - v_{surf}\right|(v_{wind} - v_{surf}), \text{ where} \quad (3\text{-}11)$$

$C_d{}^{air}$ represents the coefficient of drag for the air on the water; ϱ_{air} represents the density of air; v_{wind} represents the velocity of the wind in the y-direction; and C_d represent the coefficient of drag

for the water over the bed. The subscript *surf* refers to the surface velocity. We expected C_d^{air} to have different value for the different directions of the wind, reflecting the variations in shielding, as the levee on the western bank of Cache Slough is much taller than the levee between Cache Slough and the unnamed island. We subdivided C_d^{air} into C_d^{air+} and C_d^{air-} for the different directions of the wind.

We parameterized the bottom stress as

$$\tau_{bot} = -\rho C_d V\sqrt{U^2 + V^2}, \text{ where} \quad (3\text{-}12)$$

C_d represents the coefficient of drag between the water and the bed and U and V represent depth-averaged u and v. Using these relationships (equations 3-11 and 3-12), equation (3-10) gives a forecast of the difference in the lateral velocity in each layer as a function of measured variables, constants, and ratios of length-scales. Combining equations (3-10), (3-11), and (3-12) as a regression equation, we got

$$\Delta v = \left(\frac{H_{top}H_{bot}}{H}\right)\left[A\left(-\frac{\partial P_{top}}{\partial y} + \frac{\partial P_{bot}}{\partial y}\right) + B\frac{\left(v_{wind}{}^{+} - v_{surf}\right)^2}{H_{top}} - C\frac{\left(v_{wind}{}^{-} - v_{surf}\right)^2}{H_{top}} - D\frac{\rho V\sqrt{U^2+V^2}}{H_{bot}}\right], \quad (3\text{-}13)$$

where

$$A = \frac{\Delta z}{\alpha\rho\nu_T}, \quad (3\text{-}14)$$

$$B = \frac{\Delta z}{\alpha\rho\nu_T}\rho_{air}C_d{}^{air+}, \quad (3\text{-}15)$$

$$C = \frac{\Delta z}{\alpha\rho\nu_T}\rho_{air}C_d{}^{air-}, \quad (3\text{-}16)$$

$$D = \frac{\Delta z}{\alpha\nu_T}C_d, \quad (3\text{-}17)$$

Using multiple linear regression to fit A, B, C, and D to the entire dataset, we calculated the quantities C_d^{air+}, C_d^{air-}, and C_d. Using water values derived from our November field campaign, and wind values from the nearby CIMIS station, we calculated $C_d^{air+} = 4.5 \times 10^{-4}$, $C_d^{air-} = 1.5 \times 10^{-3}$, and $C_d = 2.0 \times 10^{-3}$ with a correlation between measured shear and our modeled shear of $r = 0.66$ (Fig 3-12). These values are similar to published values of C_d^{air} (Mitsuta and Tsukamoto 1978; Stewart 1961), although these are usually measured over open water. We got similar results in May ($r = 0.62$), with $C_d^{air+} = 4.5 \times 10^{-3}$ and $C_d^{air-} = 3.2 \times 10^{-2}$., and $C_d = 9.8 \times 10^{-3}$.

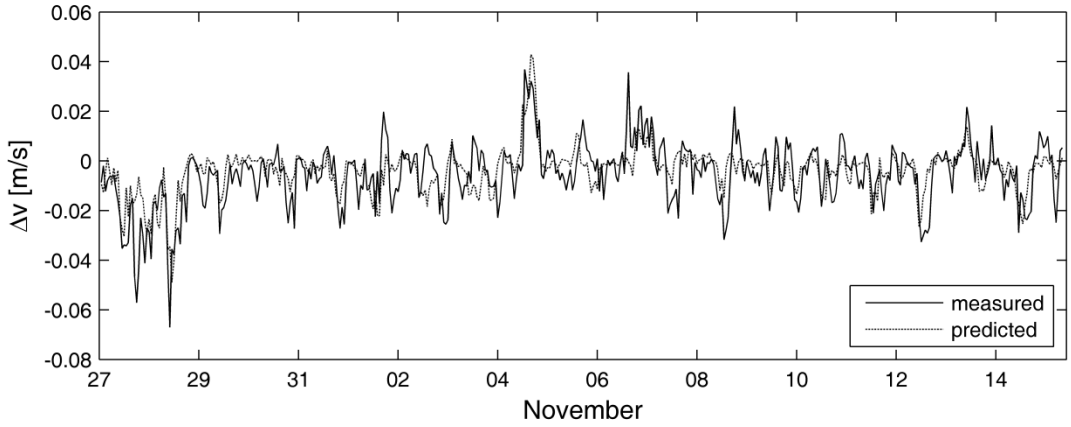

Figure 3-12. Modeled shear versus measured shear. The difference in the lateral velocities between the top layer and the bottom layer (Δv) as modeled in equation (3-13) and those measured in November (r = 0.66).

3.4 Discussion

The three processes (temperature, lateral momentum, and along-channel mixing) this study emphasizes have the potential to interact in many ways. Here we discuss the interactions between these foci, and how these three react to external forcings.

3.4.1 Temperature

PCA on the temperature data within the cross section revealed the same patterns in November and in May. The vast majority of the variance in the data was contained in the first PC, which reflects atmospheric influences and tidal advection, each on its respective timescale. The second and third PC represent vertical and lateral thermal gradients respectively. The second PC was created when heated surface water "cuts off" the bottom waters, through stable stratification. This caused the surface waters and bottom waters to respond differently to the diurnal heating/cooling, allowing for the variation captured in this PC to be distinct from variation captured in the first PC, which was also predominantly a response to atmospheric conditions. The third PC, which varies on tidal timescales, shows lateral differences in water temperature, likely due to differential heating (see discussion below). Shallower areas, whether they are flooded islands or sloughs or shoals, responded more strongly to atmospheric influences. Tidal action moved these waters into larger sloughs, but the waters did not instantly mix laterally, creating lateral gradients.

Interestingly, while the same pattern existed in November as in May, the percentages of variance explained by each PC differed between the months (Table 3-1). The November data showed much more variance in the first PC, with the second and third PCs showing much less variance than during the May campaign. This is due to the larger atmospheric fluxes to be found in May, which contribute to 1) stronger stratification events and 2) greater differential heating/cooling. In other words, the increased heating and cooling created vertical gradients that were strong enough to resist turbulent mixing and lateral gradients that were large enough to be more important in the larger scheme.

	November	May
PC1	96.0%	89.6%
PC2	2.2%	4.6%
PC3	0.7%	3.4%

Table 3-1. The percent variance explained by the first three principal components for the November and May field campaigns.

3.4.2 Lateral Momentum

Lateral momentum was only partially driven by advection of different thermal regimes causing lateral baroclinic gradients. The analysis in Section 3.3.3 shows the importance of the wind on the lateral momentum balance. This analysis only accounted for two potential forcings: thermal baroclinicity and wind. When the wind is low, this method did not completely predict the shear, as other unaccounted for processes become important (Figure 3-12). When the wind picked up, however, the wind dominated the system (Figure 3-13), creating shears large enough to over-turn the water column in time-scales of hours. This has important implications for lateral dispersion, and, potentially, for along-channel dispersion (see discussion below).

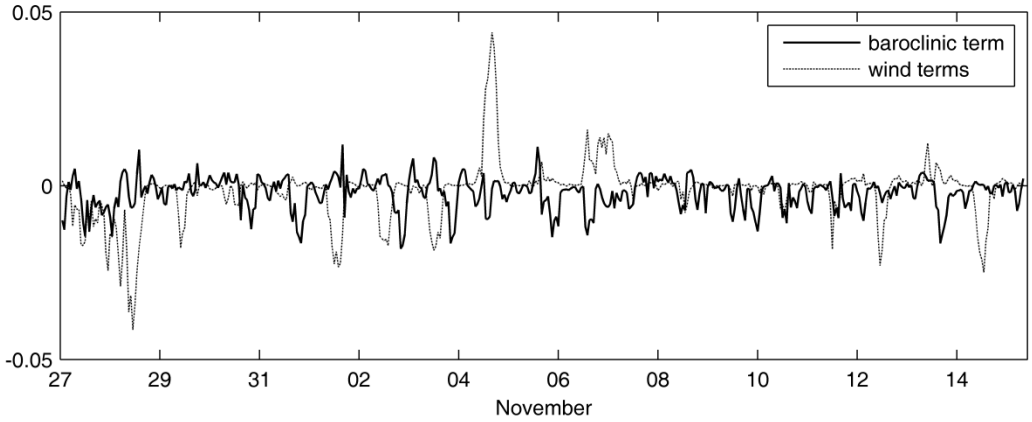

Figure 3-13. The relative importance of the contributions to the lateral shear equation over time. The thermal baroclinic term (first term on the right hand side of equation (3-13)) and the sum of the positive and negative wind terms are plotted.

The dominance of wind on this system was both surprising and important. While the other processes are also interesting, the dominance of the wind on such a small system and its effect on lateral momentum is important. Many past studies ignore the effects of lateral winds on an estuary, likely because short fetch-lengths lead one to the conclusion that wind shouldn't have a large effect. This study suggests that wind forcing can easily dominate the momentum balance, in the lateral direction, at least, in these small systems. Since lateral shear can lead to changes in along-channel dispersion if it effectively mixes out within cross-section shear (Fischer et al. 1979; Lerczak and Geyer 2004), this wind effect can become important on larger length-scales too.

3.4.3 Along-Channel Dynamics

The cross-sectionally averaged water temperature dynamics in an estuarine channel can be defined

$$\frac{\partial T}{\partial t} = -\langle U \rangle \frac{\partial T}{\partial x} + \frac{\sum F}{\varrho H C_p} + R \qquad (3\text{-}18)$$

where T is cross-sectionally averaged water temperature, $<U>$ is the cross-sectionally averaged velocity in the x-direction, F refers to atmospheric heat fluxes, ρ is the density of water, z is the depth of the water column, C_p is the specific heat of water, and R is the residual, representing lateral or vertical mixing and shear, unresolved processes in the cross-section that are frequently described by a diffusion term. The first term represents the unsteadiness of the water temperature at a point, the second represents the advective flux of temperature, and the third represents the change of temperature due to atmospheric heat fluxes. In this case, we used depth-averaged velocity, U, to represent the cross-sectionally averaged $<U>$.

Solving for the unsteadiness and the advective flux term using measured quantities revealed a balance between these two between the hours of 9pm and 12 pm (r =0.76). The fit deteriorated, likely due to atmospheric heating, from 1 pm to 11 pm (r = 0.40). Plotting the unsteadiness vs. the advective flux term revealed a relationship which leaves little room for other processes (Figure 3-14). Cross-channel averaged temperature changes were driven almost completely by advection of along-channel temperature gradients.

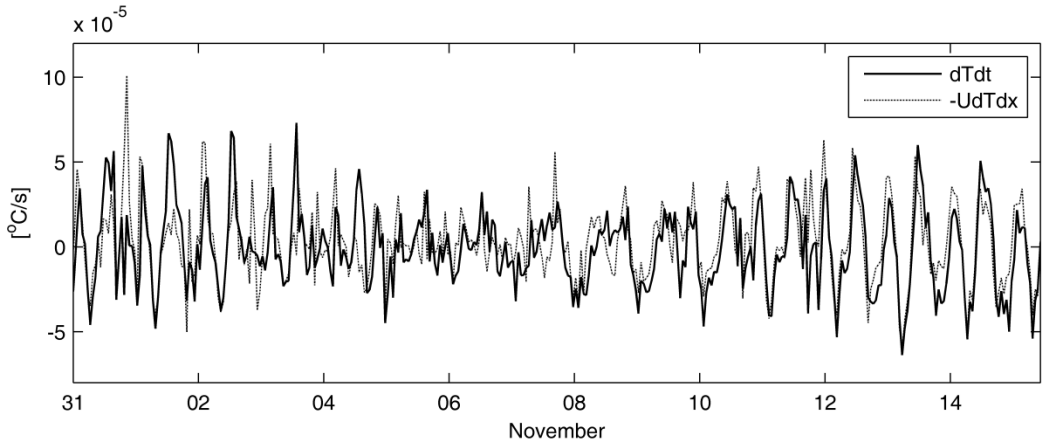

Figure 3-14. Unsteadiness vs. along-channel advection. Plotting unsteadiness and advection side-by-side shows the dominance of the advection term on the thermal dynamics of the system.

3.4.4 Connections between Temperature, Lateral Momentum, and Along-Channel Mixing

3.4.4.1 Along-Channel Dynamics create Lateral Thermal Gradients

Lateral thermal gradients form for a number of different reasons within the tidal and daily cycle. The largest gradients generally formed in mid- to late afternoon. In the fall, the largest positive gradients occurred on November 10 at 15:07 and on October 31 at 18:07. In May, the largest positive gradients occurred on May 3 at 16:32 and May 7 at 18:34. In both seasons, these largest gradients occured when the tide fell during late afternoon. Since advection of along-channel thermal gradients dominated cross-sectionally averaged temperature dynamics (Figure 3-14), we hypothesized that advection creates lateral gradients as well. Under this hypothesis, warmer waters from the small, shallow, unnamed island advected down-estuary following the right bank during falling tides, creating a positive lateral temperature gradient. In May, however, the maximum gradient occured later in the tide than in November, likely because heating continues later into the day, making it possible for lateral gradients to continue to intensify for the entire tide. Additionally, in May, strong cross-channel winds prevailed, likely preventing warm surface waters from spreading

across the channel, thus allowing larger lateral gradients to maintain and increase until the tide turned.

The largest negative lateral temperature gradients during the fall experiment occur on November 2 at 12:47 and November 5 at 14:57. The largest negative lateral temperature gradients in the May occurred on May 12 at 13:55 and on May 13 at 14:53. In November, strong rising tides combined with large positive along-channel temperature gradients lead to the assumption that the lateral gradients are formed by the interaction of lateral gradients of along-channel velocity and the along-channel temperature gradients. We did not measure along-channel temperature gradients for May. Notably, during both seasons, the maximum negative thermal gradients occurred immediately after the velocity magnitude on the rising tide had dropped from its peak (shown in Fig 3-10), leading credence to the idea that differential along-channel advection caused these gradients. When the velocities dropped after the peak, the intensification of the lateral gradients stopped, as differential advection lessened. The gradients formed by this process help create lateral shear.

3.4.4.2 Lateral Shear does not affect Along-Channel Dynamics

Lateral shear in this system was predominantly generated by cross-channel winds, but thermal baroclinicity was important when the wind is weak. The shears created, however, did not have a noticeable effect on the along-channel dynamics. We calculated the atmospheric flux term (following Wagner et al. 2011) from equation (3-18), and solved for the residual term, *R*, and it did not show an obvious pattern (Figure 3-15). We expected to find that wind, by creating lateral shear, would mix the cross section and affect along-channel dispersion by limiting across-channel shear or eliminating lateral thermal gradients.

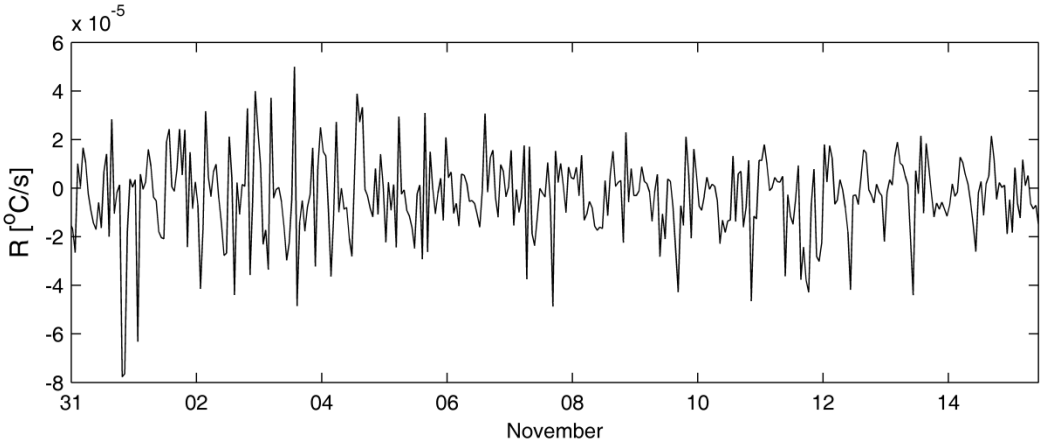

Figure 3-15. The residual term from equation (3-18).

The shears observed during our November experiment ($\perp v$ = 0.03 m/s) were seemingly enough to mix a 200 m wide channel laterally in timescales of hours, short enough to matter for along-channel mixing in a tidally oscillating system. Depending on the time-scale of the mixing processes relative to the oscillation timescale, increased across-channel mixing can either increase or decrease along-channel dispersion. For shear dispersion to work, however, differential advection of the scalar, due to either a non-uniform velocity field acting on a uniform along-channel scalar concentration or a uniform velocity field acting on a non-uniform scalar gradient or both, must interact with mixing processes across the channel. In this case, however, we postulate that the system likely maintained uniformity of velocity and temperature gradients on time-scales that were

comparable or smaller than the time-scales required for the shear to mix the cross-section. This would have negated any effect of lateral shear on along-channel dispersion of temperature. It would not necessarily have limited the dispersion of other scalars, however.

In order to quantify how the system maintained uniformity of temperature, consider the potential within cross-section balance between lateral advection of lateral temperature gradients and atmospheric heat fluxes:

$$v\frac{\partial T}{\partial y} \sim \frac{\sum \mathrm{H}}{\rho \mathrm{z} \mathrm{C_p}} \tag{3-19}$$

Using values of 10^{-2} m/s for v and 10^{-3} °C/m (Fig 5) for $\partial T/\partial y$, we get 10^{-5} °C/s for the lateral advection term, which is of the same order as the calculated heat flux term. This indicates that, within the cross-channel, a balance between wind-generated lateral advection of thermal gradients and atmospheric fluxes was possible, i.e. the along-channel thermal gradients could be maintained by atmospheric processes as quickly as they are formed by lateral advection. This action would have greatly reduced the effect of wind-generated shear on along-channel temperature gradients.

Similarly, along-channel momentum changes due to lateral shear would have to overcome the larger-scale balance between the unsteadiness and the barotropically-driven tide. For the lateral circulation to have affected the along-channel momentum, it needed to be larger than these terms. Comparing lateral advection of along-channel velocity to unsteadiness:

$$\frac{\partial U}{\partial t} \sim v\frac{\partial U}{\partial y}. \tag{3-20}$$

Tidal variation in U (Figure 3-4), however, was not the same as lateral variations in U. To address this, consider along-channel velocity as a first-order balance between a tidal barotropic pressure gradient and friction, i.e.

$$g\frac{\partial h}{\partial x} = C_d\frac{U^2}{H}, \tag{3-21}$$

where h is tidally-varying depth, then

$$U \sim \sqrt{\frac{1}{C_d} g \frac{\partial h}{\partial x} H}. \tag{3-22}$$

Since U scales as $H^{1/2}$, lateral variations in U scale as the square of the ratio of depths in the cross-section. Noting a depth range within the cross-section of 4-5 m (Figure 3-3), this relation shows the lateral variation of U to have been an order of magnitude smaller than tidal variation. Using the tidal timescale (T = 12.42 hours) and Δy = 200m, the left hand side of equation (3-18) is an order of magnitude larger than the right hand side. This indicates that the along-channel balance could re-equilibrate fast enough to limit the importance of the wind-driven lateral circulations.

These scalings indicate that the atmospheric fluxes and along-channel momentum balance were strong enough to erase the effects of the lateral circulations, even though these circulations could overturn the water column faster than tidal time-scales. This would explain the lack of effect shown on the along-channel advection-diffusion relation by lateral wind-driven circulations.

3.5 Summary

We have analyzed temperature and velocity data taken over two separate field campaigns within a cross section of a tidal slough in the Cache Slough/Liberty Island complex of California's Sacramento-San Joaquin Delta. The CSLI appears to have acted as a reverse estuary, as salinities increase with lower tidal depth. As the CSLI is upstream of any significant salinity, density gradients were predominantly driven by thermal differences. We found larger than expected thermal gradients, both laterally and vertically, that were created and broken down on a a variety of time-scales. Interactions between bathymetry, tides, and wind likely created and intensified these gradients, which mattered dynamically and biologically. We had hypothesized that 1) along-channel dynamics created lateral thermal gradients, which would then drove lateral circulation, and 2) lateral circulation affected along-channel dynamics by mixing out across-channel gradients of along-channel velocity and temperature. Our initial hypothesis was incomplete; however, as lateral winds proved to be the dominant forcing on lateral momentum in the cross-section during wind events, creating lateral circulation by driving return flows along the bottom of the channel due to set-up. Further, lateral circulations did not feedback into the along-channel dynamics, likely because they were not faster than the system's ability to re-equilibrate with tidal and atmospheric forcings.

Chapter 4

Exploration of Tidal Propagation in a Branching Channel Estuary

4.1 Introduction

There is increasing interest in restoring tidal marsh to achieve flood control and ecosystem services (Simenstad et al. 2006). When specific locations are altered, there is the potential to change the distribution of tidal energy. In branching tidal systems, tidal dissipation, propagation and reflection together define the spatial distribution of tidal energy. Restoration could lead to changes in any of these components, for instance by creating increased local dissipation. When specific locations or regions are altered, for example through the restoration of tidal marsh, there is uncertainty as to how the system will respond, including the spatial influence of the changes. When tidal marsh habitat is restored, it creates local tidal dissipation which may alter tidal energy in other parts of the estuary, potentially altering the function of tidal marshes elsewhere. It is important that this interaction be analyzed and understood before management decisions are made.

This study provides a first step towards understanding the interaction between tidal restoration and changes in tidal energy by modeling an idealized branching channel system. We present results of a simple analytic model of tidal propagation in a branching system. We develop wave equations for along-channel velocity and wave height which account for friction and changes in channel geometry. By linearizing the friction term in the depth-averaged along-channel momentum equation and including an amplification factor in the wave form, then combining it with the continuity equation, we solve for wave speed and amplification as a function of friction and channel geometry. We also solve for the tidal velocity and stage as a function of position and time. Using this solution within an idealized branching channel estuary and applying matching conditions at the branches, we analyze the effects of changes to one branch on tidal regimes throughout an idealized branching channel estuary. We then apply this simple model to consider restoration questions on California's Sacramento-San Joaquin Delta.

4.1.1 Importance of Tidal Regime to Ecosystem Function

In non-riverine dominated estuaries, local tidal dynamics set the local water depth and velocity, and provide a major contribution to the physical processes that control the transport of all ecologically important scalars (e.g. salinity, temperature, primary productivity, larvae, nutrients, etc.) Further, tidal dynamics affect sediment dynamics (Christiansen et al. 2000), which is crucial to long term sustainability of marsh elevations under potential sea level rise scenarios (Orr et al. 2003; Temmerman et al. 2004). Temmerman et al. (2003) modeled long-term marsh growth and noticed strong relationships between tidal inundation regimes, suspended sediments, and marsh growth.

Tidal amplitude is a major control on ecosystem function within tidal wetlands, affecting sediment dynamics, vegetation, bird useage, and nekton. Local tidal regime (tidal frequency, duration, and amplitude) combined with local marsh heights set inundation dynamics within a wetland system. By setting water depths, the tidal regime affects the suitability of wetlands to support vegetation and species that access the marsh ecosystem. Proper elevation in relation to tidal inundation is therefore a prerequisite for the successful restoration of salt-marsh vegetation. Past research (e.g. (Broome et al. 1988; Jacobs et al. 2009; Wolters et al. 2008)) found that the rate of salt-marsh development and species diversity appears to be affected mainly by water surface elevation. Further, Boorman et al (2001) stipulate that periods of non-inundation may be necessary for some

plants to form sufficient root structure. Burdick et. al (1997) noted that the proper hydrologic regime is essential to promote the rapid recovery of salt marsh functions in restoration. Blasco et al. (1996) noticed that mangroves are dependent on marsh inundation, among other factors, and will die out when inundation regimes become unsuitable.

Rozas (1995) found that inundation regimes affects nektonic use of wetlands as well as prey abundance and stem density. Changes to flooding frequency and duration can cause nekton community composition change and changes to access to the marsh surface; these actions can impair nursery habitat function (Osgood et al. 2003). Pomeroy (1959) noted that gross primary productivity of algae increases during high tides. Weisberg et al. (1981) found that when tidal heights were large enough to inundate the marsh surface, salt marsh killifish predate on marsh surface species. This is an important ecological link between the marsh and sub-tidal ecosystems. Zimmerman and Minnelo (1984) observed variation among crustacean species in response to spatio-temporal changes in water depth in a Texas salt marsh. Picman et al. (1993) noticed that increased water depths lead to decreases in predation of birds that breed in North American marshes.

4.1.2 Modeling Tidal Systems

In light of the importance of tidal regimes to ecosystem function, shifts in tidal regimes should be managed carefully. Physically-based models are needed to inform decision-makers of the repercussions of anthropogenic changes to an estuary and how they will affect tidal regimes. Although 3-D hydrodynamic models are more complete and able to handle the nuances of individual systems, they are computationally intense and site specific. The computational intensity limits the number of scenarios that can be run; this further limits the system responses that can be studied. Simple models offer the user the option to study multiple scenarios, varying multiple variables, to study relationships across multiple parameters. Further, since the domain is often simplified, the results can often be applied to other systems than the one being explicitly studied.

While tidal systems have been modeled extensively, most current tidal studies are field-based or numerical. Simple analytical model are not as common. Uncles and Stephens (1990) numerically modeled the Tamar Estuary, a branching estuary in southwest England, finding good agreement with observations. They were able to use this model to make inferences about the behavoir of this estuary to seasonal and spring-neap time-scale variation, but they did not use this model to study the interconnectivity of the branches. Banas and Hickey (2005) numerically modeled Willapa Bay, a branching estuary in Washington state, and noted the importance of branching to the circulation of the bay. They, too, did not study the interconnectivity of the branches. Sutherland et al. (2005) modeled tidal resonance in the Strait of Georgia and Juan de Fuca Strait, a complex branching system, using a simple analytical model with similar linear approximations as those made here. They were able to solve for the resonant periods of the system using these models.

Toffolon and Savinije (2011) applied an analytical model to explore tidal dynamics inside convergent estuaries. Using a simplified linear model that accounted for changes in an estuary's cross-sectional shape, they were able to re-create numerical results for the same idealized domain provided they applied their model over numerous smaller reaches.

In this study, we present an analytical model for tidal propagation similar to Toffolon and Savinije's, but we apply it to a branching channel estuary by applying matching conditions at junctions. We use this model to predict tidal regimes throughout the estuary, focusing on the up-

estuary ends of the system. This approach allows us to easily change the parameters of the system (geometry, friction, and reflection) to show relationships among them. Using this model, we explore tidal response to changes in reflectance at the head of the estuary and the relationship between this response an the parameters varied.

4.1.3 Study Domain

We will focus on tidal regimes in an idealized branching channel estuary (Figure 4-1), and California's branching Sacramento-San Joaquin Delta (Figure 4-2). The idealized system consists of a single main channel leading away from the source of tidal energy towards a fork. The fork (or junction) leads in two directions. These channels each lead to its head, where the tidal energy is either absorbed, reflected, or some combination of the two. Each of these three channels is defined by its geometry. The main channel is further defined by the forced tidal wave at its mouth. The two smaller channels are further defined by the ratio of reflected to absorbed energy at their heads; we will refer to this ratio as the channel's reflectance. This relatively simple domain will be useful to elucidate how changes to one branch of an estuary might affect other areas.

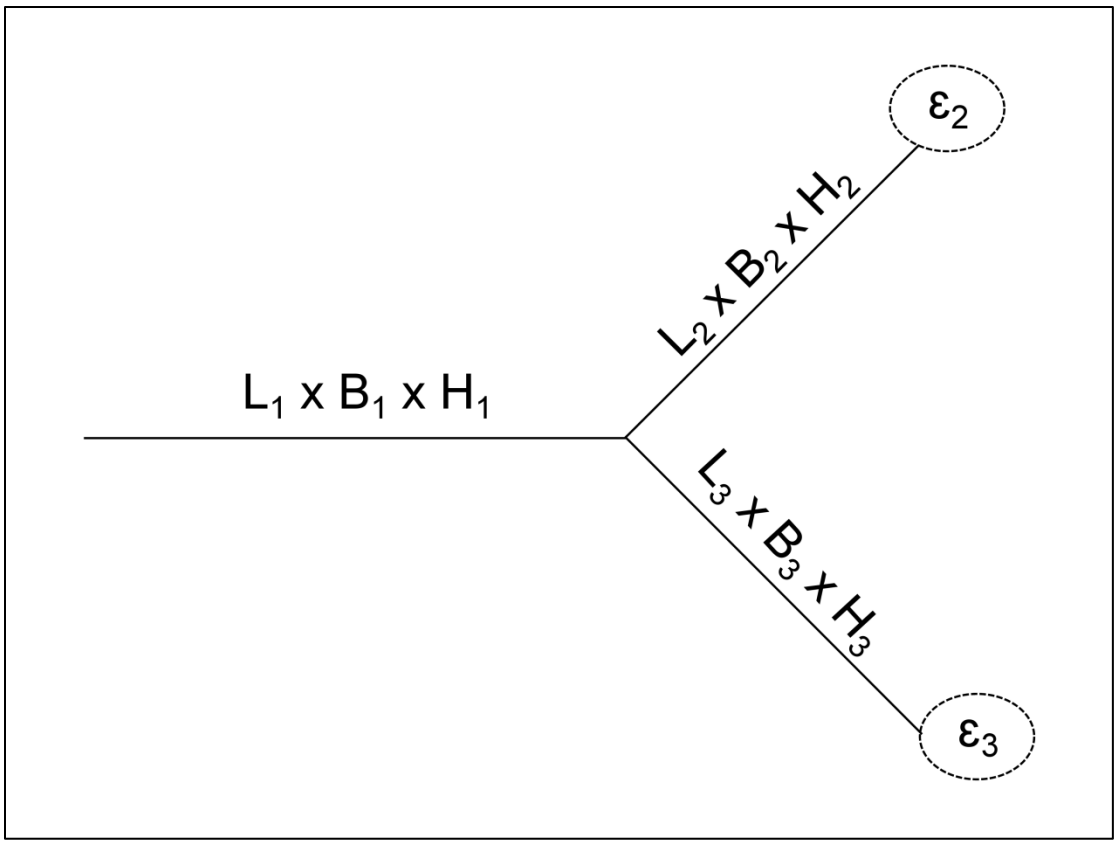

Figure 4-1: Schematic of simple branching channel system. Tides enter channel 1 from the left, from which they propagate into channels 2 and 3. At the heads of the channel, some portion of the tide is reflected, ε_j, where j is the channel number.

The Sacramento-San Joaquin Delta (hereafter, the Delta), on the other hand, is a much more complex system of interconnected rivers, tidal sloughs, and flooded islands (Figure 4-2). The Delta is, however, dominated by inputs from its two main sources of freshwater, the Sacramento and San Joaquin rivers, and by its connection to San Francisco Bay. While the Sacramento is a much larger river than the San Joaquin in terms of flow, their cross-sectional areas near their confluence are

comparable (despite different aspect ratios), suggesting that their tidal dynamics may be locally similar. Tidal energy dissipation, however, differs between the two rivers, both due the many smaller connecting slough and channels and variations in depth and friction along the channel. Further, reflection within the rivers differs due to differences in boundary conditions (levees, marshes, mudflats, etc.) Using our simple model, we will ignore the larger complexities of the Delta, and treat the system as if the Sacramento and San Joaquin rivers are the only feeders into the Delta, using characteristic geometry to define each (as well as the confluence). The tidal range near the confluence is roughly 1 m.

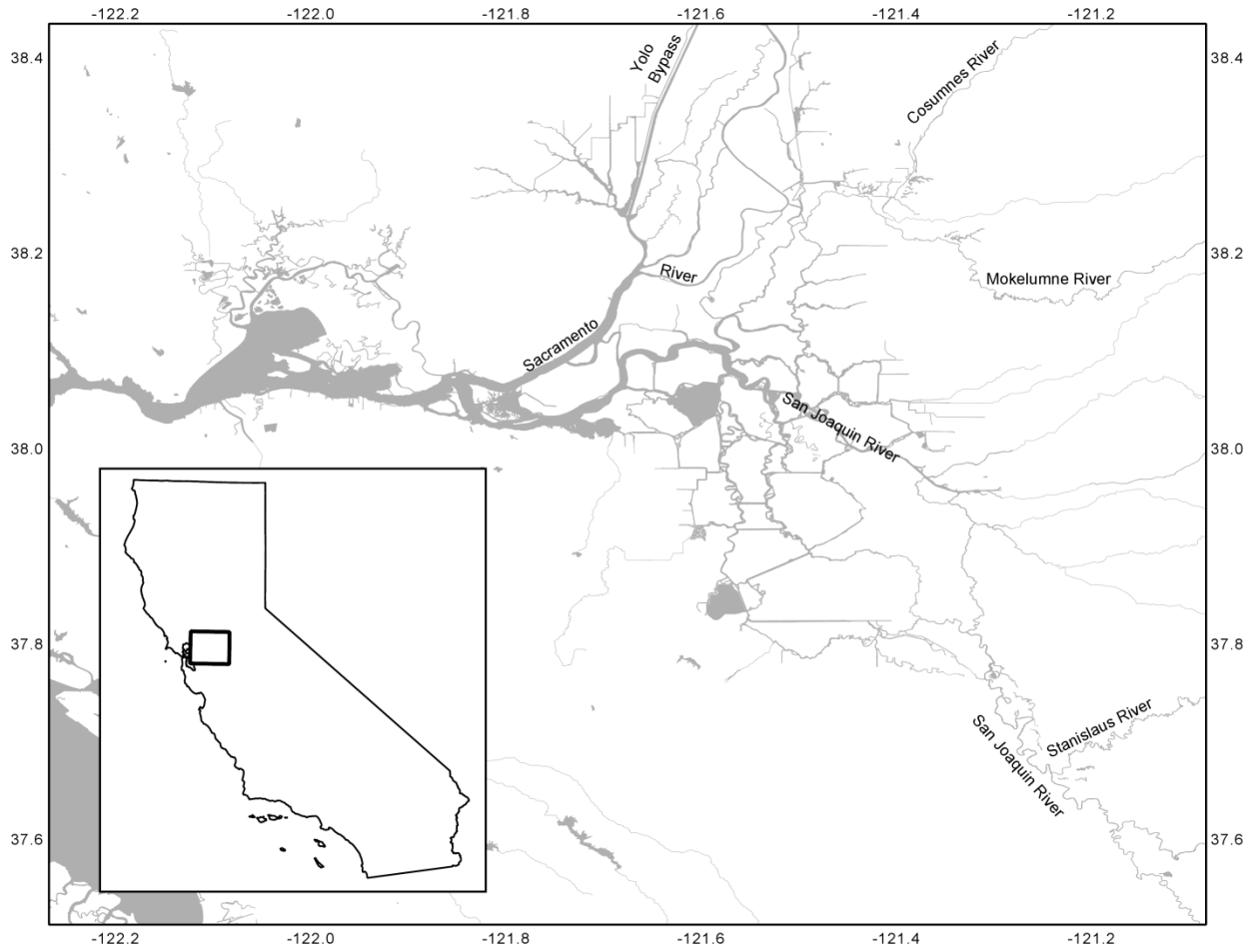

Figure 4-2: Sacramento-San Joaquin Delta. The Delta is forced primarily by freshwater flows from the Sacramento River from the north and San Joaquin River from the south as well as by tidal fluctuations from San Francisco Bay to the west.

The Delta, which was once a large wetland estuary, has been greatly altered by human activity and is now a system of rivers and sloughs, separated from the nearby islands by maintained levees (Brown 2003). In an effort to return ecosystem function to areas of the Delta, much discussion and work has been done re-create wetlands where possible and restore tidal action to flooded islands. These actions will affect the reflectance of energy within the Delta system.

4.2 Methods

Using linearized wave equations and matching conditions at the junction, we will characterize the effects changes in reflectance on one branch might have on the other branch.

4.2.1 Development of wave equations

The wave form has two principal unknowns, the wave height, $\eta(x,t)$, and the depth-averaged water velocity, $u(x,t)$, which define the wave form itself. If we focus on a single tidal harmonic (i.e. non-linear interactions between harmonics will not be covered), we define u and η as damped oscillations similar to Resnick et al (1992) (110) [110] [110] [110] [110] [110] [110] [110] [110] [110] [110] [110] [110] (110) (110) as

$$\eta(x,t) = Re\{\eta_0 e^{(m+ik)x} e^{-i\omega t}\} \tag{4-1}$$

$$u(x,t) = Re\{u_0 e^{i\varphi} e^{(m+ik)x} e^{-i\omega t}\} \tag{4-2}$$

The variables x and t represent the along-channel direction and time, respectively; the subscript 0 refers to some initial value of the variable. To define a wave form as it travels in a channel, we need to solve for the wave speed, c, the amplification of the wave as it moves down the channel, m, and the phase lag between u and h, φ. The wave speed is defined

$$c = \frac{\omega}{k}, \tag{4-3}$$

where ω represents the wave's angular velocity and k represents the wave number.

The 1-D depth-averaged momentum and continuity equations for tidal flow in a channel can be written

$$u_t = -g\eta_x - \frac{\tau}{\rho h} \tag{4-4}$$

$$B\eta_t + (Bhu)_x = 0 \tag{4-5}$$

where g is gravitational acceleration, $\boldsymbol{\tau}$ is the stress due to bottom shear, h is water depth, ρ is water density, B is the mean channel width at a location x, and subscripts represent derivatives in that dimension. The first term in equation (4-4) represents the unsteadiness of the velocity; the second represents the barotropic forcing due to the free surface tilt generated by the tide; the third represents the stress generated from the bottom. We assume convective acceleration terms, along-channel baroclinic pressure gradients, and wind forcing are negligible. The first term of equation (4-5) represents the time change in free surface height due to the tide; the second term represents the difference in flow along the channel. We assume that the flooded area does not change much as depth increases.

Taking advantage of the commonly made simplification

$$\frac{\tau}{\rho} = C_D|u|u \tag{4-6}$$

where C_D is a coefficient of drag, we can re-write equation (4-3) as

$$u_t = -g\eta_x - \frac{C_D|u|u}{h}. \tag{4-7}$$

Water depth, h, is split into its mean water depth at that location and a fluctuating portion (the wave height), i.e.

$$h(x,t) = H(x) + \eta(x,t), \tag{4-8}$$

where H represents the mean water depth at a location in the estuary and η represents the tidal fluctuations from H, as shown in Figure 4-3.

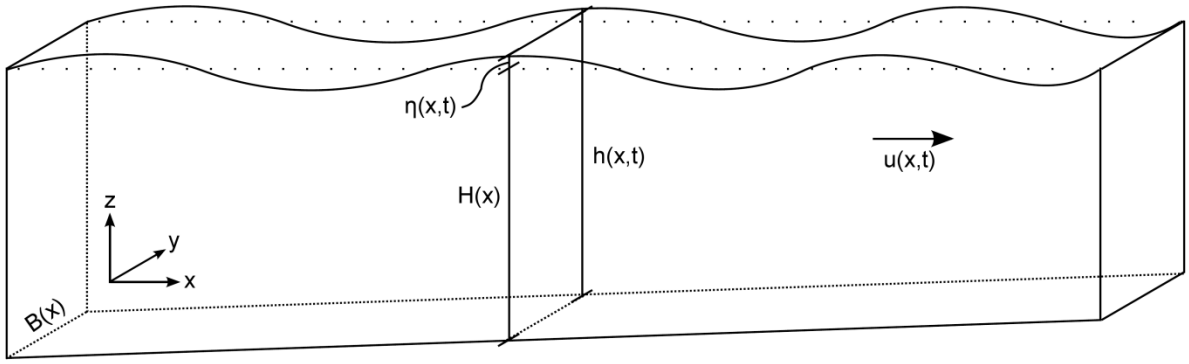

Figure 4-3. The wave form. The water's depth, *h(x,t)*, can be split into a the temporally-averaged depth, *H(x)*, and a time-varying fluctuation, *η(x,t)*. The width can vary with *x*.

To linearize our equations, we will drop all non-linear terms. For water depth, this means we will assume wave heights are small relative to channel depths:

$$h \approx H. \tag{4-9}$$

Following Toffolon and Savinije (2011) and Lorentz (1926), we can linearize the stress term and further re-write equation (4-7) as

$$u_t = -g\eta_x - \frac{Fu}{H} \tag{4-10}$$

where F is a velocity scale that represents the shear stress. For this work, we will assume that F is constant throughout a channel reach. Taking the time derivative of the linearized momentum equation (4-10) and the x-derivative of the continuity equation (4-5), dropping non-linear terms, and combining, we get

$$Bu_{tt} = gB_x\eta_t + g(BHu)_{xx} - \frac{BF}{H}u_t \tag{4-11}$$

which leaves us a single wave equation with both u and η unknown. Re-arranging equation (4-5), we can say

$$\eta_t = -\frac{1}{B}(BHu)_x \tag{4-12}$$

Plugging equation (4-12) into (4-11) and simplifying, we get a single equation with one unknown, u:

$$HBu_{tt} + BFu_t + \left[gH\frac{B_x}{B}(BH)_x - gH(BH)_{xx}\right]u + \left[gH\frac{B_x}{B}(BH) - 2gH(BH)_x\right]u_x - gBH^2u_{xx} = 0. \quad (4\text{-}13)$$

Plugging the assumed form of *u* from equation (4-2) into (4-13) and simplifying, we get:

$$-HB\omega^2 - iBF\omega + gH\frac{B_x}{B}(BH)_x - gH(BH)_{xx} + \left[gH\frac{B_x}{B}(BH) - 2gH(BH)_x\right](m + ik) - gBH^2(m + ik)^2 = 0 \quad (4\text{-}14)$$

Taking the imaginary part of equation (4-14), we can solve for the amplification as

$$m = -\frac{F\omega}{2gH^2k} - \frac{B_x}{2B} - \frac{H_x}{H} \quad (4\text{-}15)$$

Combining (4-15) with the real part of equation (4-14), we can solve for the dispersion relation:

$$\omega^2 = \frac{\frac{5gH^2{B_x}^2}{4\ B} + gB{H_x}^2 - gH^2B_{xx} - gBHH_{xx} + gBH^2k^2}{\frac{BF^2}{4gH^2k^2} + BH} \quad (4\text{-}16)$$

This equation can be simplified for any number of specific conditions. Considering piecewise prismatic channels, *H* and *B* would be constant along the length of the channel. From (4-15), we get the amplification

$$m = -\frac{\delta{k_0}^2}{2k}, \quad (4\text{-}17)$$

where

$$k_0 = \frac{\omega}{\sqrt{gH}} \quad (4\text{-}18)$$

and

$$\delta = \frac{F}{H\omega}. \quad (4\text{-}19)$$

The real part of equation (4-14), under the prismatic assumption, can then be written

$${k}^2 = {k_0}^2 + m^2. \quad (4\text{-}20)$$

Combining (4-17) and (4-20), we can write equations for *m* and *k* in a prismatic channel that show their dependence on k_0 and the dimensionless number δ.

$$m = -k_0\sqrt{\frac{1}{2}(\sqrt{1+\delta^2} - 1)} \quad (4\text{-}21)$$

$$k = k_0\sqrt{\frac{1}{2}(\sqrt{1+\delta^2} + 1)}. \quad (4\text{-}22)$$

Plugging (4-1) and (4-2) into the continuity equation (4-5), applying prismatic condition, linearizing and rearranging, we get

$$u = \frac{\eta\omega}{H}\left(\frac{k+im}{m^2+k^2}\right) \tag{4-23}$$

which can be further simplified to give

$$u_0 e^{i\varphi} = \frac{\eta_0\omega}{H}\left(\frac{k+im}{m^2+k^2}\right) \tag{4-24}$$

from which we can solve and get

$$u_0 = \frac{\eta_o\omega}{H(m^2+k^2)^{1/2}} \tag{4-25}$$

$$\varphi = tan^{-1}\left(\frac{m}{k}\right). \tag{4-26}$$

We could have used the momentum equation (4-4) along with (4-1) and (4-2) to get different expressions for u_0 and φ, however, these expressions would have been mathematically identical to (4-25) and (4-26), assuming (4-21) and (4-22) are true. From (4-21), (4-22), and (4-26), the phase lag, φ, can be shown to have a limit of -π/4, as friction becomes infinite.

For linear waves in a prismatic channel, the equations (4-1) and (4-2), with (4-21), (4-22), (4-25), and (4-26) define the waveform. Further, we can define the volumetric flux through a cross section, Q, of a channel due to a small-amplitude wave as

$$Q = HBu \tag{4-27}$$

which can be re-written in terms of η using equation (4-23) to give

$$Q = B\omega\left(\frac{k+im}{k^2+m^2}\right)\eta \tag{4-28}$$

4.2.2 Development of branching channel equations

We define an idealized branching channel system as shown in Figure 4-1, with the geometry in channel j defined as length (L_j), width (B_j), and depth (H_j). Within each channel, we define a forward wave (f_j) and a backward wave (b_j) in terms of wave heights. Within the 3 channel system outlined in Figure 4-1, this gives 6 unknowns, three forward waves and three backwards waves, which meet at the junction. We will solve for all six at the junction. We define the incident wave for the system, f_1, as

$$f_1(x,t) = \eta_{f1} e^{(m_1+ik_1)x_1} e^{-i\omega t}, \tag{4-29}$$

where η_{f1} refers the wave amplitude at the beginning of channel 1 and x_1 refers to the distance along channel 1. At the junction, f_1 is defined as

$$f_1(L_1,t) = \eta_{f1} e^{(m_1+ik_1)L_1} e^{-i\omega t} \tag{4-30}$$

At the junction of channels, we impose two matching conditions, following Lighthill (1978): continuity of the free surface and conservation of mass. For continuity of the free surface, we require

$$f_1(L_1,t) + b_1(L_1,t) = f_2(0,t) + b_2(0,t) = f_3(0,t) + b_3(0,t). \tag{4-31}$$

For conservation of mass, we require flow into the junction to equal the flow out of the junction. Using equation (4-28), we write

$$B_1\left(\frac{k_1+im_1}{{k_1}^2+{m_1}^2}\right)\left(f_1(L_1,t)-b_1(L_1,t)\right)+B_2\left(\frac{k_2+im_2}{{k_2}^2+{m_2}^2}\right)\left(-f_2(0,t)+b_2(0,t)\right)+$$
$$B_3\left(\frac{k_3+im_3}{{k_3}^2+{m_3}^2}\right)\left(-f_3(0,t)+b_3(0,t)\right)=0 \quad (4\text{-}32)$$

Notably, equations (4-31) and (4-32) create possibilities for reflection, positive or negative, at the junction due to cross-sectional shapes.

At the end of each channel, we impose a reflection condition, wherein some fraction, between 0 and 1, of the incoming wave, ε_j, is reflected, in phase, back towards the junction. We impose no reflection from the mouth of the estuary, where f_1 enters, but we allow reflection at the head of channels 2 and 3. Applying this condition to each channel and considering it propagates to the junction, for channels 2 and 3, we impose

$$b_j(0,t)=\varepsilon_j e^{(m_j+ik_j)2L_j} * f_j(0,t) \quad (4\text{-}33)$$

Through these six equations (4-30)-(4-33), we are able to solve for the wave heights for all six waves at the junction. (Note: Equation (4-31) and equation (4-33) are each two equations.) Using equation (4-1), we can then solve for wave heights at any location in our idealized branching channel estuary by propagating the forward wave and the backward wave from the junction to the location of interest. Superposing these wave forms, we get the local tidal wave form:

$$A_j(x_j,t)=\ f_j(x_j,t)+b_j(x_j,t) \quad (4\text{-}34)$$

The local tidal wave form at the head of channel 3, for example, is defined as

$$A_3(L_3,t)=f_3(L_3,t)+b_3(L_3,t) \quad (4\text{-}35)$$

We define a_{L3}, the tidal amplitude at $x = L_3$, as the amplitude of A_3, the combined wave at the head of channel 3.

4.2.3 Development of framework for exploration

We wish to use the equations developed in sections 4.2.1 and 4.2.2 to address questions regarding the interconnectivity of a branching channel estuary. To do this, we need to simplify the number of variables at play. We will present results of two different sorts: broad results aimed at a theoretical understanding of the interplay between two branches and a more controlled study that mimics the Sacramento-San Joaquin Delta (the Delta).

To eliminate the effects of amplification in channel 1, we will set L_1=0. To simplify the problem, we want to either set friction to zero or some value large enough to affect the system. In the inviscid case, F=0; we resort to scaling to discover an appropriate value in the other case.

Consider equation (4-11), a wave equation that includes a friction term. For the friction term to influence but not dominate the system, the third and fourth terms on the right-hand side of the equation should be of the same order, i.e.

$$gH^2 u_{xx} \sim F u_t \tag{4-36}$$

which implies that

$$\frac{gH^2}{\lambda^2} \sim \frac{F}{T} \tag{4-37}$$

where λ is the wavelength of the tide and T is the tidal period.

$$\lambda = cT, \tag{4-38}$$

The wave speed, c, is defined in equation (4-3), but can be approximated as

$$c = \frac{\omega}{k} \approx \frac{\omega}{k_0} \tag{4-39}$$

The assumption that k scales as k_0 will need to be checked since friction creates the difference between the two. Combining equation (4-16) under the prismatic inviscid assumption, (4-37), (4-38), and (4-39) gives

$$F \sim \frac{H}{T}. \tag{4-40}$$

At this level of friction, using k_0 in place of k creates a less than 2% error according to equations (4-20) and (4-22), well within reason and validating the earlier assumption. We will use equation (4-40) whenever we turn friction "on" for the studies below, creating a frictional environment, but not one that is dominated by friction. We will now explore the relationships between channel geometry, reflectances at the heads of channels, and friction on wave heights at the heads of the estuary.

4.3 Broad Theoretical Study: Results and Discussion

4.3.1 Broad theoretical results

We will explore the question of interconnectivity of two branching channels by starting simple, to establish base cases, then slowly adding complexity. The purpose of this section will be to explore how changes in branch geometry, reflectance, and friction will affect tidal amplitudes in the other branch. In the following analysis, we will walk through model results of progressively more complex situations to illustrate the model's behavior in response to changes to the idealized branching channel system. We do this to inform a case study on the Sacramento-San Joaquin (section 4.3.2). In that case study, we consider a tide meeting the confluence of the two major rivers with similar cross-sectional areas, but different aspect ratios. The tide will interact with different reflectances between the two channels; furthermore, the tides will extend different lengths up each channel.

We will consider first an even split, inviscid case with no reflection at the head of either branch. In this scenario, the channels 2 and 3 have identical cross sections with channel 1 having the same depth, but twice the width of either channel 2 or 3. We will then alter the reflectance at the head of channel 3 to complete reflectance and analyze the results. We will then add in friction to see how it affects the system. Finally, we will change the depth and width of channel 3 in an inviscid

scenario to determine the effect of each on tidal propagation. A summary of the different cases is offered in Table 4-1.

We will maintain $L_1 = 0$ throughout this study to focus on the interconnection between the branches. Changes to L_1 will only affect the phasing and amplitude (if the channel is frictional) of the tide at the junction. We will treat the incoming wave at the junction as a given. We will set $\eta_{f1} =$ 1 m in all cases. We will only consider the M_2 tide ($T = 12.42$ hours). All cases are summarized in Tables 4-1 and 4-2.

Table 4-1: The set-up and geometry for all cases within the theoretical study. All channel geometries are in meters.

		3.1a	3.1b	3.1c	3.1d	3.1e
	L_1	0	0	0	0	0
	B_1	200	200	200	200	200
Channel 1	H_1	10	10	10	10	10
	L_2	varies	varies	varies	varies	varies
	B_2	100	100	100	100	100
Channel 2	H_2	10	10	10	10	10
	L_3	varies	varies	varies	varies	varies
	B_3	100	100	100	100	50 or 200
Channel 3	H_3	10	10	10	5 or 20	10
	Friction	Off	Off	On	Off	Off
	ε_2	0	0	0	0	0
	ε_3	0	1	1	1	1

4.3.1.1 Even Split Case Setup and Results: Case 3.1a: Consider the case where channel 1 has a cross section (B_1 x H_1) of 200 m x 10 m that splits into two identical channels the same depth, but half the width (100 m x 10 m). Due to symmetry, we expect the tidal amplitude to be identical between the two branches. If we consider an inviscid, no reflection sub-case by setting friction to zero and the reflectances at the heads of channels 2 and 3 to zero, the incident wave will transmit with no reflection at the junction or loss of height into channels 2 and 3. The wave travels and encounters the head of each channel, where it is completely absorbed. (Setting reflectance to zero can be equivalent to having an infinitely long channel or a channel long enough that friction does not allow any return wave.) In this case, the tidal amplitude at the head of each channel (a_{L2}, a_{L3}) is 1 m, regardless of the length of the channels. The tidal phase would change as the wave moved upstream, but we will focus on tidal amplitudes only. There is no backward wave in channels 2 or 3; and none in channel 1, since the incident wave did not reflect at the junction and there was not a backward wave in 2 or 3. In this case, the tidal amplitude is 1 m everywhere in the system.

Case 3.1b: To simulate changes in channel boundaries, through either levee construction (increasing reflectance) or marsh restoration (decreasing reflectance), we can adjust ε at the heads of channels 2 and 3. If we increase the reflectance in channel 3 to reflect completely (ε_3=1), we find that a_{L3} still does not depend on L_2 since there remains no return wave in channel 2. On the other hand, a_{L2} and a_{L3} show strong dependency on L_3 (Figure 4-4). In this case, for most values of L_3, a_{L2} and a_{L3} are similar in magnitude, approaching 4/3 m. Although the heads of the two channels show similar amplitudes for most values of L_3, they come about them differently, as a_{L3} is the sum of the forward and backwards wave at L_3, while a_{L2} is just a forward wave. Notably, a_{L2} drops to zero periodically (every $\lambda/2$ starting at $\lambda/4$) as a function of L_3, while a_{L3} spikes as high as 4 m on the same cycle. We discuss these relationships below.

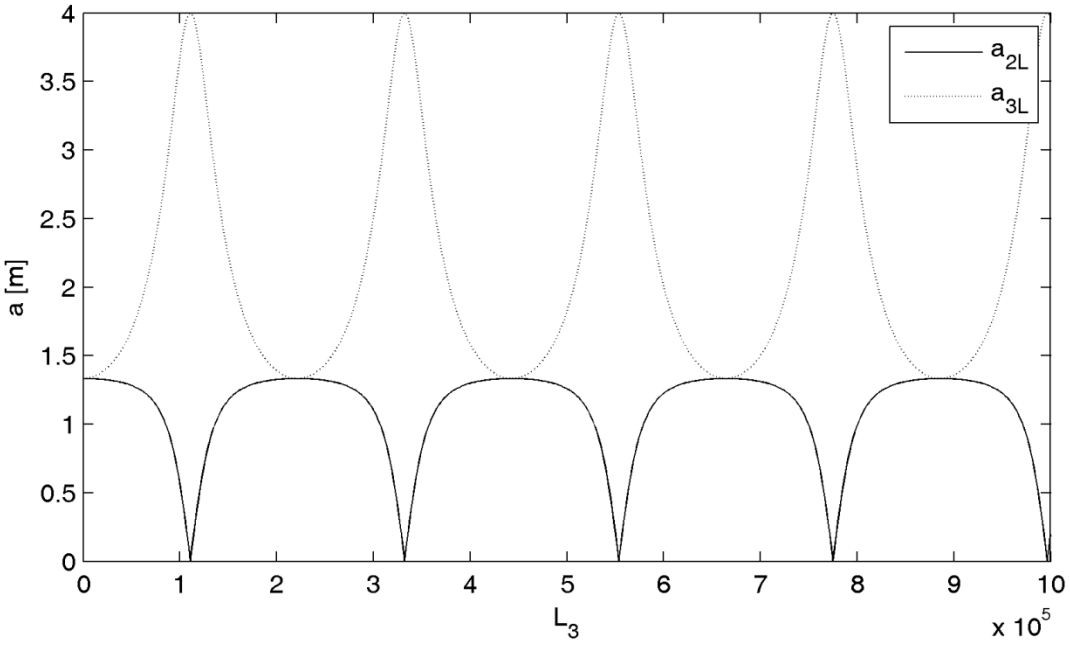

Figure 4-4. Even Split Case: Inviscid (Case 3.1b). The amplitude at the heads of channels 2 and 3 as a function of the length of channel 3. With friction turned off and 100% reflectance at the end of channel 3, superposition of forward and backward waves at the head of channel 3 lead to large amplification when the channel approaches the amplification lengths. At these lengths, channel 3 maintains zero amplitude at its mouth at all time, causing tidal amplitudes at the head of (and throughout) channel 2 to zero. (Note: The wavelength, λ, for an inviscid wave in 10 m of water is 4.43 x 10^5 m.)

Case 3.1c: If we turn friction on for the simulation, we damp these effects (Figure 4-5). Because ε_2 equals zero, a_{L3} still does not depend on L_2, but we see a_{L3} go to zero as L_3 increases. Within channel 2, a_{L2} decreases as L_2 increases but a_{L2} shows a stronger dependence on L_3. The sharp peaks we saw in a_{L3} are lessened, while a_{L2} no longer drops to zero.

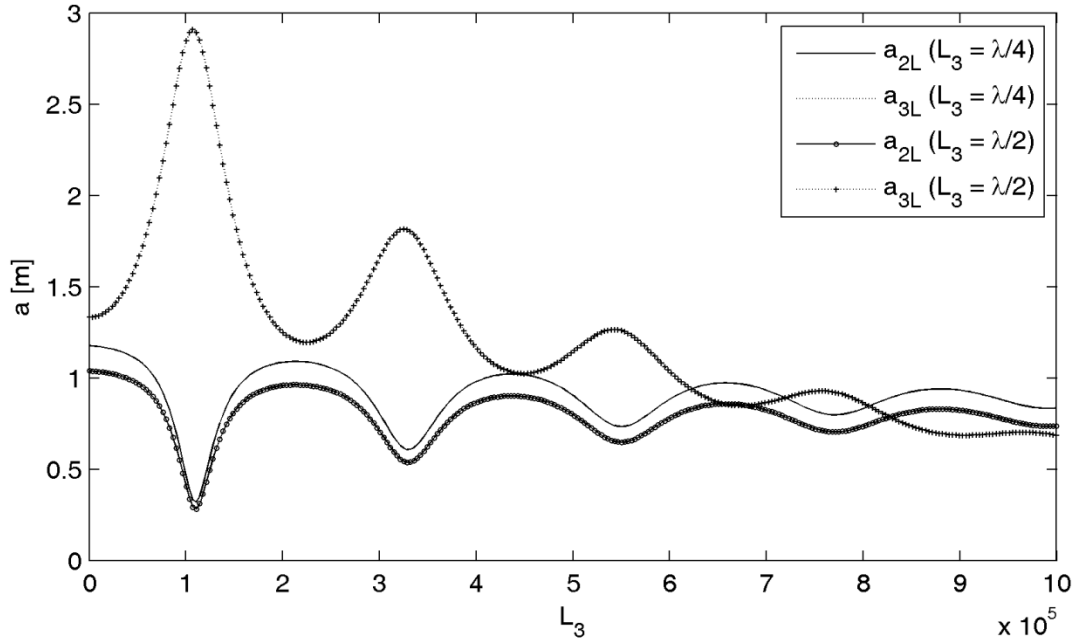

Figure 4-5: Even Split Case: Frictional (Case 3.1c). If friction is turned on, resonance becomes less of a factor. The return wave decays over the length of channel 3, reducing its ability to cancel out the forward wave. This lessens the ability of channel 3 to dominate the dynamics in channel 2 when channel 3 approaches resonance lengths. As channel 3 gets longer, tidal amplitudes within it decrease, and channel 2 is no longer dominated by resonance in channel 3. Amplitudes in channel 2 asymptotes towards some value set by its own geometry and frictional characteristics.

4.3.1.2 Even Split Case Discussion: When the length of the channel is $n\lambda/2$, where n is a positive integer, a_{L2} and a_{L3} are similar in magnitude due to constraints on the free surface (equation (4-34)) at the junction and no energy losses along the channel. However, since the reflectance at the head of each channel is different, a_{L2} is a entirely formed by f_2 while a_{L3} is a split between f_3 and b_3.

If the length of a channel equals the quarter wavelength ($\lambda/4$) of the tidal wave (or $(2n-1)*\lambda/4$; this is the "quarter wave resonator"), however, then f_3 and b_3 will be out of phase at the junction at all times. In a simple non-branching system, this could lead to the "infinite amplification" condition, wherein the waves in the channel reinforce each other at the head of the channel but cancel each other out completely at the mouth. In this case, however, the "mouth" is the junction. If channel 3 is a quarter wave resonator, it will, in effect, maintain zero amplitude at the junction and prevent any waveforms from traveling down channel 2. This can be seen in Figure 4-5, where the tidal amplitude at the head of channel 2 is shown to drop as L_3 approaches $(2n-1)*\lambda/4$. This creates an interesting amplification in channel 3, however, as mass conservation requires the flow that otherwise would have travelled into channel 2 to flow into channel 3. Both f_3 and b_3 double in this case, leading to tidal amplitudes at the head of 4 m (Figure 4-4). This is a very large amplification considering the inviscid, no reflection case where tidal amplitudes were 1 m everywhere. This difference is more interesting considering the only change in the system was to increase the reflectance at the end of channel 3.

With friction on, a_{L2} and a_{L3} respond differently to increased L_3. As the length of channel 3 increases, amplitudes at its head decrease due to the decrease in wave height from the friction acting over longer distances. This has the added effect of turning off the quarter wave resonator, as the backward wave ends up much smaller than the forward wave in channel 3. If channel 3 is long

enough, the reflectance at its head no longer matters. This, in turn, means that channel 3 does not have the huge effect on the junction that it once had. As a result, as channel 3 lengthens, a_{L2} asymptotes. In the case of large L_3, the branching channels split the incident wave evenly, just like in the inviscid case with ε_2, $\varepsilon_3 = 0$. The wave in channel 2 decays along it to some finite value at the head. The wave in channel 3 decays to zero as it travels down channel 3. If friction is increased, this decay will happen over shorter length scales; tidal penetration decreases with increased friction. Conversely, if friction is decreased, tidal penetration will increase.

4.3.1.3 Uneven Split Case: To explore the effect of differing cross sections between the two branches, we will explore two sub-cases: varying depth (case 3.1d) and width (case 3.1e). In both cases, we will maintain $\varepsilon_2 = 0$ and $\varepsilon_3 = 1$ with friction turned off. If we vary the depth in channel 3 (setting H_3 = 5 m or 20 m and keeping the widths in the two channels equal at 100 m), the amplitudes at the heads of the branches shows similar functional relationship to L_3, but with different periodicity and different max values for a_{L3} (Figure 4-6). Altering the width (setting B_3 = 50 m or 200 m), on the other hand, does not affect the periodicity, but has a large effect on the magnitude of the tidal amplitudes at the heads of the channels (Figure 4-7).

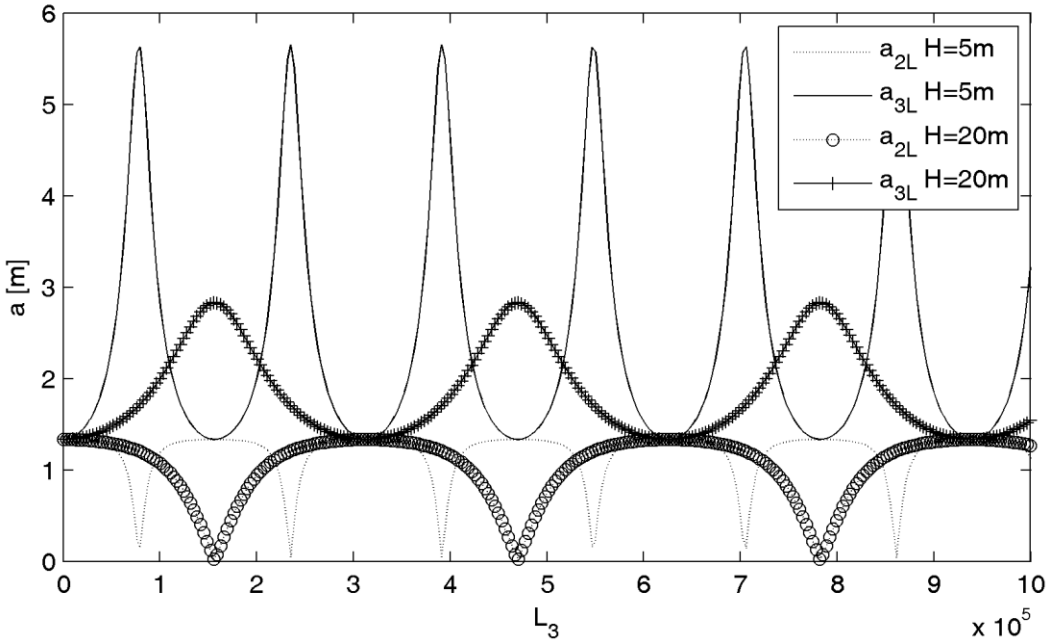

Figure 4-6: Tidal amplitude at the head of channels 2 and 3 as a function of the width of channel 3 and the depth of channel 3 (Case 3.1d). As channel 3 deepens, the wave speed within it increases, enabling it to accommodate larger flows. This makes the amplitude at its head less affected by tidal resonance. The periodicity of the resonance condition lengthens as the wavelength increases in deeper water.

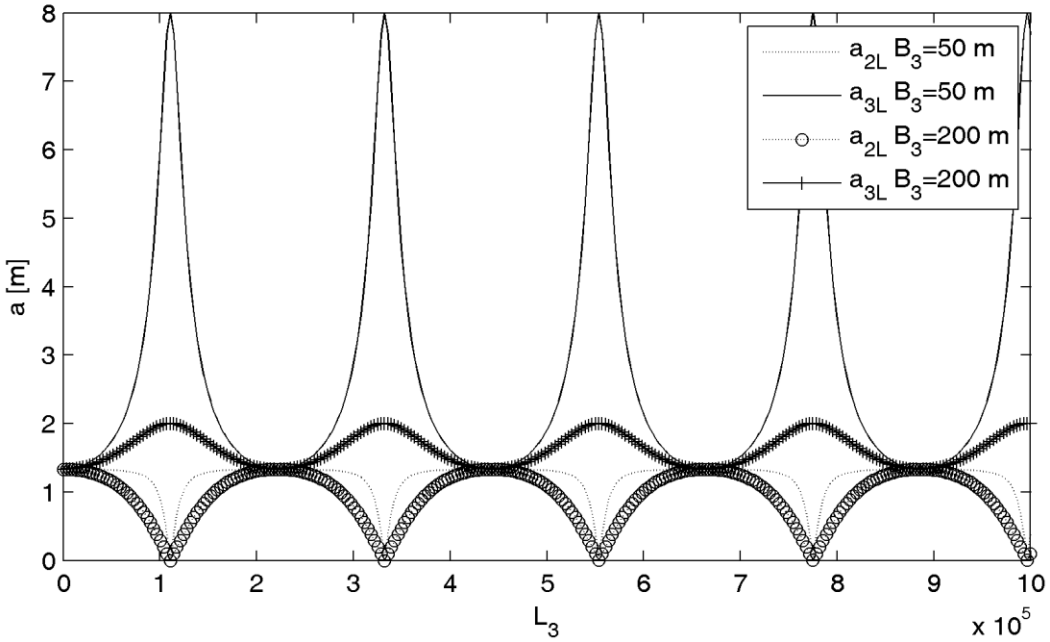

Figure 4-7: Tidal amplitude at the head of channels 2 and 3 as a function of the width of channel 3 and the length of channel 3 (Case 3.1e). Tidal amplitudes at the head of channel 3 become amplify less as the width of channel 3 increases and gives the channel the ability to accommodate larger flows. Channel 2 still feels the effects of resonance, as the amplitude of the waves in it drop to zero periodically, but the drop begins further from the quarter wavelength condition.

4.3.1.4 Uneven Split Case Discussion: With uneven branch sizes, the tidal waves do not respond as they might otherwise. The channels still respond to the quarter wave resonance condition, but the degree to which they amplify is affected due to the conservation of mass. Equation (4-28), which expresses the volumetric flux through a cross-section, shows that volumetric flux varies linearly with width; the dependence on depth is buried in the wave number, whence it can be shown that volumetric flux goes as $H^{1/2}$ in the inviscid, prismatic case (equations (4-18), (4-19), and (4-22)). Because of this difference in power, amplification at the head of channel 3 is more sensitive to width than to depth. The periodicity, however, is only a function of depth, as the wavelength is a function of wave number, which depends on depth, not width.

4.3.2 Case Study: The Sacramento-San Joaquin Delta

The Sacramento-San Joaquin Delta is dominated by freshwater inputs from its namesake rivers (Figure 4-2). The Sacramento and San Joaquin Rivers wills serve in this section as channels 2 and 3 served in the last. Friction will be turned on for this case study.

These rivers have identical characteristic cross-sectional areas near their confluence, but different aspect ratios. This will affect flow through the confluence since volumetric flux is more strongly correlated with width than depth (see section 4.3.1.4). In this section, we will not encounter length-scales as long as were explored in the last section, since the locations of interest are all less than one quarter wavelength from the confluence.

Table 4-2. The set-up and geometry for all cases within the Sacramento-San Joaquin Case Study. All channel geometries are in meters.

		3.2a	3.2b	3.2c
	L_{con}	0	0	0
	B_{con}	1000	1000	1000
Confluence	H_{con}	15	15	15
	L_{Sac}	3.5×10^4	3.5×10^4	3.5×10^4
	B_{Sac}	800	800	800
Sacramento River	H_{Sac}	10	10	10
	L_{SJ}	varies	varies	varies
	B_{SJ}	400	400	400
San Joaquin River	H_{SJ}	20	20	20
	Friction	On	On	On
	ε_{RV}	0	0	0
	ε_{SJ}	varies	0	1

4.3.2.1 Restoration on the San Joaquin Results: Case 3.2a: Using characteristic width and depths for the two rivers and the confluence (Sacramento 800 m x 10 m; San Joaquin 400 m x 20 m; confluence 1000 m x 15 m), we analyze what effects restoration efforts on the San Joaquin would have on the Sacramento River near Rio Vista (roughly 35 river km upstream of the confluence.) Based on analyses from section 4.3.1, the location of the restoration will matter. Thus, we will vary the reflectance at the head of the San Joaquin, as well as the "length" of the San Joaquin. In this case, the length will refer to the location of the restoration site. With the San Joaquin having a tidal excursion of O(100 km) upstream of the confluence, we will limit our analysis to these lengthscales. Since the wavelength in 20 m depths is greater than 600 km, we will not see the lengths tested above, though we will approach the quarter wavelength.

Generally speaking, greater reflectances lead to larger tidal amplitudes at Rio Vista (Figure 4-8). If there is no reflectance at the site in question, its proximity to the confluence has no effect on the tidal amplitude in the other branch. If the reflectance is high (due to a barrier or levee) and near the confluence, tidal amplitudes at Rio Vista can be 20% higher than if the reflectance is low. If the barrier or levee is farther down the San Joaquin, amplitudes at Rio Vista can be 10% lower than if the barrier is near the confluence.

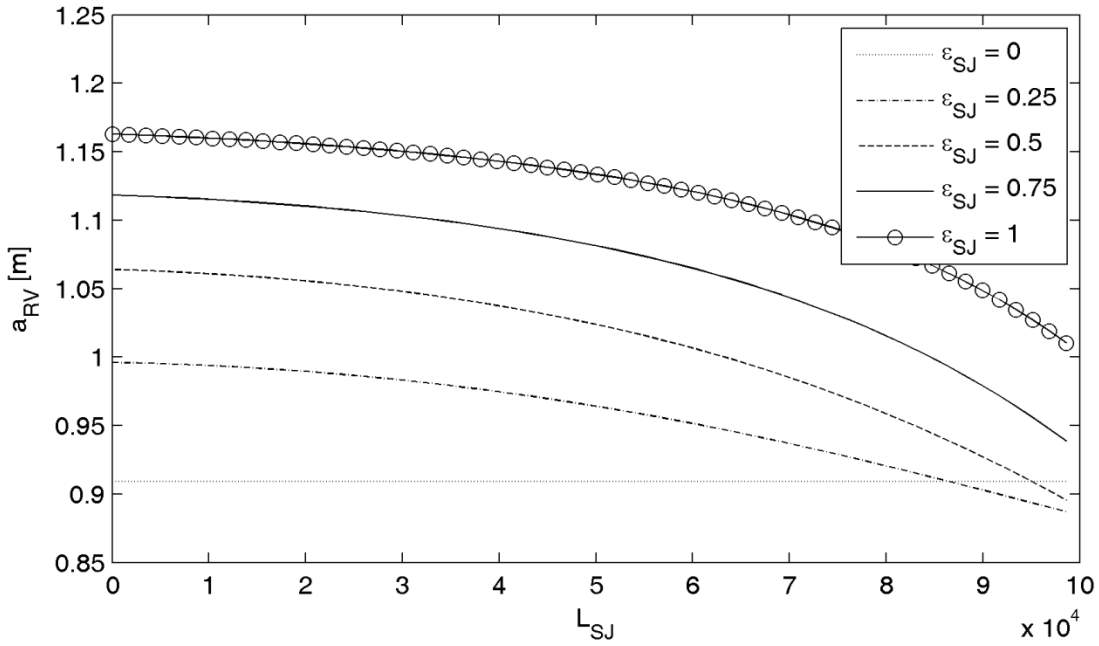

Figure 4-8: Effects of Restoration on the San Joaquin on Tidal Amplitudes near Rio Vista (Case 3.2a). Due to the variance in the location along the San Joaquin River and the level of reflectance at that location, the tidal amplitude at Rio Vista is affected. As the length along the San Joaquin increases, the channel approaches resonance, causing decreases in tidal amplitudes as large as 0.1 m, depending on the reflectance, at Rio Vista, on the Sacramento River. If the reflectance on the San Joaquin decreases, less wave energy will reach Rio Vista.

4.3.2.2 Restoration on the San Joaquin Discussion: If the reflectance at the head of the channel is high, the tidal amplitudes drop sharply as the length to the reflection increases. This is due to the channel approaching the quarter wave resonator condition. If the reflectance is decreased in a short channel, the tidal amplitude at Rio Vista can be decreased by 20%. If the channel is longer, the effect is lessened, as resonance becomes more important than reflectance.

4.3.2.3 Restoration on the Sacramento: Using the same characteristic width and depths for the two rivers and the confluence, we analyze what effects restoration efforts on the Sacramento River near Rio Vista would have on locations along the San Joaquin River. The length, in this case, will refer to locations along the San Joaquin. We will analyze two sub-cases (Case 3.2b and 3.2c, respectively): one with reflectance at the San Joaquin site equal to zero ($\varepsilon_{SJ} = 0$); the other with it equal to one ($\varepsilon_{SJ} = 1$).

If $\varepsilon_{SJ} = 0$, decreased reflectances at Rio Vista leads to decreases in tidal amplitudes along the San Joaquin (Figure 4-9). This follows from analyses from above (Cases 3.1a and 3.1b). While this relationship generally holds if we reflect the waves at the San Joaquin site, the amplitudes are much greater (Figure 4-10). Further, the amplitudes increase greatly with increasing channel length.

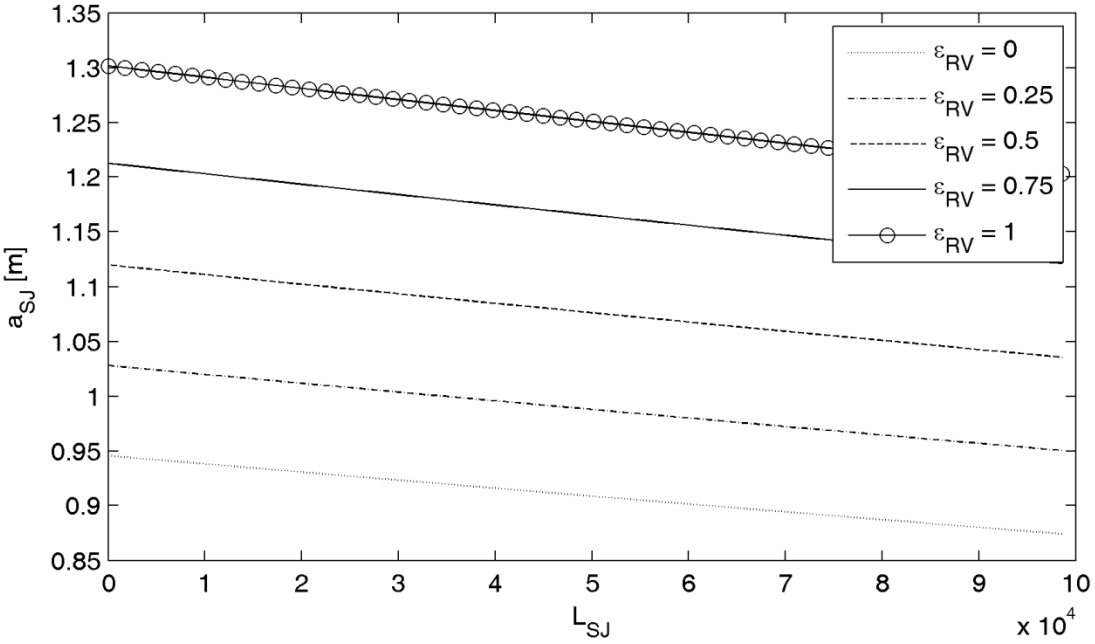

Figure 4-9: Effect of restoration at Rio Vista on the San Joaquin with no reflection on the San Joaquin (Case 3.2b). If the reflectance at Rio Vista decreases, less energy will reflect and enhance tidal amplitudes on the San Joaquin. Tidal amplitude along the San Joaquin will decrease along the channel as friction slowly decreases the forward wave height.

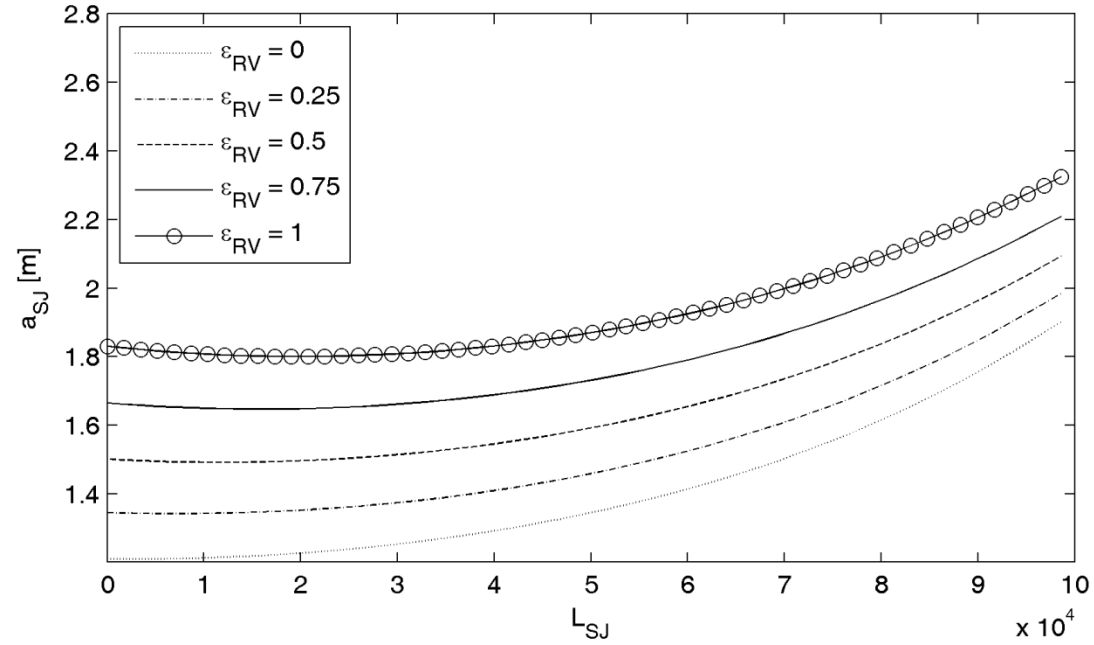

Figure 4-10: Effect of Restoration at Rio Vista on the San Joaquin with 100% reflectance on the San Joaquin (Case 3.2c). With reflection on San Joaquin, the effects of resonance become pronounced as the location under consideration moves farther from the confluence. As in Figure 4-9, increased reflection at Rio Vista increases wave amplitudes along the San Joaquin, but resonance greater over powers friction on these length-scales.

4.3.2.4 Restoration on the Sacramento Discussion: From discussions above, the reaction of the system to restoration at Rio Vista makes sense: in the absence of reflection at the end of a channel,

the tidal amplitude decreases along the channel. This is due to friction as the channel lengthens and the absence of a return wave. If the reflection is high, then resonance dominates as the channel approaches the quarter wavelength.

4.4 General Discussion

We have presented results of a simple mathematical model of tidal dynamics in two simplified systems. The idealized systems in this study ignore the many connecting branches in more realistic systems which provide dissipation on their own, but also might allow tidal energy to bypass restoration sites and lose less energy because of it. Further, our system ignores bathymetric variability within larger branches which can serve as a source of energy dissipation. Although more computationally expensive 3D numerical models are likely needed to address specific questions regarding specific locations, we can generalize a few keys findings from this study.

1) Changing reflectances within a branching system can have large effects throughout the system regardless of channel length or friction. Figures 4-8 through 4-10 show changes in tidal amplitudes on the order of 10% for differences in reflectance of 0.25. Although changing the reflectance of a major river by that much might be very difficult unless a major new levee is built (or a levee fails), it is likely that these sorts of changes can occur locally near marsh restoration within the much larger system. Further, ecosystem response to disturbance is usually non-linear (Koch et al. 2009; Mayer and Rietkerk 2004), so even small changes to tidal amplitudes may matter.

2) In systems large enough to approach resonant length-scales, changes to reflectance should be carefully considered. If the functioning marsh or sensitive levees are near resonance length-scales along a branch of an estuary, changes to the other branch could exacerbate already-large tides.

3) Friction lessens the impact of resonance. As frictional effects slowly weaken wave forms, the effects of wave reflection lessens. If channels are long enough, friction can eliminate the interconnectivity of the branches, making each branch, in effect, independent of changes along the other. To analyse this, we plot a_{L2} versus a_{L3} (Figure 4-11) for the even-split geometry while varying friction and holding $L_2 = \lambda/2$. As L_3 increases, if there is no friction, a_{2L} oscillates from zero (resonance condition) to 4/3 m while a_{3L} oscillates from 4 m (resonance condition) to 4/3 m. As F is increased from zero to $64H/T$, friction damps the resonance characteristics of the system, decreasing the peaks in a_{L3} and lessening a_{L2}'s dependence on the length of channel 3. If the system is long enough, even low levels of friction can bring the system to a steady-state at the head of channel 2. If friction is high enough, a_{L2} is almost completely independent of L_3.

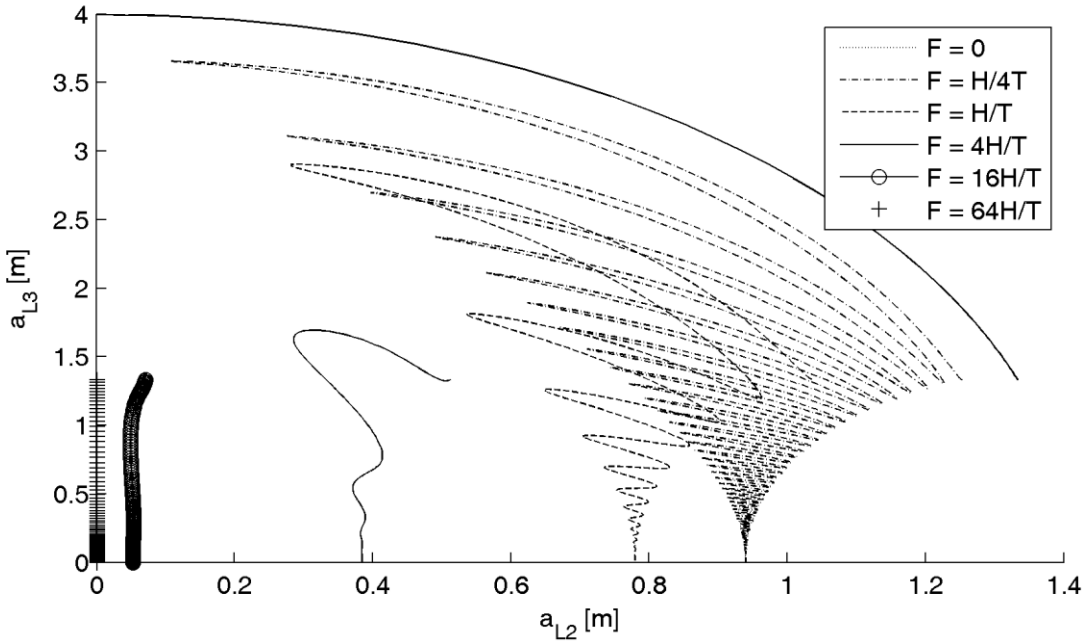

Figure 4-11. Frictional impacts on resonance. Plotting a_{L2} versus a_{L3} for the even-split geometry while varying friction and holding $L_2 = \lambda/2$. (Note: the first and third lines were plotted in figures 4-4 and 4-5 as amplitudes versus L_3. In this case we plot the amplitudes against each other.) The lines represent the dependence on L_3. Looking at the $F = H/4T$ line: For $L_3 = 0$, the line begins with the highest value of a_{L2}; when $L_3 = \lambda/4$ (resonance condition), a_{L3} reaches it's highest value. For higher values of friction, both amplitudes and oscillation frequency are damped.

4) Changes to reflectance and friction change the transport of scalars within the branching channel system. Although this is beyond the scope of this chapter, the ratio of the forward wave to the backward wave helps determine the mass flux due to wave transport within a estuarine channel. Changes to the channel's reflectance will affect how much mass will be transported by tidal wave energy and how much will either a) be stored within the system or b) flow out the system as river flow. This could have huge implications physically, chemically, and biologically, as mixing and flow regimes evolve as the system is altered.

4.5 Summary

We developed linearized wave equations that account for channel geometry, friction, and wave amplification and use them to solve for tidal wave amplitudes throughout branching prismatic channel systems by applying matching conditions at the junctions. By adjusting the channel lengths and reflectances at their heads, we are able to analyze system response to a number of different scenarios. Tidal amplitudes throughout a system are controlled primarily by the system's geometry; mass conservation can create huge amplitudes in certain locations due to resonance or greatly limit the effect of resonance in other cases. Friction, when allowed to act over sufficient distances, can greatly diminish the importance of resonance (or reflectance near the head.) Changes to friction or reflectance can have huge implication on mass transport within a channel, affecting the balance between tidal time-scale transport to river flow transport.

Chapter 5

Conclusions

5.1 Summary and Implications

We set out to answer the fundamental question: What are the thermal mixing dynamics and the physical processes that control them within an estuary at a variety of length- and time-scales? This work focused on physical processes and their implications for ecosystem health and restoration. The question was sub-divided into three research questions.

1) How do water temperatures vary on large length- and time-scales across the Delta? What does this imply for critical species in the Delta, specifically the delta smelt. (Chapter 2)

Daily water temperatures vary seasonally across the Delta, but sites within the Delta behave somewhat independently of each other. The central Delta serves as a mixed region as waters from the Sacramento and San Joaquin Rivers mix with San Francisco Bay waters. Thermally, sites in the north are dominated by the Sacramento River, sites in the south by the San Joaquin, and sites in the west by the San Francisco Bay. All regions are relatively free of thermal influence from upstream dam releases, although yearly flow regimes do appear to decrease yearly-averaged Delta water temperatures by order 1°C as high flows cool the Delta temporarily.

Using a simple model driven by global circulation models, we project water temperatures in the Delta to increase across all climate scenarios. This increase will affect the delta smelt through increases in the number of days in which the smelt's thermal limit is reached. Further, the Delta smelt's spawning window is likely to shift earlier in the year. These conditions could lead to ecological bottlenecks for this critical fish.

2) What controls temperature and thermal gradients within a tidal slough? Can this be managed to improve thermal refugia for species? (Chapter 3)

Thermal gradients within Cache Slough are formed through a combination of processes. Along-channel gradients are formed by interactions between along-channel thermal gradients and along-channel velocity gradients. Lateral gradients are formed by differential advection of temperature; this can be due to either a lateral velocity gradient or a lateral temperature gradient from atmospheric effects on different depths. Vertical gradients are formed predominantly by atmospheric heating from above, but the relaxation of lateral gradients near the turn of the tide does sometimes create vertical stratification. Wind plays a major role in lateral circulations, but this circulation does not affect along-channel thermal mixing.

These gradients are quite large biologically. If the Delta smelt thermal limit is tightly defined at 25°C, then within cross-section lateral temperature differences in May of 1.2°C and vertical temperature differences of 2.8°C are important. Since these gradients are initially formed by differential heating within the Delta, local bathymetry plays a leading role in the formation of thermal refugia. Tides advect these refugia within the region, so their location will not be static, nor will they last indefinitely.

3) How do tides interact across junctions? Will restoration efforts affect ecologically functional systems elsewhere in the estuary? (Chapter 4)

Reflectances at the head of a channel can be adjusted through levee construction, wetland creation, or island flooding. Tidal amplitudes at the heads of two intersecting channels interact as energy reflects within the system and through their junction. Tidal effects from one channel to the other is most prominant when branches of the estuary are near resonant length-scales, often causing ramping near the heads of the channel and damping near the junction (and in the other junction). Friction, by damping return waves, can greatly reduce this resonant condition. In the Sacramento-San Joaquin, changes in reflectance of 25% in one channel can affect tidal amplitude in the other channel by order 10%. These changes can affect the function of other wetland systems as tidal amplitude is important to, for example, the ability of plants to establish roots (Boorman et al. 2001) or nekton access to wetlands (Rozas 1995).

5.2 Future Work

Future work should address the options for management and mitigation of the projected temperature rise for maintaining habitat quality. Although our modeling study indicated only limited effects on local water temperature, later work (Appendix A) indicated a relationship between river flow and mean annual water temperature. This suggests, for instance, that efforts to restore flow in the Delta may have the additional effect of buffering against climate-change induced temperature rises. If flows are responsible for larger-than-usual weekly to monthly time-scale residuals in our water temperature model as shown in Figure 2-9, then managed releases of stored water may provide a short-term option for mitigating extreme heat events. Our model creates a great starting point for water temperature forecasts, accurately predicting long-term water temperatures. Our field work indicates that local conditions can vary greatly over small length-scales. Future work should focus specifically on the effects of reservoir releases on water temperatures throughout the Delta. Additionally, future work can focus on the temporal and spatial effects of flooded islands on the thermal regimes of nearby regions of the Delta.

With respect to tidal interconnectivity, our simple tidal model highlights how tidal amplitudes are affected due to changes in one branch of an estuary. The simple model presented here highlights the scales of the response to expect. This problem is relatively unstudied, and further research is needed. If the scales of response are large enough to affect the functioning ecosystems within the Delta, then this issue should be considered when changing the Delta infrastructure. At that point, more detailed 3D hydrodynamic models can be employed to fine tune system response to change. In the meantime, these simple tools presented here offer powerful insights into the Delta's systemic responses to forcing and change.

References

Athearn, N. D., et al. (2010), 'Mapping Elevations of Tidal Wetland Restoration Sites in San Francisco Bay: Comparing Accuracy of Aerial Lidar with a Singlebeam Echosounder', *Journal of Coastal Research,* 26 (2), 312-19.

Baker, P. F., Speed, T. P., and Ligon, F. K. (1995), 'Estimating the Influence of Temperature on the Survival of Chinook Salmon Smolts (Oncorhynchus-Tshawytscha) Migrating through the Sacramento-San-Joaquin River Delta of California', *Canadian Journal of Fisheries and Aquatic Sciences,* 52 (4), 855-63.

Banas, N. S. and Hickey, B. M. (2005), 'Mapping exchange and residence time in a model of Willapa Bay, Washington, a branching, macrotidal estuary', *Journal of Geophysical Research-Oceans,* 110 (C11).

Barnett, T. P., et al. (2008), 'Human-induced changes in the hydrology of the western United States', *Science,* 319 (5866), 1080-83.

Bartholow, J.M. (1989), 'Stream temperature investigations: field and analytic methods. Instream Flow Information Paper No. 13.', *U.S. Fish and Wildlife Service Biological Report,* 89 (17), 139.

Bennett, William A. (2005), 'Critical assessment of the delta smelt population in the San Francisco Estuary, California', *San Francisco Estuary and Watershed Science,* 3 (2).

Benyahya, L., et al. (2007), 'Modeling of water temperatures based on stochastic approaches: case study of the Deschutes River', *Journal of Environmental Engineering and Science,* 6 (4), 437-48.

Blasco, F., Saenger, P., and Janodet, E. (1996), 'Mangroves as indicators of coastal change', *Catena,* 27 (3-4), 167-78.

Boorman, L. A., Hazelden, J., and Boorman, M. (2001), 'The effect of rates of sedimentation and tidal submersion regimes on the growth of salt marsh plants', *Continental Shelf Research,* 21 (18-19), 2155-65.

Bradley, A. Allen, et al. (1998), 'Estimation of Water Temperature Exceedence Probabilities Using Thermo-Hydrodynamic Modeling', *Journal of the American Water Resources Association,* 34 (3), 467-80.

Brew, D. S. and Williams, P. B. (2010), 'Predicting the Impact of Large-Scale Tidal Wetland Restoration on Morphodynamics and Habitat Evolution in South San Francisco Bay, California', *Journal of Coastal Research,* 26 (5), 912-24.

Broome, S. W., Seneca, E. D., and Woodhouse, W. W. (1988), 'Tidal Salt-Marsh Restoration', *Aquatic Botany,* 32 (1-2), 1-22.

Burchard, H., et al. (2011), 'Drivers of Residual Estuarine Circulation in Tidally Energetic Estuaries: Straight and Irrotational Channels with Parabolic Cross Section', *Journal of Physical Oceanography,* 41 (3), 548-70.

Burdick, D., et al. (1997), 'Ecological responses to tidal restorations of two northern New England salt marshes', *Hydrologic Restoration of Coastal Wetlands,* 4 (2), 129-44.

Caissie, D., El-Jabi, N., and Satish, M. G. (2001), 'Modelling of maximum daily water temperatures in a small stream using air temperatures', *Journal of Hydrology,* 251 (1-2), 14-28.

Cayan, Dan, et al. (2009), 'Climate change scenarios and sea level rise estimates for California 2008 Climate Change Scenarios Assessment: California Energy Commission Report', 62.

Chant, R. J. (2002), 'Secondary circulation in a region of flow curvature: Relationship with tidal forcing and river discharge', *Journal of Geophysical Research-Oceans,* 107 (C9).

Chen, S. N. and Sanford, L. P. (2009), 'Axial Wind Effects on Stratification and Longitudinal Salt Transport in an Idealized, Partially Mixed Estuary', *Journal of Physical Oceanography,* 39 (8), 1905-20.

Chen, S. N., Sanford, L. P., and Ralston, D. K. (2009), 'Lateral circulation and sediment transport driven by axial winds in an idealized, partially mixed estuary', *Journal of Geophysical Research-Oceans,* 114.
Cheng, P., et al. (2009), 'Modeling Influence of Stratification on Lateral Circulation in a Stratified Estuary', *Journal of Physical Oceanography,* 39 (9), 2324-37.
Christiansen, T., Wiberg, P. L., and Milligan, T. G. (2000), 'Flow and sediment transport on a tidal salt marsh surface', *Estuarine Coastal and Shelf Science,* 50 (3), 315-31.
Cloern, J. E., et al. (2011), 'Projected Evolution of California's San Francisco Bay-Delta-River System in a Century of Climate Change', *Plos One,* 6 (9).
Coutant, C (1976), 'Thermal effects on fish ecology', *Encyclopedia of Environmental Science and Engineering* (New York: Gordon and Breach Publishers), 891-96.
Cronin, T. W. (1982), 'Estuarine Retention of Larvae of the Crab Rhithropanopeus-Harrisii', *Estuarine Coastal and Shelf Science,* 15 (2), 207-20.
Crump, B. C., et al. (2004), 'Microbial biogeography along an estuarine salinity gradient: Combined influences of bacterial growth and residence time', *Applied and Environmental Microbiology,* 70 (3), 1494-505.
Cyrus, D. P. and Blaber, S. J. M. (1987), 'The Influence of Turbidity on Juvenile Marine Fishes in Estuaries .2. Laboratory Studies, Comparisons with Field Data and Conclusions', *Journal of Experimental Marine Biology and Ecology,* 109 (1), 71-91.
Das, T., et al. (2005), 'Thermal tolerance, growth and oxygen consumption of Labeo rohita fry (Hamilton, 1822) acclimated to four temperatures', *Journal of Thermal Biology,* 30 (5), 378-83.
Dauer, D. M., Rodi, A. J., and Ranasinghe, J. A. (1992), 'Effects of Low Dissolved-Oxygen Events on the Macrobenthos of the Lower Chesapeake Bay', *Estuaries,* 15 (3), 384-91.
Delworth, T. L., et al. (2006), 'GFDL's CM2 global coupled climate models. Part I: Formulation and simulation characteristics', *Journal of Climate,* 19 (5), 643-74.
Elliott, M. and McLusky, D. S. (2002), 'The need for definitions in understanding estuaries', *Estuarine Coastal and Shelf Science,* 55 (6), 815-27.
Eyre, B. D. (2000), 'Regional evaluation of nutrient transformation and phytoplankton growth in nine river-dominated sub-tropical east Australian estuaries', *Marine Ecology-Progress Series,* 205, 61-83.
Fischer, Hugo B., et al. (1979), *Mixing in inland and coastal waters* (New York: Academic Press) xiv, 483 p.
Fisher, T. R., et al. (1988), 'Phytoplankton, Nutrients, and Turbidity in the Chesapeake, Delaware, and Hudson Estuaries', *Estuarine Coastal and Shelf Science,* 27 (1), 61-93.
Fortier, L. and Leggett, W. C. (1982), 'Fickian Transport and the Dispersal of Fish Larvae in Estuaries', *Canadian Journal of Fisheries and Aquatic Sciences,* 39 (8), 1150-63.
Garrick, M., Cunnane, C., and Nash, J. E. (1978), 'Criterion of Efficiency for Rainfall-Runoff Models', *Journal of Hydrology,* 36 (3-4), 375-81.
Geist, D. R., et al. (2005), 'Movement, swimming speed, and oxygen consumption of juvenile white sturgeon in response to changing flow, water temperature, and light level in the Snake River, Idaho', *Transactions of the American Fisheries Society,* 134 (4), 803-16.
Geyer, W. R., Chant, R., and Houghton, R. (2008), 'Tidal and spring-neap variations in horizontal dispersion in a partially mixed estuary', *Journal of Geophysical Research-Oceans,* 113 (C7).
Haller, W. T., Sutton, D. L., and Barlowe, W. C. (1974), 'Effects of Salinity on Growth of Several Aquatic Macrophytes', *Ecology,* 55 (4), 891-94.

Hidalgo, Hugo G., Dettinger, Michael D., and Cayan, Daniel R. (2008), 'Downscaling with constructed analogues - Daily precipitation and temperature fields over the United States: California Energy Commission PIER Final Project Report ', 48.
Hotta, K. , et al. (2001), 'Changes in spawning characteristics of Japanese whiting Sillago japonica under control of temperature', *Fisheries Science,* 67 (6), 1111-18.
Jacobs, S., et al. (2009), 'Restoration of tidal freshwater vegetation using controlled reduced tide (CRT) along the Schelde Estuary (Belgium)', *Estuarine Coastal and Shelf Science,* 85 (3), 368-76.
Jassby, A. D., et al. (1995), 'Isohaline Position as a Habitat Indicator for Estuarine Populations', *Ecological Applications,* 5 (1), 272-89.
Johnson, T. B. and Evans, D. O. (1996), 'Temperature constraints on overwinter survival of age-0 white perch', *Transactions of the American Fisheries Society,* 125 (3), 466-71.
Kalkwijk, J. P. T. and Booij, R. (1986), 'Adaptation of Secondary Flow in Nearly-Horizontal Flow', *Journal of Hydraulic Research,* 24 (1), 19-37.
Kimmerer, Wim (2004), 'Open water processes of the San Francisco Estuary: from physical forcing to biological responses', *San Francisco Estuary & Watershed Science,* 2 (1), Unpaginated.
Koch, E. W., et al. (2009), 'Non-linearity in ecosystem services: temporal and spatial variability in coastal protection', *Frontiers in Ecology and the Environment,* 7 (1), 29-37.
Lacy, J. R. and Monismith, S. G. (2001), 'Secondary currents in a curved, stratified, estuarine channel', *Journal of Geophysical Research-Oceans,* 106 (C12), 31283-302.
Lacy, J. R., et al. (2003), 'Interaction of lateral baroclinic forcing and turbulence in an estuary', *Journal of Geophysical Research-Oceans,* 108 (C3), -.
Lankford, T. E. and Targett, T. E. (1994), 'Suitability of Estuarine Nursery Zones for Juvenile Weakfish (Cynoscion Regalis) - Effects of Temperature and Salinity on Feeding, Growth and Survival', *Marine Biology,* 119 (4), 611-20.
Largier, J. L. (1993), 'Estuarine Fronts - How Important Are They', *Estuaries,* 16 (1), 1-11.
Lemos, R. T., Sanso, B., and Huertos, M. L. (2007), 'Spatially varying temperature trends in a Central California estuary', *Journal of Agricultural Biological and Environmental Statistics,* 12 (3), 379-96.
Lerczak, J. A. and Geyer, W. R. (2004), 'Modeling the lateral circulation in straight, stratified estuaries', *Journal of Physical Oceanography,* 34 (6), 1410-28.
Lighthill, M. J. (1978), *Waves in fluids* (Cambridge Eng. ; New York: Cambridge University Press) xv, 504 p.
Loarie, Scott R., et al. (2008), 'Climate Change and the Future of California's Endemic Flora', *PLoS ONE,* 3 (6), e2502.
Lund, J., et al. (2007), *Envisioning Futures for the Sacramento-San Joaquin Delta* (San Francisco, CA: Public Policy Institute of California) x, 285.
MacVean, Lissa and Stacey, Mark (2010), 'Estuarine Dispersion from Tidal Trapping: A New Analytical Framework', *Estuaries and Coasts*, 1-15.
Marce, R. and Armengol, J. (2008), 'Modelling river water temperature using deterministic, empirical, and hybrid formulations in a Mediterranean stream', *Hydrological Processes,* 22 (17), 3418-30.
Mayer, A. L. and Rietkerk, M. (2004), 'The dynamic regime concept for ecosystem management and restoration', *Bioscience,* 54 (11), 1013-20.
Meehl, G. A., et al. (2007), 'The WCRP CMIP3 multimodel dataset - A new era in climate change research', *Bulletin of the American Meteorological Society,* 88 (9), 1383-94.
Mitsuta, Y. and Tsukamoto, O (1978), 'Drag Coefficients in Light Wind', *Bulletin of the Disaster Prevention Research Institute,* 28 (2), 25-32.

Miyakoda, K. and Rosati, A. (1984), 'The Variation of Sea-Surface Temperature in 1976 and 1977 .2. The Simulation with Mixed Layer Models', *Journal of Geophysical Research-Oceans,* 89 (Nc4), 6533-42.

Mohseni, O., Erickson, T. R., and Stefan, H. G. (1999), 'Sensitivity of stream temperatures in the United States to air temperatures projected under a global warming scenario', *Water Resources Research,* 35 (12), 3723-33.

Moller, I., et al. (1999), 'Wave transformation over salt marshes: A field and numerical modelling study from north Norfolk, England', *Estuarine Coastal and Shelf Science,* 49 (3), 411-26.

Monismith, S. G., et al. (2009), 'Thermal Variability in a Tidal River', *Estuaries and Coasts,* 32 (1), 100-10.

Moyle, P. (2008), 'The Future of Fish in Response to Large-Scale Change in the San Francisco Estuary, California', *American Fisheries Society Symposium,* 64 (0).

Moyle, P., et al. (2004), 'Biology and Population Dynamics of Sacramento Splittail (Pogonichthys macrolepidotus) in the San Francisco Estuary: A Review', *San Francisco Estuary and Watershed Science,* 2 (2), 1-47.

Myrick, C. A. and Cech, J. J. (2000), 'Swimming performances of four California stream fishes: temperature effects', *Environmental Biology of Fishes,* 58 (3), 289-95.

North, E. W., et al. (2004), 'The influence of wind and river pulses on an estuarine turbidity maximum: Numerical studies and field observations in Chesapeake Bay', *Estuaries,* 27 (1), 132-46.

Nunes, R. A. and Simpson, J. H. (1985), 'Axial Convergence in a Well-Mixed Estuary', *Estuarine Coastal and Shelf Science,* 20 (5), 637-49.

Okubo, A. (1973), 'Effect of Shoreline Irregularities on Streamwise Dispersion in Estuaries and Other Embayments', *Netherlands Journal of Sea Research,* 6 (1-2), 213-24.

Oliveira, A., Fortunato, A. B., and Pinto, L. (2006), 'Modelling the hydrodynamics and the fate of passive and active organisms in the Guadiana estuary', *Estuarine Coastal and Shelf Science,* 70 (1-2), 76-84.

Orr, M., Crooks, S., and Williams, P. (2003), 'Will Restored Tidal Marshes Be Sustainable?', *San Francisco Estuary and Watershed Science,* 1 (1).

Osgood, D. T., et al. (2003), 'Tidal hydrology and habitat utilization by resident nekton in Phragmites and non-Phragmites marshes', *Estuaries,* 26 (2B), 522-33.

Overland, J. E. and Preisendorfer, R. W. (1982), 'A Significance Test for Principal Components Applied to a Cyclone Climatology', *Monthly Weather Review,* 110 (1), 1-4.

Pennock, J. R. (1985), 'Chlorophyll Distributions in the Delaware Estuary - Regulation by Light-Limitation', *Estuarine Coastal and Shelf Science,* 21 (5), 711-25.

Pethick, J. (2002), 'Estuarine and tidal wetland restoration in the United Kingdom: Policy versus practice', *Restoration Ecology,* 10 (3), 431-37.

Picman, J., Milks, M. L., and Leptich, M. (1993), 'Patterns of Predation on Passerine Nests in Marshes - Effects of Water Depth and Distance from Edge', *Auk,* 110 (1), 89-94.

Pomeroy, L. R. (1959), 'Algal Productivity in Salt Marshes of Georgia', *Limnology and Oceanography,* 4 (4), 386-97.

Preisendorfer, Rudolph W. and Mobley, Curtis D. (1988), *Principal component analysis in meteorology and oceanography* (Amsterdam; New York, NY, U.S.A.: Elsevier Science Publishing Company) xviii, 425 p.

Rakocinski, C. F., Baltz, D. M., and Fleeger, J. W. (1992), 'Correspondence between Environmental Gradients and the Community Structure of Marsh-Edge Fishes in a Louisiana Estuary', *Marine Ecology-Progress Series,* 80 (2-3), 135-48.

Resnick, Robert, Halliday, David, and Krane, Kenneth S. (1992), *Physics*, 2 vols. (4th edn.; New York: Wiley).
Rozas, L. P. (1995), 'Hydroperiod and Its Influence on Nekton Use of the Salt-Marsh - a Pulsing Ecosystem', *Estuaries,* 18 (4), 579-90.
Rubin, Edward S. and Davidson, Cliff I. (2001), *Introduction to engineering and the environment* (1st edn.; Boston: McGraw-Hill) xxi, 696.
Scheller, R. M., et al. (1999), 'An analysis of the influence of annual thermal variables on the occurrence of fifteen warmwater fishes', *Transactions of the American Fisheries Society,* 128 (2), 257-64.
Scully, M. E., Friedrichs, C., and Brubaker, J. (2005), 'Control of estuarine stratification and mixing by wind-induced straining of the estuarine density field', *Estuaries,* 28 (3), 321-26.
Simenstad, C., Reed, D., and Ford, M. (2006), 'When is restoration not? Incorporating landscape-scale processes to restore self-sustaining ecosystems in coastal wetland restoration', *Ecological Engineering,* 26 (1), 27-39.
Sinokrot, B. A. and Stefan, H. G. (1993), 'Stream Temperature Dynamics - Measurements and Modeling', *Water Resources Research,* 29 (7), 2299-312.
Sommer, T., et al. (2007), 'The collapse of pelagic fishes in the Upper San Francisco Estuary', *Fisheries,* 32 (6), 270-77.
Stacey, M. T., Burau, J. R., and Monismith, S. G. (2001), 'Creation of residual flows in a partially stratified estuary', *Journal of Geophysical Research-Oceans,* 106 (C8), 17013-37.
Stancyk, S. E. and Feller, R. J. (1986), 'Transport of Non-Decapod Invertebrate Larvae in Estuaries - an Overview', *Bulletin of Marine Science,* 39 (2), 257-68.
Stevenson, J. C. (1988), 'Comparative Ecology of Submersed Grass Beds in Fresh-Water, Estuarine, and Marine Environments', *Limnology and Oceanography,* 33 (4), 867-93.
Stewart, R. W. (1961), 'The Wave Drag of Wind over Water', *Journal of Fluid Mechanics,* 10 (2), 189-94.
Sutherland, G., Garrett, C., and Foreman, M. (2005), 'Tidal resonance in Juan de Fuca Strait and the Strait of Georgia', *Journal of Physical Oceanography,* 35 (7), 1279-86.
Swanson, C., et al. (2000), 'Comparative environmental tolerances of threatened delta smelt (Hypomesus transpacificus) and introduced wakasagi (H-nipponensis) in an altered California estuary', *Oecologia,* 123 (3), 384-90.
Temmerman, S., et al. (2003), 'Modelling long-term tidal marsh growth under changing tidal conditions and suspended sediment concentrations, Scheldt estuary, Belgium', *Marine Geology,* 193 (1-2), 151-69.
Temmerman, S., et al. (2004), 'Modelling estuarine variations in tidal marsh sedimentation: response to changing sea level and suspended sediment concentrations', *Marine Geology,* 212 (1-4), 1-19.
Toffolon, M. and Savenije, H. H. G. (2011), 'Revisiting linearized one-dimensional tidal propagation', *Journal of Geophysical Research-Oceans,* 116.
Uncles, R. J. and Stephens, J. A. (1990), 'Computed and Observed Currents, Elevations, and Salinity in a Branching Estuary', *Estuaries,* 13 (2), 133-44.
--- (2001), 'The annual cycle of temperature in a temperate estuary and associated heat fluxes to the coastal zone', *Journal of Sea Research,* 46 (2), 143-59.
--- (2011), 'The Effects of Wind, Runoff and Tides on Salinity in a Strongly Tidal Sub-estuary', *Estuaries and Coasts,* 34 (4), 758-74.
Valle-Levinson, A., et al. (2000), 'Convergence of lateral flow along a coastal plain estuary', *Journal of Geophysical Research-Oceans,* 105 (C7), 17045-61.

van Proosdij, D., et al. (2010), 'Ecological re-engineering of a freshwater impoundment for salt marsh restoration in a hypertidal system', *Ecological Engineering,* 36 (10), 1314-32.
Vannote, R. L. and Sweeney, B. W. (1980), 'Geographic Analysis of Thermal Equilibria - a Conceptual-Model for Evaluating the Effect of Natural and Modified Thermal Regimes on Aquatic Insect Communities', *American Naturalist,* 115 (5), 667-95.
Vanrheenen, N. T., et al. (2004), 'Potential implications of PCM climate change scenarios for Sacramento-San Joaquin River Basin hydrology and water resources', *Climatic Change,* 62 (1-3), 257-81.
Wagner, R. W., et al. (2011), 'Statistical Models of Temperature in the Sacramento-San Joaquin Delta Under Climate-Change Scenarios and Ecological Implications', *Estuaries and Coasts,* 34 (3), 544-56.
Ward, J. V. and Stanford, J. A. (1982), 'Thermal Responses in the Evolutionary Ecology of Aquatic Insects', *Annual Review of Entomology,* 27, 97-117.
Washington, W. M., et al. (2000), 'Parallel climate model (PCM) control and transient simulations', *Climate Dynamics,* 16 (10-11), 755-74.
Weisberg, S. B., Whalen, R., and Lotrich, V. A. (1981), 'Tidal and Diurnal Influence on Food-Consumption of a Salt-Marsh Killifish Fundulus-Heteroclitus', *Marine Biology,* 61 (2-3), 243-46.
Williams, R. B. (1964), 'Division Rates of Salt-Marsh Diatoms in Relation to Salinity + Cell-Size', *Ecology,* 45 (4), 876-&.
Wolters, M., et al. (2008), 'Restoration of salt-marsh vegetation in relation to site suitability, species pool and dispersal traits', *Journal of Applied Ecology,* 45 (3), 904-12.
Yin, K. D., Lin, Z. F., and Ke, Z. Y. (2004), 'Temporal and spatial distribution of dissolved oxygen in the Pearl River Estuary and adjacent coastal waters', *Continental Shelf Research,* 24 (16), 1935-48.
Yin, K. D., et al. (2000), 'Dynamics of nutrients and phytoplankton biomass in the Pearl River estuary and adjacent waters of Hong Kong during summer: preliminary evidence for phosphorus and silicon limitation', *Marine Ecology-Progress Series,* 194, 295-305.
Zimmerman, R. J. and Minello, T. J. (1984), 'Densities of Penaeus-Aztecus, Penaeus-Setiferus, and Other Natant Macrofauna in a Texas Salt-Marsh', *Estuaries,* 7 (4A), 421-33.

Appendix A: Flow Effects on Water Temperatures

In chapter 3, we presented results studying the thermal dynamics in a tidal slough. After analyzing the advection-diffusion equation for cross-sectionally averaged temperatures (section 3.4.3), we concluded that the advective term dominated the thermal budget in Cache Slough on hourly time-scales (Figure 3-14). It was not surprising that the tidally-dominated advection of thermal gradients is important in small tidal sloughs on short time-scales. This, of course, contrasted with our findings in chapter 2, which studied daily thermal dynamics on the Sacramento and San Joaquin Rivers.

In Chapter 2, we presented daily water temperature models that show high predictive skill ($R^2 > 0.95$) for both calibration and verification periods (Figures 2-5 and 2-6) without accounting for the effects of riverine flows. Indeed, inclusion of flows in the daily temperature model did not improve model results (Section 2.6.2). This was a counter-intuitive result, as advection of along-channel thermal gradients should be an important term in the thermal budget. We reasoned that flows from upstream had already equilibrated with the atmosphere prior to reaching the Delta; this equilibration greatly reduced the along-channel thermal gradient. This reasoning was corroborated by observations by Bartholow (1989) that reservoirs do not influence temperatures more than 25 or 30 km downstream. This effect, we believed, indicated that riverine flows were not an important contributor to the daily heat budget at a location in the Delta. We did note, however, that our model appeared to deviate from the measured water temperatures during high flow events (Figure 2-9) and during high flow years (Figure 2-8).

Further analysis has shown that higher flows do correlate with model residuals on longer time-scales. Close analysis of Figure 2-10 shows that high flows correlate with larger absolute residuals due to cooler water temperatures than predicted. High flow years have as much as 2°C difference in daily residuals from low flow years. This effect is seasonal, however, so we did not notice it in our daily model. Averaging our residuals (measured minus modelled water temperatures) on the Sacramento River at Rio Vista over the course of a year and plotting against Sacramento River flows for that year shows this more clearly (Figure A-1).

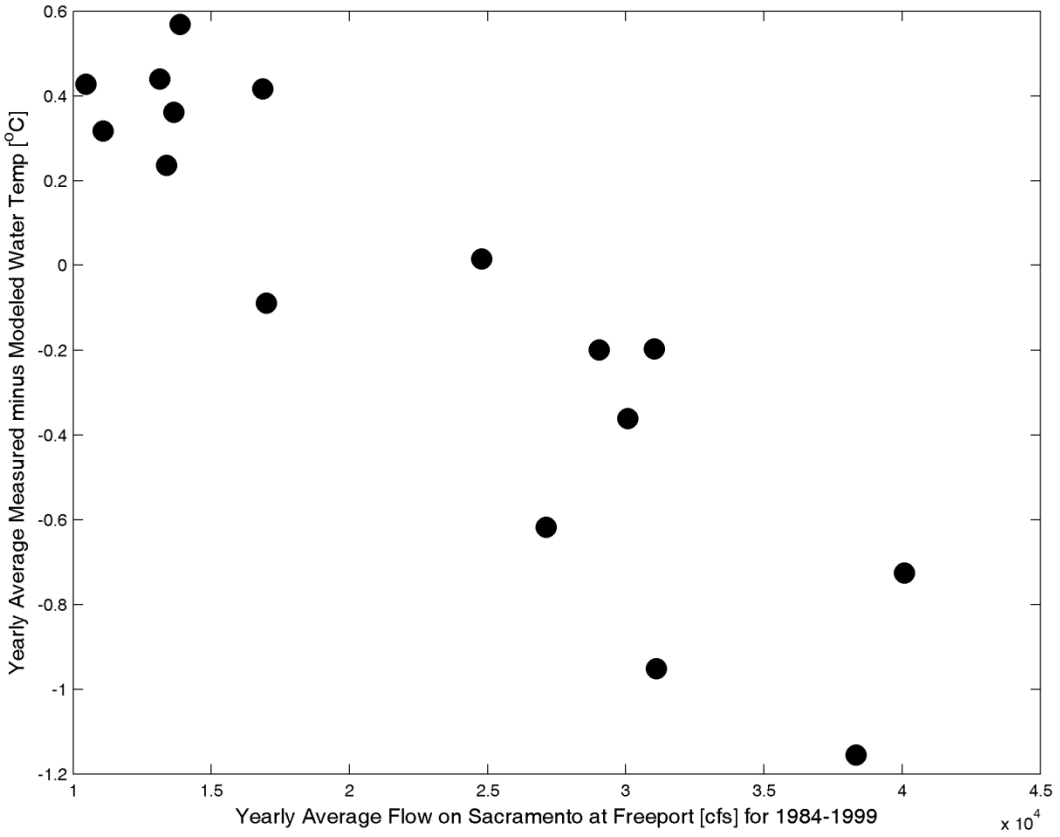

Figure A-1: Flow Effect on Yearly Averaged Model Residuals. High flow years have residuals as low as -1°C lower while low flow years are typically around +0.5°C.

Flows would not have improved the statistical model we presented in chapter 2 because flow generally has a negligible effect on temperatures. For years with flows less than 2 x 10^4 cfs, there does not appear to be a relationship between flow and residuals. Similarly, Figure 2-10 does not show any obvious pattern in the residuals during low flow times. This would also apply to times within years when flows are low. When the flows pick up, over time-scales of weeks or months, however, they drive the water temperatures down, potentially as much as a couple degrees (Figure 2-10) and affecting the yearly average of the measured water temperature. In wet years, this can affect the model's performance and, more importantly, the local water temperatures. Since so much of the variability in water temperature is contained in the yearly cycle, however, it is unlikely that the model's performance would ever be greatly compromised since the model still captures the yearly variability quite well.